CHARGE TRANSPORT INVESTIGATIONS IN NOVEL TRIARYLAMINE DERIVATIVES BASED ORGANIC DEVICES

Thesis

Submitted in partial fulfilment of the requirements for the degree of

DOCTOR OF PHILOSOPHY

by

JEAN MARIA FERNANDES

DEPARTMENT OF PHYSICS

NATIONAL INSTITUTE OF TECHNOLOGY KARNATAKA,

SURATHKAL, MANGALORE-575025

FEBRUARY, 2018

DECLARATION

by the Ph.D. Research Scholar

I hereby *declare* that the Research Thesis entitled "Charge Transport Investigations in Novel Triarylamine Derivatives Based Organic Devices", which is being submitted to the National Institute of Technology Karnataka, Surathkal in partial fulfilment of the requirements for the award of the Degree of Doctor of Philosophy in Physics is a *bonafide report of the research work carried out by me*. The material contained in this Research Thesis has not been submitted to any University or Institution for the award of any degree.

Jean Maria Fernandes
Reg. No: 100502PH10F02
Department of Physics

Place: NITK-Surathkal
Date:

CERTIFICATE

This is to *certify* that the Research Thesis entitled "Charge Transport Investigations in Novel Triarylamine Derivatives Based Organic Devices", submitted by Jean Maria Fernandes (Register Number**:** 100502PH10F02) as the record of the research work carried out by her, is *accepted as the Research Thesis submission* in partial fulfilment of the requirements for the award of degree of Doctor of Philosophy.

Dr. M. N. Satyanarayan
Research Guide

Prof. G. Umesh
Research Co-Guide

Chairman - DRPC
Date:

ACKNOWLEDGEMENT

I record my sincere gratitude to my Research Guides, Dr. M. N. Satyanarayan and Prof. G. Umesh, for their guidance, motivation and support throughout my research work. I am grateful to NITK Surathkal and its Physics department for awarding the full time Institute Research Scholarship and contingency grant. I thank the Chairman and the members of the Research Progress Assessment Committee for their suggestions. I extend my thanks to the entire teaching faculty and non-teaching staff of the Physics department, NITK, for their co-operation.

I would like to acknowledge the Ministry of Electronics and Information Technology, India for financial support through a research grant, and Dr. Arun M. Isloor's group, Chemistry department, NITK, for the collaborative work in the project. I sincerely thank Prof. V. Jayathirtha Rao's group, IICT Hyderabad, for the synthesis of new organic compounds used in this work. I am grateful to Prof. K. L. Narasimhan, IIT Bombay, and Mr. Meghan P. Patankar, TIFR Mumbai, for their guidance in the initial stages of my experimental work. I thank Prof. Thomas Anthopoulos, KAUST Thuwal, and Prof. Subhasis Ghosh, JNU Delhi, for sharing their expertise with our research group. I sincerely thank Prof. U. Sripati, Dr. T. Laxminidhi, Mr. Sanjeeva Poojary and the staff of Analog Lab, Electronics & Communication department, NITK, for their support and timely help in the setup of electronic circuits. I thank Dr. K. Navamani, JNCASR Bengaluru, for providing valuable insights into my research work. I thank Dr. Kartick Tarafder for his guidance and help in computational work. I also thank the editors and reviewers of my publications for their valuable assessment.

My thanks go to many of the present and former research scholars, staff and students of Physics and other departments, including my former and present colleagues of Optoelectronics Laboratory for their co-operation. I specially acknowledge many research scholars for their help in completing this work. I remain grateful for all the help, moral support, technical aid and motivation I received from many people, directly or indirectly in several aspects, at different stages throughout my Ph. D. tenure. Finally, I acknowledge the support and encouragement from my family in this endeavor.

ABSTRACT

Research on new organic semiconductor materials and their optoelectronic properties has been growing in prominence due to diverse potential applications. This thesis explores the charge transport properties of some novel triarylamine based organic semiconductors in hole-only devices to examine their suitability for OLED applications. Devices fabricated by physical vapor deposition are characterized using Impedance Spectroscopy as well as frequency and/or voltage dependent measurements of current density, capacitance and conductivity. The thickness dependent hole injection efficiency of 2,3,5,6-tetrafluoro-7,7,8,8-tetracyanoquinodimethane (F_4TCNQ) film in devices of *N,N′*-Di(1-naphthyl)-*N,N′*-diphenyl-(1,1′-biphenyl)-4,4′-diamine (α-NPD) shows that the hole injection and transport properties reach a maximum for F_4TCNQ film of optimum thickness of ~ 4 nm. The hole mobility of α-NPD (~ 10^{-5}-10^{-4} $cm^2V^{-1}s^{-1}$) is observed to increase over several orders of magnitude with its thickness and is found to be in good agreement with the literature. Following these studies, the electrical and optical properties of hole-only devices are investigated using triphenylamine (TPA) derivatives with either methyl or tert-butyl as side groups. This substitution is seen to improve charge transport properties. In addition to the above mentioned measurements, the role of side groups on the electrical and optical properties of the TPA derivatives is also investigated through UV-Vis and Photoluminescence (PL) spectroscopy. The frequency dependent analysis of charge carrier hopping rate reveals a crossover from dc to ac conductivity in the presence of a small ac bias. The new TPA molecules investigated are seen to possess hole mobility in the order of 10^{-7}-10^{-6} $cm^2V^{-1}s^{-1}$ and Photo Luminescence (PL) efficiency (~ 30%) which indicate their suitability for OLED applications.

Keywords: Organic semiconductor, Impedance Spectroscopy, triarylamine, mobility, hopping rate.

CONTENTS

LIST OF FIGURES

Page No.

LIST OF TABLES

NOMENCLATURE

OLED	Organic Light-Emitting Diode
OPV	Organic Photovoltaic
OFET	Organic Field Effect Transistor
GDOS	Gaussian Density of States
HOMO	Highest Occupied Molecular Orbital
LUMO	Lowest Unoccupied Molecular Orbital
IS	Impedance Spectroscopy
SCLC	Space-Charge-Limited Current
α-NPD	N,N′-Di(1-naphthyl)-N,N′-diphenyl-(1,1′-biphenyl)-4,4′-diamine
F_4TCNQ	2,3,5,6-tetrafluoro-7,7,8,8-tetracyanoquinodimethane
J	Current Density
q	Electronic Charge
V	Applied Voltage
V_{bi}	Built-in Voltage
F	Electric Field
T	Temperature
ε_0	Permittivity of Vacuum
ε_r	Relative Permittivity
k_B	Boltzmann Constant
d	Thickness of the organic layer

μ	Carrier Mobility
β	Poole-Frenkel Factor
τ_d	Characteristic Time
τ_r	Relaxation Time
C	Capacitance
R	Resistance
Z	Impedance
ϕ	Phase Shift
ω	Angular Frequency
f	Frequency
Re[$Z(\omega)$]	Real part of frequency dependent impedance
Im[$Z(\omega)$]	Imaginary part of frequency dependent impedance
δ	Loss angle
tan δ	Loss tangent (dissipation factor)
ε'	Real part of dielectric constant
ε''	Imaginary part of dielectric constant (dielectric loss factor)
$-\Delta B$	Negative Differential Susceptance
$\omega\Delta G$	Differential Conductance
G	Susceptance
B	Conductance
Y	Admittance

A	Area
TPA	Triphenylamine
CPE	Constant Phase Element
$N(E_f)$	Density of localized states
E_f	Fermi energy
W_m	Carrier Binding energy
R	Minimum hopping length
γ	Hopping Rate coefficient
σ	Hopping conductivity
b	Dynamic state factor
PL	Photoluminescence

CHAPTER 1

INTRODUCTION

1.1 BACKGROUND AND MOTIVATION

Organic electronics is an emerging interdisciplinary field of Photonics, dealing with the design, synthesis, characterization, and device applications of organic small molecules or polymers having suitable electronic properties. These materials are mainly carbon-based; unlike inorganic materials, such as Silicon, Germanium, Gallium Arsenide, etc., used in traditional electronics. Organic electronics is receiving steady and increasing attention in optoelectronics since the past few decades due to the advent of new class of materials known as organic semiconductors (Brütting 2005, Sergiyenko 2011). Organic semiconductor devices can be broadly classified into three main classes, namely organic light-emitting diodes (OLEDs) (Tang and Van Slyke 1987), organic photovoltaics (OPVs) (Lu et al. 2015), and organic field-effect transistors (OFETs) (Uemura et al. 2016). A few commercially developed prototypes based on organic semiconductors are shown in figure 1.1 (a-d). The 77" flexible and transparent OLED display by LG, shown in figure 1.1 (a) features a resolution of 4K/UHD (3840 x 2160), 80 mm radius of curvature and 40% transparency. Figure 1.1 (b) shows a bright Amber OLED panel developed by Yeolight Technology to be used for automotive OLED rear lights. This panel has a size 85x85 mm (active area 76.5x76.5 mm) and color temperature 2000 K-2600 K. Its efficiency is > 70 lm/W at 2,000 cd/m^2 brightness and the lifetime is over 20,000 h. In figure 1.1 (c), the Lumiblade 12 x 12 cm OLED Panel Brite FL300 Philips with a luminous flux of up to 300 lumen is shown. Figure 1.1 (d) shows two flexible white passive-matrix OLED (PMOLED) panels by Wisechip, one is 1.8" 160x32 and the other 1.36" 128x16. The curvature radius of the displays is 40 mm.

Organic materials are lighter, flexible, and a very large variety of these materials are available, which makes them attractive alternatives in many applications. An added

advantage is that these materials can be processed on a large scale (in many cases) by employing low temperature techniques, solution processing or even screen printing technology for device fabrication.

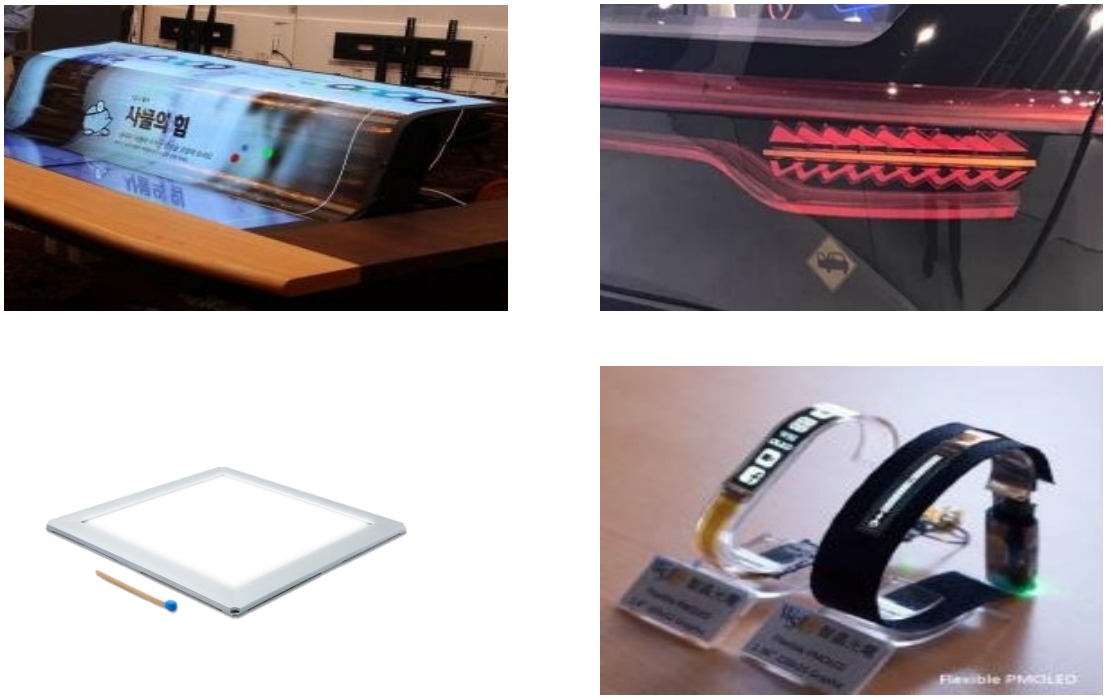

Figure 1.1 Commercially developed prototypes based on organic semiconductors: (Clockwise from left) **(a)** LGD 77" flexible and transparent OLED display-2017 (www.oled-info.com) **(b)** Yeolite OLED panel prototype for automotive rear lights -2017 (www.oled-info.com) **(c)** Lumiblade 12 x 12 cm OLED Panel Brite FL300 Philips-2015 (www.lighting.philips.co.uk) and **(d)** Wisechip flexible PMOLED displays-2017 (www.oled-info.com)

The amorphous nature of the organic materials allows structural flexibility and does not require lattice matching at the organic interfaces in order to obtain high quality films of large size (Forrest 1997). This enables large scale applications, such as smart windows, electronic paper, etc. It may be emphasized that good lattice matching between the substrate and deposited film is a critical requirement in devices based on crystalline thin films requiring intricate fabrication procedures and hence, leading to high costs. The flexible nature of organic films also leads to added benefits, such as mechanical flexibility, light weight, and cost-effective fabrication procedures (Koch

2007). Another advantage of these materials is the option to tailor their electronic and optical properties by chemically modifying the molecular structure (Montes et al. 2004).

Inorganic semiconductors, such as silicon and germanium played a dominant role in the electronics industry ever since the invention of the transistor in the middle of the last century, and continue to reign the world of microelectronic applications of which optoelectronics forms an important part. Organic electronics revolution has provided new prospects in optoelectronics (Brütting 2005). However, a major limitation of organic devices is the lack of high purity organic materials and much lower carrier mobility compared to that of inorganics which prove far more robust in major electronic applications. Extensive research to address these fundamental challenges is still the need of the hour. Moreover, the organic optoelectronic devices are based on charge transport, and understanding this nature is crucial to design new materials with improved structure-property relationship. The charge transport in these materials also depends on the device architecture. Therefore, understanding the transport mechanism by correlating the device architecture and molecular structure with the electrical properties is necessary for the development of highly efficient devices.

1.2 ORGANIC SEMICONDUCTORS

Organic materials used in electronic device applications are mainly carbon based semiconductors having alternate single and double bonds, which are termed as conjugated organic materials. The atomic bonding in these systems results from hybridization, forming σ and π bonds. The delocalization of electrons due to the formation of the π bonds leads to the semiconducting properties of conjugated organic materials.

In case of sp^2 hybridization, which is often found in conjugated systems, strong σ bonds are formed by three electrons (one in s orbital and two in *x* and *y* planes of p orbitals) as shown in figure 1.2. These σ bonds determine the shape and structure of the molecule. The electron in the *z* plane of the p orbital forms the weaker π bond with its neighbor. These π-bond electrons freely move in the molecule, accounting for the

unique electronic properties of conjugated systems. The energy states formed by the molecular bonding and antibonding orbitals lead to the formation of occupied and unoccupied states, respectively.

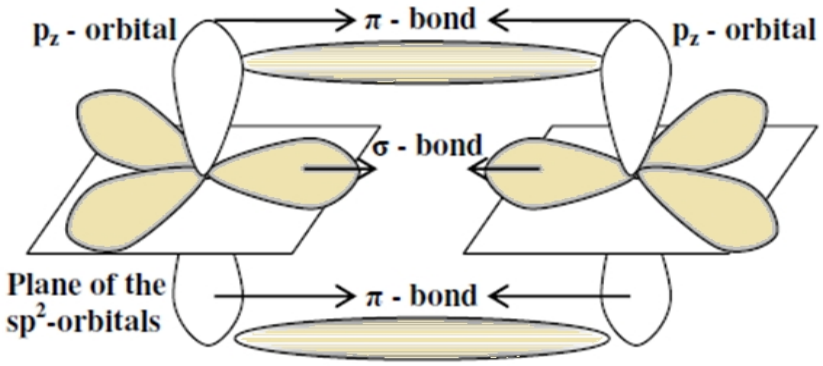

Figure 1.2 Schematic representation of sp^2 hybridization (Brütting 2005)

In the condensed phase, the bonding and antibonding orbitals merge to form band-like structures. The highest occupied molecular orbital (HOMO) is the state possessing the highest energy among all occupied orbitals and is analogous to the edge of the valence band in inorganic semiconductors. Similarly, the lowest unoccupied molecular orbital (LUMO) is the state possessing the lowest energy among all unoccupied orbitals and is analogous to the edge of the conduction band in inorganic semiconductors. Figure 1.3 shows the bonding (π) and antibonding (π*) levels in organic molecules and the formation of HOMO and LUMO in the solid. The π and π* states are stabilized in the molecular solid by polarization energies when compared to isolated molecules in the gas phase, leading to an energy level scheme (Brütting 2005). However, it is seen from the figure that there is a spread in the π and π* states compared to σ and σ* states. This is because, during the formation of σ bonds, electrons are attracted between two nuclei strongly due to effective head to head overlapping, whereas in π bond formation, electrons are not strongly attracted between nuclei due to weak parallel overlapping, leading to a spread of π electrons and orbitals over a wide area (Brütting 2005).

There are two classes of organic materials: small molecules and polymers, as shown in figure 1.4. Their device fabrication techniques are simpler than those used for

inorganic devices. This makes them promising candidates for the electronic industry. Organic materials can be processed at low temperatures (< 200°C) by either solution processing or vacuum deposition.

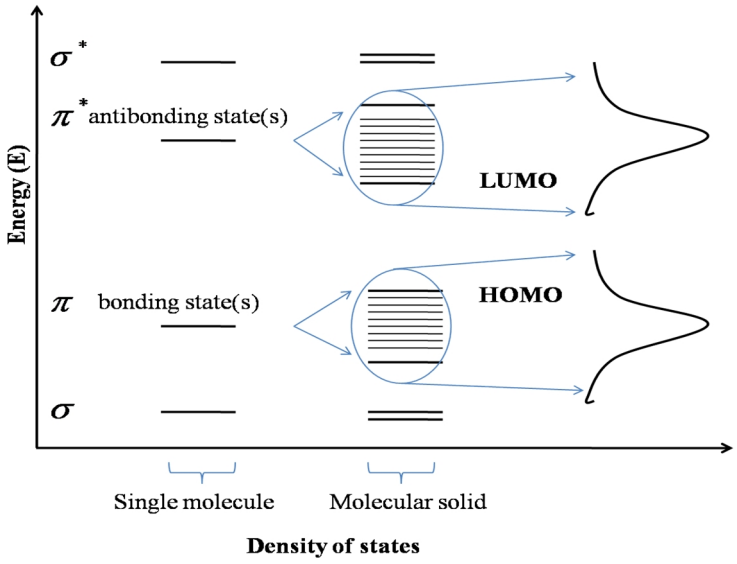

Figure 1.3 Formation of HOMO and LUMO with Gaussian Density of States (Brütting 2005)

The advantage of using small molecules is that they have a well-defined chemical structure, and their thin films produced by vacuum deposition are uniform and free from contaminants, leading to improved device properties (Tour 1996). In addition, the charge carrier mobility in small molecules is substantially higher than in polymeric materials (Dimitrakopoulos and Malenfant 2002).

Although organic semiconductors have intramolecular covalent bonds similar to conventional semiconductors, they are held together by weak intermolecular van der Waals interactions. The disorder in organic semiconductors leads to weak coupling between the molecules, giving rise to Gaussian density of states (GDOS). The shape of the density of states is assumed to be Gaussian since the coupling between a charge carrier and a random distribution of static or induced dipoles leads to a Gaussian function (Bässler 1993, Dieckmann et al. 1993). Due to this phenomenon, charge transport through organic semiconductors occurs by inter-site hopping of charge carriers through the GDOS of HOMO and/or LUMO between molecules.

(a)

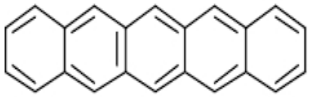

Pentacene

5,6,11,12-Tetraphenyltetracene (Rubrene)

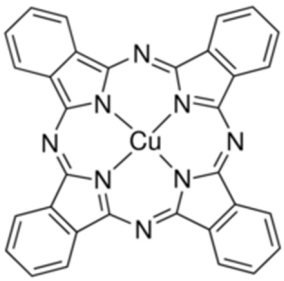

Copper(II) phthalocyanine (CuPc)

(b)

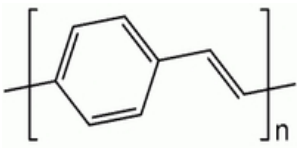

Poly(p-phenylene vinylene) (PPV)

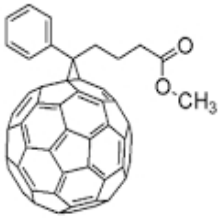

Phenyl-C61-butyric acid methyl ester (PCBM)

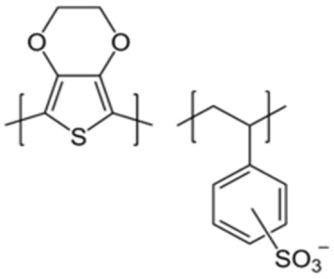

Poly(3,4-ethylenedioxythiophene) polystyrene sulfonate (PEDOT:PSS)

Figure 1.4 Some significant organic semiconductor **(a)** small molecules and **(b)** polymers (Brütting 2005)

Organic semiconductor materials used in applications such as OLEDs have various functions based on their conjugation type, ionization potential (IP), electron affinity (EA) and charge transport ability in the device. Depending on these factors, they are classified as hole injection, hole transport, electron injection, electron transport, hole blocking and electron blocking materials. The organic materials used in this thesis are small molecule organic semiconductors. The charge transport materials should be capable of forming pinhole-free smooth films and should be morphologically and thermally stable. A high glass transition temperature of these materials is required to

enable operation of devices at operating temperatures. They should have a wide optical band gap, thus confining the injected carriers within the emitting layer and leading to radiative recombination. The commonly used hole transport materials include triarylamines, triphenylamines, thiophenes, etc. (Bellmann et al. 1998, Shirota and Kageyama 2007). Metal chelates, oxadiazole derivatives, triazoles, etc., are some of the commonly used electron transport materials.

1.3 DEVICE STRUCTURES

A typical multilayer organic light-emitting diode (OLED) consists of the emissive layer that is sandwiched between the charge transport layers and the electrodes as shown in figure 1.5. Holes from the anode and electrons from the cathode recombine to form excitons, which should preferably decay radiatively in the emissive layer. The hole mobility in organic materials is generally two orders of magnitude greater than that of electrons (Tiwari and Greenham 2009). Due to this, the recombination takes place in the vicinity of the cathode and results in quenching of the excitons, leading to decrease in the lifetime and efficiency of the device (Burin and Ratner 2000). Studies have shown that multilayer structures have balanced carrier injection and transport.

As seen in figure 1.5, inclusion of hole/electron blocking layers on either side of the emissive layer acts to confine the charge carriers within the emissive layer, which greatly improves the device performance (Adachi et al. 1988, Troadec et al. 2001, Hao et al. 2006). Further, the inclusion of hole and electron injection layers (HIL and EIL) in the device lowers the charge injection barriers at the anode and cathode, respectively. The hole and electron transport layers (HTL and ETL) enable easy passage for the injected carriers to reach the emissive layer (Shinar 2004). The most widely used anode is indium tin-oxide (ITO) which is highly transparent in the visible region, owing to its large band gap (Kim et al. 1999). The cathode typically constitutes any of the low work function metals, such as aluminum, magnesium, and calcium or their alloys with silver.

The materials are selected such that there is close energy barrier at the interface between various layers in the device. Because of this configuration, the charge transport into emissive layer becomes highly efficient.

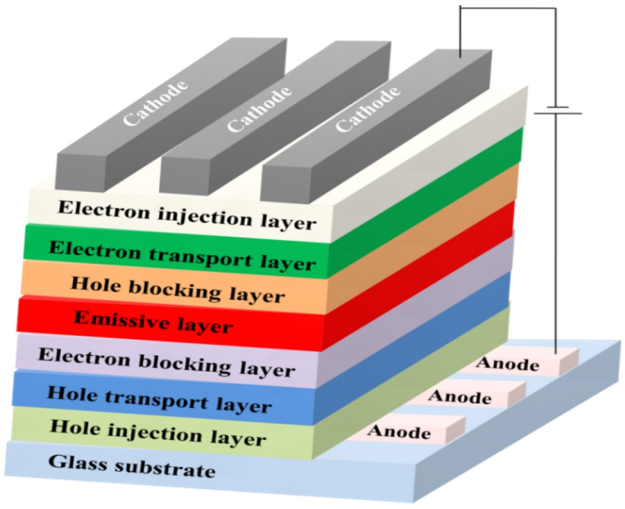

Figure 1.5 A typical multilayer OLED structure (Mazzeo 2010)

Figure 1.6 shows a schematic representation of the energy level matching in typical OLEDs. When an external voltage is applied to the device, there is bending of the energy levels (not shown in this figure).

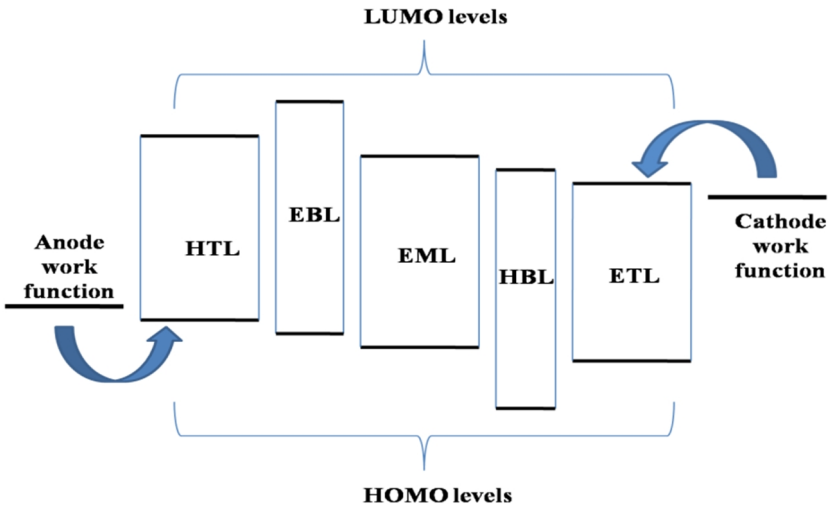

Figure 1.6 Schematic representation of the energy level diagram

The hole transport layer should possess high hole mobility and low ionization potential to enable efficient hole transport from the hole injection layer. Similarly, the electron transport layer should have high electron mobility and high electron affinity in order to match the work function of the cathode and enable efficient electron transport

to the emissive layer. As a first step towards optimizing the device performance, it is prudent to study single carrier devices in order to reveal the role of geometry of films of different materials and the film quality. In this work, hole-only devices have been investigated.

1.4 ROLE OF INTERFACES

In organic devices, the various interfaces play a crucial role in the device performance. The quality and the number of interfaces determine the efficiency and overall performance of these devices. In this regard, the understanding of energy level alignment at the interfaces is important.

1.4.1 Metal-Organic Interfaces

The energy level alignment at the electrode-organic interfaces determines the charge injection into the device. The work functions of the anode and cathode have to match the HOMO and LUMO energy levels of the organic layer immediately next to them, for efficient hole and electron injection, respectively. In practical devices, this is facilitated by the hole and electron injection layers between the electrode and the charge transport layers. For negligible energy barrier between the metal and organic layer, an ohmic contact ensues. At larger energy barriers, the junction functions as a Schottky contact.

The schematic representation of energy level alignment at the two electrode-organic interfaces is shown in Figure 1.7 (a) and (b), where the vacuum levels of metal and organic are assumed to be aligned. The position of the Fermi level in the metal with respect to the vacuum level gives the work function of the metal and is denoted by ϕ_m. The energy barriers to hole and electron injection are denoted as ϕ_h and ϕ_e, respectively.

In ideal cases, the Fermi level position of the anode/cathode should match the ionization potential (IP)/electron affinity (EA) of the organic materials, respectively. However, in cases of many metal-organic interfaces, the assumption of a common vacuum level does not suffice. There exists a small vacuum level offset between that of metal and organic due to the formation of interfacial dipoles arising from the formation

of chemical bonds and charge transfer ("push-back") effect (Salaneck et al. 1996, Koch et al. 2006, Kanai et al. 2012).

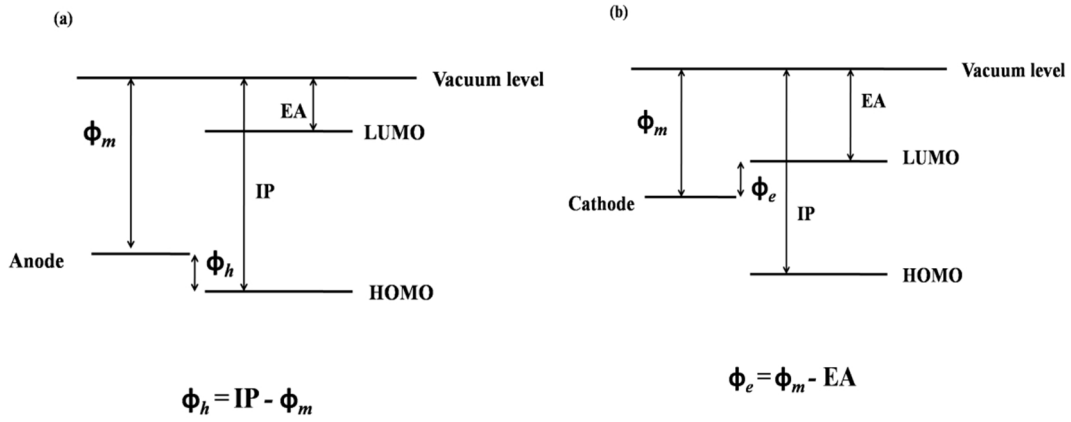

Figure 1.7 Schematic representation of the energy level diagram at the **(a)** anode-organic and **(b)** cathode-organic interfaces assuming a common vacuum level (Koch et al. 2006)

Therefore, in practical devices, there certainly exists a small barrier due to this vacuum level misalignment even if the work function of the metal matches the IP or EA of the organic materials.

1.4.2 Organic-Organic Interfaces

Although a similar approach is followed in understanding the organic-organic interfaces, their underlying physics is not as straightforward as that of metal-organic interfaces. This is because of a number of factors, such as alignment of molecular orbital energies (HOMO and LUMO), interfacial dipoles, structural defects, molecular orientation in the thin films, etc., involved in the formation of these interfaces (Yonezawa et al. 2014, Opitz et al. 2016).

Several theoretical models have been developed in literature to address the issue of interface energetics between different organic layers, based on the type of interfaces (Beljonne et al. 2011, Liu et al. 2012, Ryno et al. 2016).

1.5 CHARGE INJECTION AND TRANSPORT MECHANISM

The knowledge of charge injection and transport mechanism in crystalline inorganic semiconductors is well established since many decades. The extension of this knowledge to amorphous organic semiconductors has met with several obstacles, since the charge transport in amorphous materials occurs by hopping in a manifold of localized states and not by band-like transport as in inorganic semiconductors. Several theoretical models have been proposed based on simulations and experiments (Tessler et al. 2009), but there is still need for extensive research to arrive at an accurate model. This becomes quite challenging since the nature of the interface in terms of composition and structure is not well understood. For example, the charge injection is influenced by substrate preparation conditions, deposition parameters, material properties and device architecture (Coropceanu et al. 2007).

1.5.1 Charge Injection Mechanism

In organic semiconductor devices, charge injection from the metal electrode into the organic semiconductor depends on the barrier between the two. Upon formation of electrode-organic interface, diffusion of the charge carriers into the organic layers results in an image force, thereby lowering the potential barrier. This leads to a reduction in the energy of the interface states whereby they become energetically available to the electrons hopping from the metal Fermi surface.

On the other hand, the bulk states, deep in the organic layer remain energetically unavailable for charge hopping because the image potential decreases rapidly away from the interface. However, on applying an external electric field, the energy of the available states in the bulk of the organic layers is lowered. This results in an increased probability of carrier hopping into bulk states (Shinar 2004, Brütting 2005, Ng et al. 2007).

Charge injection from a metal into a semiconductor is well described in inorganic semiconductors using two well accepted models, known as Fowler-Nordheim (FN) model for tunneling injection and the Richardson-Schottky (RS) model for

thermionic emission (Sze and Ng 2007). The Fowler-Nordheim (FN) model considers that electrons from the metal, tunnel through a triangular barrier into unbound continuum states on the other side. This model neglects the image charge effects and the barrier height, which play an important role in organics. It also considers current density to be independent of temperature as shown in equation 1.1 below (Sze and Ng 2007).

$$J(V) = \frac{q^3 V^2 m_0}{8\pi h \phi m^*} \exp\left[-\frac{4(2m^*)^{1/2}\phi^{3/2}}{3hqV} \right] \tag{1.1}$$

where m_0 is the mass of the free electron, m^* is the electron effective mass, h is the Planck's constant, q is the elementary charge, ϕ is the barrier height and V is the applied voltage.

On the other hand, the Richardson-Schottky (RS) model assumes that the superposition of the external and image charge potential results in a potential maximum, and once an electron from the metal has acquired sufficient thermal energy to cross this potential, it can be injected into the semiconductor. In this formalism, the tunneling of electrons across the barrier is taken to be absent. The charge transport in organic solids is a Brownian process and the mean-free path is comparable to the intermolecular distance. The current density is given by the following equation (Sze and Ng 2007).

$$\left.\begin{aligned} J(F) &= A^* T^2 \exp\left[-\frac{q(\phi - \sqrt{qF/4\pi\varepsilon_r\varepsilon_0})}{kT} \right] \\ A^* &= \frac{16\pi\varepsilon_r\varepsilon_0 N_0 \mu k_B^{\,2}}{q^2} [A/cm^2K^2] \end{aligned}\right\} \tag{1.2}$$

where A^* is the Richardson factor, T is the temperature, q is the elementary charge, ϕ is the barrier height, F is the applied field, ε_0 is the permittivity of vacuum, ε_r is the relative permittivity, k_B is the Boltzmann constant, N_0 is the density of surface states and μ is the charge carrier mobility.

The inadequacy of both these models led to other extended charge injection

models. Arkhipov et al. (1998) presented an analytical model based on thermally stimulated hopping theory. Wolf et al. (1999) performed detailed Monte Carlo simulations of charge injection from a metal to an organic semiconductor layer. More recently, Gozzi et al. (2015) described charge injection at metal-organic semiconductor heterojunctions using a combination of the FN model and the model proposed by Arkhipov et al. (1998).

1.5.2 Hopping Transport Mechanism

The charge carriers in the Gaussian distribution of density of states (GDOS) in organic materials are localized and they hop within a collection of discrete energy states. This hopping transport is modeled mainly using the Gaussian Disorder Model (GDM) proposed by Bässler (1993). The Gaussian energy distribution is given by the following expression

$$g(E) = (2\pi\sigma^2)^{-1/2} \exp\left(-\frac{E^2}{2\sigma^2}\right) \tag{1.3}$$

where σ is the width of the density of states (DOS) and E is energy relative to the center of the DOS. The schematic of the Gaussian distribution of energies showing the transport and localized states is shown in the figure 1.8.

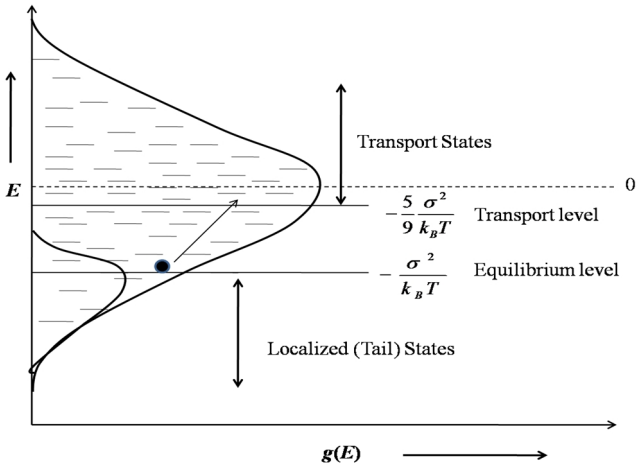

Figure 1.8 Schematic of the Gaussian disorder model (Kramer 2002, Craciun 2011)

The charge transport in the GDOS is fundamentally governed by the equilibrium level and transport level (Kramer 2002). The equilibrium level represents the maximum of the density of occupied states and has energy equal to $-\sigma^2/k_BT$. The charge carriers within the GDOS relax to this level, and this acts as a starting point for the carriers to move towards the transport level.

The transport level with energy $-5/9(\sigma^2/k_BT)$ is relevant to the charge transport. The charge carrier is free to move in the transport states. However, beyond the equilibrium level towards the bottom of the GDOS, there exist localized (tail) states where the charge carrier is localized and trapped. The position of the Fermi level depends on the carrier density (Craciun 2011). At low carrier density, the Fermi level lies below the equilibrium level, whereas it crosses the equilibrium level with increasing carrier density. The energy difference between the equilibrium and transport levels gives the activation energy. At low field, this leads to the mobility being directly proportional to $\exp[-(2\sigma/3k_BT)^2]$ (Kramer 2002, Craciun 2011).

Various numerical and analytical models have also been proposed as an extension to GDM or as its alternative in order to provide an insight to the underlying physical mechanism (Arkhipov et al. 1998). Traditionally, both numerical and analytical models of charge carrier hopping in disordered materials are based on the Miller-Abrahams (1960) expression

$$\nu(r,E,E') = \nu_0 \exp(-2r/a) \begin{cases} 1, & E < E' \\ \exp[-(E-E')/(k_BT)], & E > E' \end{cases} \qquad (1.4)$$

where ν is the frequency of carrier jumps over a distance r from a localized state with energy E to a state with energy E', a is the localization radius, k_B is the Boltzmann constant and T is the temperature.

A more specific expression than the Miller-Abrahams' was proposed by Rudolph A. Marcus in the 1950s, which describes local charge transport with a hopping rate from site i to site j over a distance r_{ij}, given by the following equation

$$\nu_{ij} = \frac{|I_{ij}|^2}{\hbar}\sqrt{\frac{\pi}{\lambda kT}}\exp\left[-\frac{(\Delta G_{ij}+\lambda)^2}{4\lambda kT}\right] \tag{1.5}$$

where I_{ij} is called the transfer integral, i.e. the wavefunction overlap between sites i and j, which is proportional to the tunnelling; λ is the reorganisation energy related to the polaron relaxation; kT is the thermal energy and ΔG_{ij} is the energy difference between the two sites.

In the Miller-Abrahams hopping rate, the polaronic effects are usually neglected (Tress 2014). Therefore, instead of transfer integrals, only the attempt-to-escape frequency is approximated. Instead of the reorganization energy, only energetic site differences derived from Gaussian density of states distribution are considered. It may be noted that the Miller-Abrahams model is applicable at low temperatures and to weak electron-phonon couplings, whereas Marcus model is appropriate for use at high temperatures and for strong electron-phonon coupling (Kumar 2017).

In general, charge carrier mobility in organic semiconductors depends on several factors, such as applied electric field, temperature, dopant concentration, traps, scattering and disorder in the system. Unlike in band transport in inorganic semiconductors, the mobility in the hopping transport of organic semiconductors increases with temperature. This is due to the lattice irregularity in organic semiconductors and/or the localization of the charge carriers at a defect site, both requiring an activated process of lattice vibrations for carrier movement from one site to the other. The temperature and field dependence of mobility follows the Poole-Frenkel behavior given by the following expression (Brütting et al. 2001),

$$\left.\begin{aligned} \mu(F,T) &= \mu_0 \exp\left(-\frac{\Delta E - \beta\sqrt{F}}{k_B T_{eff}}\right) \\ \text{with } \frac{1}{T_{eff}} &= \frac{1}{T} - \frac{1}{T_0} \text{ and } \beta = \sqrt{\frac{q^3}{\pi\varepsilon_r\varepsilon_0}} \end{aligned}\right\} \tag{1.6}$$

where ΔE is the activation energy at zero-electric field, T_0 is an empirical parameter, μ_0 is the mobility at temperature $T = T_0$, β is the Poole-Frenkel coefficient, q is the charge,

ε_0 is the permittivity of vacuum, ε_r is the relative permittivity of the organic semiconductor and F is the electric field.

The charge transport is influenced by traps present in the organic semiconductor that can be either intrinsic or extrinsic. Basically, these traps are localized electronic states associated with chemical impurities, structural disorder and surface states. Extrinsic traps due to impurities can be avoided by repeated sublimation process, whereas intrinsic traps are formed due to structural disorders due to different growth conditions, and mainly affect the device performance. Traps are temperature dependent and are classified as deep and shallow traps, depending on their position occupied in the energy distribution. The charge transport and the device performance are mainly affected by deep traps. The traps can be further classified as fast and slow, depending on their rate of trapping and releasing the charge carrier comparable to the carrier transit time. Trap- filling is another important process where the increase in temperature and applied field helps in the filling of traps. This leads to improvement in charge transport through the device.

Trapping is considered to be the primary cause of dispersion in many organic systems (Philippa et al. 2014, Berleb and Brütting 2002, Borsenberger et al. 1992). The anomalous dispersion in the transit time of charge carriers is described by Scher and Montroll (1975) where the hopping transport in disordered organic semiconductors is given by the waiting time distribution of the charge carriers between successive hops as

$$\psi(t) \sim t^{-(1+\alpha)} \tag{1.7}$$

Here, α is the dispersion parameter and $0 \leq \alpha \leq 1$ (Scher and Montroll 1975, Tripathi et al. 2011).

From equation 1.7 it can be implied that the average position of a carrier is proportional to t^{α} (Tripathi et al. 2011). When this is the case, small signal *ac* component comes into picture and the frequency dependence of admittance Y in the space-charge-limited regime is related to frequency $\Omega = 2\pi f\tau_{dc} = \omega\tau_{dc,}$ where ω is

angular frequency and τ_{dc} is the dc transit time (Tsang and So 2006, Tripathi et al. 2011).

The *ac* mobility normalized to dc mobility is given by (Tripathi et al. 2011, Martens et al. 1999, Tsang and So 2006).

$$\tilde{\mu}(\Omega) = \mu(\Omega) / \mu_{dc} = 1 + M(i\Omega)^{1-\alpha} \tag{1.8}$$

where M and α are the dispersion parameters. Combinations of these parameters have been used by various groups to simulate and determine the numerical factor $k = \tau_d/\tau_r$ for different degree of dispersion (Tripathi et al. 2011, Okachi et al. 2008, Tsang and So 2006). For non-dispersive transport, $M = 0$ and $\alpha = 1$ (Tripathi et al. 2011).

The details on the current flow mechanism in organic devices are presented in the next chapter.

1.6 LITERATURE REVIEW

Bernanose (1955) first observed electroluminescence in organic materials when very high *ac* potential was applied to organic cells of acridine derivatives and carbazole. Later Pope et al. (1963) observed dc electroluminescence in anthracene single crystals above an applied voltage of 400 V. Owing to the difficulty in producing large sized single crystals and the requirement of very high applied electric fields to produce luminescence, this phenomenon did not gain commercial interest. In an attempt to reduce the drive voltage, Vincett et al. (1982) made use of thin organic films instead of single crystals in their electroluminescent (EL) devices and were successful in obtaining a significantly low drive voltage less than 30 V. However, these devices were single layered, i.e. a single organic layer was sandwiched between two injecting electrodes in the device, which led to inefficient electron injection and instability of the EL device, accounting for quantum efficiency of only about 0.05 %.

The pioneering breakthrough came from Tang and Van Slyke (1987) who fabricated highly efficient double organic layer EL devices. This EL device produced green light emission of high brightness (> 1000 cd/m^2) at a dc voltage of less than 10 V. This low drive voltage could be achieved due to the incorporation of a low work

function cathode metal such as Mg:Ag alloy which is suited for electron injection into organic materials. This is because, the work function of Mg:Ag alloy is energetically well matched to the LUMO of the electron transport layer Alq_3. However, the device lifetime was rather short. Further research focused on multilayer devices, wherein better charge transport and charge carrier confinement led to highly efficient devices. In this process, it was clear that detailed understanding of charge carrier transport in organic semiconductors is necessary to produce highly efficient devices (Li and Meng 2006). A variety of techniques have been employed for the characterization of organic electronic devices (Li and Meng 2006, Cheung et al. 2008, Tripathi et al. 2010, Blakesley et al. 2014, Landi et al. 2016, Aloui et al. 2014, Ooi et al. 2014, Fukuda et al. 2014, Philippa et al. 2015, Bittle et al. 2016).

Different characterization techniques employed to evaluate charge carrier mobility in organic semiconductors involve transient and steady-state measurements and are listed below (Kokil et al. 2012):

- Time-of-flight (TOF)
- Space-charge-limited current (SCLC) measurement
- Dark-injection space-charge-limited current (DI-SCLC) measurement
- Transient electroluminescence (T-EL)
- Charge extraction by linearly increasing voltage (CELIV) measurement
- Organic field-effect transistor (OFET)
- Impedance Spectroscopy (IS)

The conventional time-of–flight (TOF) method used to determine mobility has the disadvantages of a very thick film (~ several microns) requirement besides requiring a UV laser for excitation of charge carriers (Cheung et al. 2008). Thinner films (~ 100 nm) can be used in SCLC and DI-SCLC measurements. However, these methods require the use of an ohmic injecting contact at one end (Malliaras and Scott 1999, Campbell et al. 2001). Another method called transient electroluminescence requires that the mobility of one carrier be substantially higher than that of the other (Mückl et al. 2000). In CELIV measurement, current transients are strongly dependent on

photogeneration profile and carrier concentration. In addition, electric field mobility measurements are unreliable since the applied field is linearly increasing (Juska et al. 2002). The OFET structure requires deposition of the contacts on the same plane. This leads to overestimation of mobility and also the choice of the dielectric layer affects the device performance (Cicoira et al. 2005).

Amongst all the electrical characterization techniques listed above, impedance spectroscopy (IS) offers several advantages. This technique is seen to be a very versatile method for electrical measurements of organic semiconductors and is relatively simple to implement (Xu et al. 2005, Tripathi et al. 2011, Tang et al. 2013, Xu et al. 2014, Ishihara et al. 2014). In addition, impedance spectroscopy can be used to determine mobility of charge carriers in materials with dispersive transport (Tripathi et al. 2011). Here, a small alternating voltage of the order of millivolts is superimposed on a dc bias and applied to the organic semiconductor under test. There is a linear relationship between the alternating perturbation signal and the response of the system (MacDonald 1992, Barsoukov and MacDonald, 2005).

Impedance spectroscopy essentially involves voltage and frequency dependent measurements of capacitance, admittance, phase and impedance. The terms impedance spectroscopy (IS) and admittance spectroscopy (AS) have been used interchangeably in literature (Ishihara et al. 2014, Tsang and So 2006).

In 1996, Harrison et al. investigated single layer polymer electroluminescent diodes using impedance spectroscopy, photo-impedance spectroscopy and modulated photovoltage spectroscopy. From impedance spectroscopy, they observed that for MEH-PPV devices, the impedance plot exhibited a single semicircle; whereas for PPV devices it showed two semicircles which merged into one at very high voltages. They attributed the presence of single semicircle to the absence of either a barrier layer or depletion layer and concluded that the electric field is approximately uniform throughout the polymer film. However, the other case was attributed to the presence of highly resistive barrier layer of a fixed width (of the order of 100 Å), rather than the presence of a depletion layer, for which the width would vary with applied bias. The impedance of single and double layer electroluminescent devices was investigated

using equivalent electrical circuits by Jonda and Mayer (1999). They made use of a single RC component in the equivalent circuit of single layer devices and ascribed this to a homogenous decrease in the electrical field over the entire layer thickness. On the contrary, two RC components were needed to describe the double layer devices. A microscopic model was proposed based on the results of the impedance analysis by Kim et al. (2000) to explain the enhancement of the electroluminescence efficiency of a heterostructured polymer light-emitting diode. They studied the effect of incorporating sodium sulfonated polystyrene (SSPS) ionomer on the device properties and found the optimum concentration of SPPS to be 6.7 mole %. They observed a lower relaxation frequency in SPPS devices and attributed this to increase in activation energy. The SPPS was observed to lower the work function of the cathode, thus increasing the EL efficiency. Petty et al. (2000) employed impedance spectroscopy to study the electrical properties of gas sensors and light emitting devices (LEDs) based on Langmuir–Blodgett (LB) films and to provide an insight into the electrical equivalent circuits of the multilayer device. Changes in the admittance of the gas sensing structure on exposure to different organic vapors were also observed.

The analysis of the voltage dependent capacitance (*C-V*) is considered to be the most reliable method to explain the charge transport and interface properties in organic semiconductors. The peak voltage and the peak height of *C-V* characteristics have been shown to accurately determine the injection barriers and built-in voltage of polyfluorene based single carrier devices by van Mensfoort and Coehoorn (2008). Boix et al. (2009) employed capacitance measurements to determine energy distributions of defects in the effective band gap of organic bulk heterojunctions in solar cells. Similarly, Carr and Chaudhary (2012 and 2013) carried out capacitance measurements in detail to understand the deeper defect levels in P3HT: PCBM organic photovoltaic devices. Recent studies by Tripathi and Mohapatra (2014) have demonstrated the role of interfacial density of states in the charge transport across different organic structures using *C-V* characteristics. A recent report by Weis et al. (2015) suggests an improvement in the performance of an OLED with a poly(3,4-ethylenedioxythiophene):poly(4-styrenesulfonate) (PEDOT:PSS) layer on glass substrate, which was observed from a detailed impedance spectroscopy analysis

of the charge relaxation process. They studied the charge injection and recombination mechanism using *C-V* measurement. Ray et al. (2014) reported that the interpretation of the classical Mott-Schottky analysis in the reverse-bias *C-V* measurements does not hold good in the case of organic semiconductors due to the presence of deep traps. So, they developed a new technique called forward bias *C-V* to determine the energy levels of the deep defect states in organic semiconductors. The effect on the charge carrier transport by doping titanyl phthalocyanine (TiOPc) into Alq_3 has been investigated by Ramar et al. (2014) from the *C-V* and impedance measurements. Here, the equivalent resistance of the optimized device was found to reduce with increase in doping and thereby the mobility was found to increase. Recently, Agarwal et al. (2016) proposed a simplified asymmetric capacitance test structure with a large channel length to determine mobility using *C-V* characteristics and found it comparable to the measurements using OTFT configuration.

Frequency dependent capacitance measurement is widely used to study the interfacial defects and traps in the organic devices. The bias and frequency dependent behavior of the capacitance in organic hetero-layer light emitting diodes has been studied by Berleb et al. (2001) and its origin attributed to the presence of negative interfacial charges whose number density was determined to be $6x10^{11}/cm^2$. The numerical analysis to validate the determination of charge-carrier mobility by IS measurements in the presence of localized states has been performed by Okachi et al. (2008), where the increase in capacitance at low frequencies was shown to be caused by distributed localized states. Sharma et al. (2013) characterized deep traps due to structural disorder in pentacene and copper phthalocyanine (CuPc) thin films by *C-V* and *C-f* measurements. They obtained trap parameters and energy distribution of traps from the temperature dependent capacitance studies. Zhang et al. (2013) studied the *C-V* characteristics of a 4,4'-bis[(N-carbazole)styryl]biphenyl based OLED at different frequencies. They observed that at high frequency, the capacitance is independent of voltage due to the carriers not being able to respond to the ac signal. They attributed the capacitance variation at low frequency to the redistribution of injected carriers, leading to the recombination process in the OLED. From the frequency dependent capacitance (*C-f*) and conductance (*G-f*), one can obtain negative differential

susceptance ($-\Delta B$) and differential conductance ($\omega \Delta G$) as a function of frequency, which are used to determine charge carrier mobility in organic devices. Martens et al. (2000) observed two relaxation peaks in the plot of $-\Delta B$ versus ω for a polymer light-emitting diode and ascribed it to two inductive processes arising from the transit of electrons and holes resulting from the simultaneous measurement of electron and hole mobilities. Recently, Tang et al. (2015) developed a model to determine carrier mobility of Schottky-contacted single-carrier organic devices from $-\Delta B$ and the Schottky energy barrier height. This model does not require the devices to have ohmic contacts. An in-depth analytical and experimental analysis was carried out by Tsang and So (2006) to determine carrier mobility from $-\Delta B$ in an organic semiconductor. They found their results to be comparable with those obtained from TOF technique. A notable report by Tsung and So (2009) established the advantages of $-\Delta B$ technique over time-of-flight technique for studying dispersive charge transport in organic semiconductors. Here, carrier dispersion was measured in the hole transport layer NPB in case of deep traps in the material. Recent work by Takagi et al. (2016) proposes a model using IS to simultaneously determine drift mobility and deep trapping lifetime in prototypical hole transporting organic semiconductors.

Hole mobility in the electron transport layer Alq_3 has been determined using IS measurements by Ishihara et al. (2011) using a thin layer of 4,4'-bis[N-(1-naphthyl)-N-phenyl-amino]-biphenyl (NPB) for hole-injection. They also obtained hole mobility values for double-layer devices with NPB layer thickness comparable to the Alq_3 layer, indicating that the applied field mostly acts on the Alq_3 layer. This was further examined by them in 2012 through simulations to interpret the transit-time effects in multilayer OLEDs. The same group in 2014 determined electron mobility in Alq_3 in electron-only devices using IS technique to clarify the carrier transport mechanism in OLEDs. Montero and Bisquert (2011) used IS measurements to interpret the field-dependent mobility of the carrier transport, ascribing it to traps in organic layers. The computational results confirmed the mobility enhancement with the applied electric field. The electrical properties of organic materials and their interfaces are also very well studied using impedance spectroscopy (IS). In 2006, Bisquert et al. and Pingree et al. (2007) investigated the interfacial properties in OLEDs and attributed the negative

capacitance observed in IS measurements to the role played by the dipole layer at the interface. It was also observed that density of trap states and the frequency-dependent charge transport in OLEDs depend on the quality of ITO surface. Plasma treatment of ITO anode was seen to reduce the overall resistance, resulting in improved performance of the device (Park et. al. 2007).

Ono et al. (2001) observed build-up of additional capacitance in the devices if an electrode is exposed to air. Hsieh et al. (2006) studied the effect of incorporating tungsten oxide (WO_3) into 1,4-bis[N-(1-naphthyl)-N'-phenylamino]-4,4'diamine (NPB). They observed an improvement in hole injection into the organic layer due to reduction in junction resistance. Wu et al. (2012) correlated the accumulated charges due to space-charge at the interface of organic layers with carrier mobility in OLEDs using impedance versus voltage (*Z-V*) measurements, which provide an alternate method to estimate the carrier mobility in organic materials.

In addition to the study of charge injection and transport properties in organic semiconductors, IS measurements have also been performed to probe the degradation in OLEDs. Nowy et al. (2010) demonstrated that IS measurements such as *C-V* and *C-f* can be utilized to obtain information about interfacial changes caused by degradation under electrical operation.

The electrical studies are carried out to determine factors such as charge injection, transport and recombination (Blom and Vissenberg 2000, Crone et al. 1998, Eva et al. 2010, Pivrikas et al. 2010). The physical parameters such as defects or traps governing these three factors affect the performance of these devices (Li et al. 2007, Kumar et al. 2011, Nguyen et al. 2001, Zhan et al. 2007). Martens et al. (1999) studied the dispersive transport of holes in poly(p-phenylene vinylene) as a function of frequency, temperature, dc bias and polymer thickness using AS to determine mobility. An extensive probe has been conducted by Berleb and Brütting (2002) on the trap-causing dispersive transport of electrons in tris(8-Hydroxyquinoline) Aluminum (Alq_3) using impedance spectroscopy. Sharma et al. (2011) have shown the dependence of traps in organic semiconductors on the growth conditions and surface morphology. The addition of dopant molecules in the device leads them to function either as traps or

scattering centers, thus affecting charge carrier mobility (Zhan et al. 2007, Chauhan et al. 2010). The generation of free carriers from the ionization of dopant molecules leads to an increase in the mobility and conductivity of the organic material (Tong et al. 2007). Lee et al. (2014) demonstrated that direct charge transfer from trap states of host to dopants enhances the conductivity of doped organic semiconductors.

It must be noted that if dispersion is present even at a moderate level, the frequency dependent capacitance and conductance (*C-f* and *G-f*) may not show the characteristic dip needed to determine mobility by negative differential susceptance ($-\Delta B$) and differential conductance ($\omega \Delta G$) methods, respectively (Tripathi et al. 2011). This problem can be overcome by using the frequency dependent impedance method ($|\mathrm{Im}[Z(f)]|$–f) which is not susceptible to dispersion (Tripathi et al. 2011). The doping process in pentacene Schottky diodes and the influence of charge carrier traps on doping have been studied by Pahner et al. (2013). By modulating the bias voltage at different device temperatures, the distribution of trap sites was also estimated. Mesta et al. (2014) probed the charge carrier relaxation in hole-only devices of a polyfluorene-based disordered organic semiconductor by solving a time-dependent three-dimensional master equation for the occupational probabilities of transport sites in the semiconductor. These simulations based on the data provided by IS were used to study steady state and transient charge transport.

The family of organic semiconductors can be classified into hole transporting, electron transporting, emissive, bipolar (hole and electron transporting) or multifunctional groups. Among the amorphous hole-transporting materials (HTMs), triarylamine based compounds such as *N,N*′-Di(1-naphthyl)-*N,N*′-diphenyl-(1,1′-biphenyl)-4,4′-diamine (α-NPD) constitute a very important class and are commonly used in OLED applications (Giro et al. 1999, So et al. 2007, Cheung et al. 2008, Thesen et al. 2010, Wu et al. 2016). Their chemical, thermal and structural stability makes them an ideal choice to study the physics involved in these materials. Ever since the pioneering step of Tang and Van Slyke (1987), these compounds are mainly used as HTMs (Giro et al. 1999, So et al. 2007, Wu et al. 2016) and emissive materials in OLED applications (Wee et al. 2009, Oshiro et al. 2012, Tian et al. 2014). However, they can

also be used as a hole transport component in bipolar transport materials (Tao et al. 2009, Wang et al. 2010, Fan et al. 2015). Their applications also extend to organic solar cells and organic field-effect transistors (Paek et al. 2012, Zheng et al. 2013).

Charge injection and transport on triarylamine based compounds has been studied in-depth by various research groups using different techniques, such as time of-flight (TOF), OTFT measurements, current–voltage (*J-V*) measurement, dark-injection space-charge-limited current (DISCLC) transients, and admittance spectroscopy (AS) (So et al. 2007, Cheung et al. 2008). However, there are very few reports on charge injection and transport studies of new triarylamine based compounds using impedance spectroscopy (IS). For the work reported in this thesis, the most widely used triarylamine based compound α-NPD, and novel triphenylamine (TPA) derivatives are selected to study the fundamental mechanism of charge injection and transport in single carrier devices.

1.7 SCOPE AND OBJECTIVES OF THE PRESENT INVESTIGATION

Due to the suitability of organic materials in potential flexible and large-scale electronic device applications, attention has been focused towards their development. Several researchers have carried out different investigations to study the optical and electrical properties of various organic compounds. However, detailed investigations on the optoelectronic properties of novel materials continue to be very active research areas. The balance between charge transport and luminescence is essential for efficient OLEDs. In a wide range of materials, it has been observed that organic materials having high Photo Luminescence (PL) efficiency exhibit rather low charge carrier mobility ($\sim 10^{-6}$ $cm^2V^{-1}s^{-1}$), whereas materials having large carrier mobility show much lower PL-efficiencies (Liu et al. 2015). In this regard, there is wide scope to develop organic materials showing efficient charge transport and high luminescence. The hole mobility in organic p-type materials is generally two orders of magnitude greater than electron mobility (Helander et al. 2008). In addition, organic p-type materials are easier to synthesize than organic n-type materials, owing to the former's electron-rich conjugation (Shan and Miao 2017). Understanding the elementary processes involved in charge carrier transport mechanism in organic materials is essential to design new

materials with improved properties. This can be achieved by designing interfaces with low defect density and appropriate device configurations. The study of structure-property relationship facilitates development of efficient organic devices.

The present work focuses on the experimental investigation of the charge injection and transport of few p-type triarylamine based compounds, such as α-NPD and novel TPA derivatives in hole-only device structures, as well as the optical properties of the TPA derivatives in thin films. Studies on the well-known hole transport material α-NPD are used as a reference to study the properties of novel TPA derivatives. The investigations were carried out employing measurements such as current density-voltage (*J-V*), capacitance-voltage (*C-V*), frequency dependent capacitance (*C-f*), conductance (*G-f*) and impedance. *J-V* measurements were performed to study the dependence of the turn-on voltage and current density through the device on the organic layer thickness and molecular substitutions. The hole mobility of the TPA molecules was determined from the space-charge-limited current density. The *C-V* measurements were done to identify the presence of traps in the device and to interpret the behavior of carriers at the interfaces. The dielectric constants of the organic materials were determined from the *C-f* measurements. *G-f* measurements were performed to study the dependence of the conductance through the device on the organic layer thickness. The nature of charge transport was determined from the frequency dependent *ac* conductivity measurements. The impedance measurements were used to determine the hole mobility of the organic materials.

In addition to these measurements, the role of side groups (alkyl substitution in the molecular structure) on the optical and electrical properties of the novel TPA derivatives is also investigated through UV-Vis and Photoluminescence (PL) spectroscopy. UV-Vis spectroscopy was used to determine the optical absorption by the TPA molecules and to confirm the presence of intermolecular interactions in the molecules. PL spectroscopy was used to determine the excited state fluorescence of the TPA molecules and their PL quantum efficiency.

2,3,5,6-tetrafluoro-7,7,8,8-tetracyanoquinodimethane (F_4TCNQ) was used as the hole injection material in these devices. In all the experiments, frequency dependent

complex impedance, capacitance and conductivity along with voltage dependent capacitance (*C-V*) were measured at room temperature using Agilent E4980A Precision LCR Meter in the frequency range 20 Hz-1 MHz applying a dc bias (typically ± 0-5 V or ± 0-10 V) over which an *ac* voltage of 100 mV at 500 Hz was superimposed. *J-V* measurements were carried out using computer-controlled Keithley 2400 SMU. The photophysical characterization was carried out using UV-Vis (Ocean Optics Inc. SD 2000) and PL (Fluoromax-4 TCSPC Horiba JobinYvon) Spectrometers. All measurements on the devices were carried out immediately after their fabrication keeping them in open air.

The main research objectives of this thesis were:

1. To investigate the efficiency of F_4TCNQ layer to inject holes into the α-NPD layer as a function of the thickness of F_4TCNQ film using capacitance, conductance and impedance measurement methods.
2. To determine the effect of variation of the thickness of α-NPD layer on its hole mobility using frequency dependent capacitance, conductance and impedance methods. Further, examine the role of defect density in this layer on hole mobility.
3. To fabricate hole-only device using α-NPD as hole transport material and F_4TCNQ as hole injection material. The devices were fabricated by employing physical vapor deposition (PVD) method.
4. To study the role of different side-groups attached to novel TPA derivatives in hole transport mechanisms using capacitance, conductivity and impedance methods along with UV-Vis and PL spectroscopy.
5. To fabricate hole-only device using novel TPA derivatives by employing PVD, with F_4TCNQ film as hole injection layer and α-NPD film as hole transport layer.

1.8 OUTLINE OF THE THESIS

The research work in this thesis is divided into 5 chapters.

Chapter 1 and its sub-sections provide the background and motivation for the present work. The chapter also includes a general introduction to organic semiconductors along with their charge injection and transport mechanism. It also provides a summary of the literature review on charge transport in organic semiconductors using impedance spectroscopy as well as capacitance and conductance measurements. An insight to the scope and objectives of the present work is given at the end of the chapter.

Chapter 2 provides the details of experimental techniques used in the present work. The first section gives the details about the substrate preparation and device fabrication by physical vapor deposition technique. The second section contains an introduction to the techniques of device characterization, their theoretical description and formulae used for calculations. The experimental setup used in our laboratory for the characterization of the fabricated devices is also presented.

Chapter 3 discusses the charge injection and transport properties of the hole transport material α-NPD in hole-only devices using measurements of current density, capacitance, conductance and impedance spectroscopy. The first section describes the investigation of the charge injection properties in α-NPD with F_4TCNQ as hole-injection layer. In the second section, the thickness dependent charge transport properties of α-NPD are investigated.

Chapter 4 presents the investigation of electrical and optical properties of novel compounds bearing electron donating TPA moiety through measurement of current density, capacitance, *ac* conductivity, Impedance spectroscopy, UV-Vis spectroscopy and PL spectroscopy. The three compounds differ in their side groups to the TPA moiety, and the effect of this side group substitution on their electrical and optical properties has been investigated. In order to better understand the charge transport, the effect of molecular structural dynamics of the compounds on their charge transfer kinetics is also analyzed.

Chapter 5 summarizes the conclusions drawn from the present work. Next, the scope for further work in this field is mentioned.

An appendix followed by list of references and a brief profile with publications in international journals and conferences are presented at the end of the thesis.

CHAPTER 2

EXPERIMENTAL TECHNIQUES

Abstract

This chapter describes the experimental techniques employed to fabricate and characterize the single carrier devices. The basic operating principle of each of the experimental techniques is described in brief and the formulae used to determine various parameters are presented. The experimental setup used in this study is described in detail.

2.1 DEVICE FABRICATION

The fabrication procedure involves substrate preparation with UV- ozone surface treatment, and physical vapour deposition (PVD) of the organic materials and aluminum (Al) as cathode.

2.1.1 Substrate Preparation

Glass plate having patterned indium tin oxide (ITO) as anode on one surface is used as the substrate onto which the organic layers and aluminum are deposited. The ITO coated glass substrate was procured from XinYan Technology Ltd., Hong Kong. Prior to the deposition, ITO coated glass substrates with a sheet resistance of 15Ω/□ are sequentially ultrasonicated using acetone, isopropyl alcohol, DI water for 15 min each and dried in flowing dry nitrogen (purity 99.99%), which is followed by UV-Ozone treatment for 15 min. The substrates are handled in a work bench with filtered laminar flow air supply to ensure processing in nearly dust-free environment.

2.1.2 UV - Ozone Treatment

UV-Ozone treatment of the cleaned and dried substrates is carried out to ensure the decomposition of contaminants by UV irradiation and oxidation due to ozone (O_3).

The ITO substrates which are wet cleaned to remove inorganic contaminants are subjected to UV-O_3 treatment for 15 min (Li et al. 2005) to remove organic contaminants. This results in increase in the work function of ITO, thereby reducing the barrier for hole injection. The schematic of the UV-O_3 process is shown in figure 2.1 (a). The UV-O_3 treatment is carried out using the chamber shown in figure 2.1 (b).

(a)

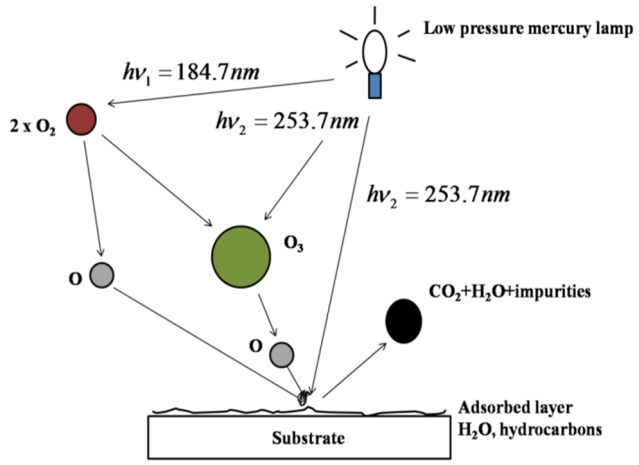

Figure 2.1 (a) Schematic representation of the UV-O_3 treatment process (Kern 1993)

(b)

Figure 2.1 (b) UV-O_3 chamber

The low-pressure mercury vapor lamp (UVC) used in our work emits UV radiations of wavelengths 184.7 nm and 253.7 nm. Light at wavelength 184.7 nm reacts with atmospheric oxygen (O_2) to yield two atoms of oxygen (O + O). One of the atomic oxygen (O) reacts with atmospheric oxygen (O_2) to yield ozone (O_3). Light at wavelength 253.7 nm reacts with ozone and decomposes it into atomic oxygen with

strong oxidizing ability. The contaminant molecules also react with light at wavelength 253.7 nm and undergo photolysis to yield ions, free radicals, excited and neutral molecules which in turn lead to decomposition of organic contaminants.

2.1.3 Physical Vapor Deposition (PVD)

The cleaned substrates are loaded into the vacuum evaporation chamber having a turbo-molecular pump backed by a dry scroll pump, for the sequential deposition of all organic layers and cathode layer without breaking the vacuum. The schematic of the vacuum evaporation chamber is shown in figure 2.2 (a).

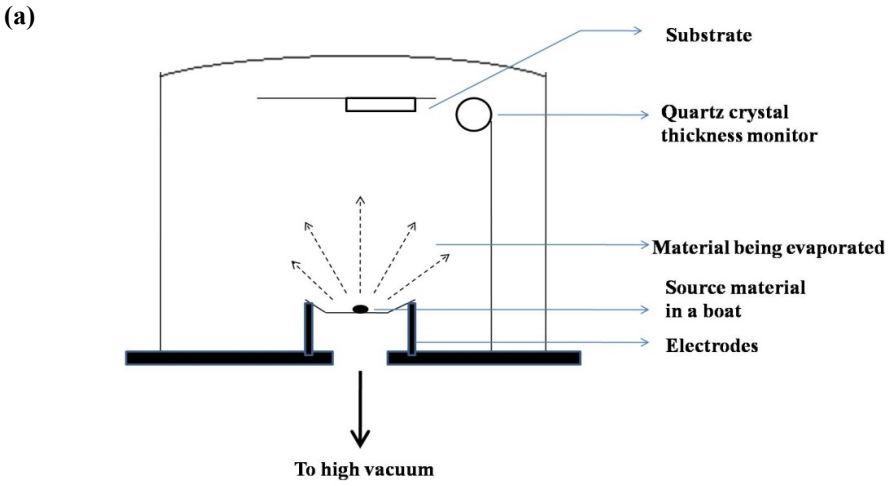

Figure 2.2 (a) Schematic of a vacuum chamber of the PVD system

The PVD system used in this study is shown in figure 2.2 (b), and figure 2.2 (c) shows the interiors of the chamber used for device fabrication. Organic layers and aluminum are thermally evaporated at a base pressure maintained at ~10^{-6} mbar. Aluminum is deposited using a shadow mask of 0.8 mm wide strips. The active area of the device is 1.6 mm^2.

The PVD system used for deposition is equipped with *in-situ* sensors for monitoring the rate of deposition and thickness of the deposited film. The evaporator also has facility to evaporate all organic layers and aluminum layer without breaking the vacuum. The rate of deposition is fixed at ~ 1-2 Å/s for organics and ~ 5 Å/s for aluminum. The thickness of the layers is of the order of several nm.

(b) **(c)**

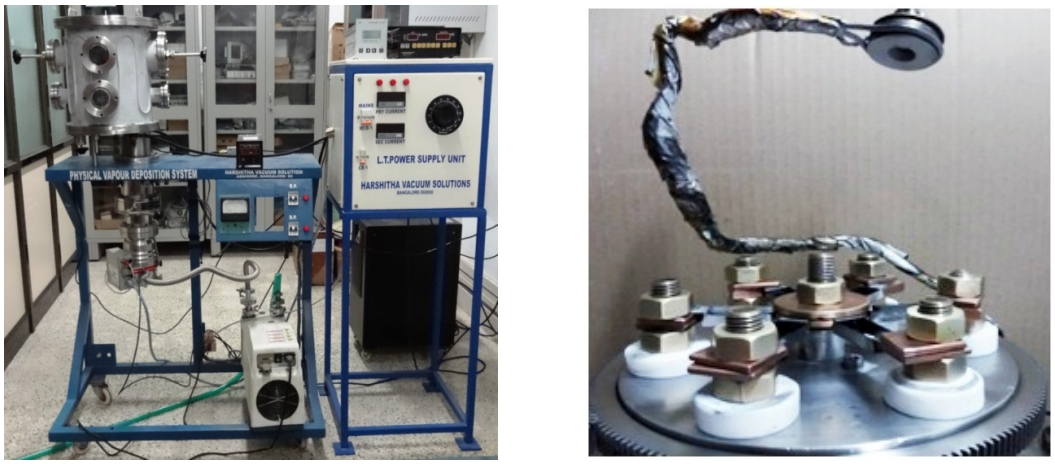

Figure 2.2 (b) The PVD system and **(c)** Interior of the evaporation chamber showing the six boat assembly

2.2 DEVICE CHARACTERIZATION

The characterization includes the following measurements on different organic devices to determine various electrical properties of the organic semiconductors used in the study.

2.2.1 Current Density-Voltage (*J-V*) Characteristics

2.2.1.1 Introduction

The current through the device is determined primarily by three factors namely, charge injection, charge transport and recombination of charge carriers. While charge injection depends mainly on the energy barrier between the contact and the organic semiconductor, the transport and recombination depend on the material properties of the organic layer (Crone et al. 1998).

2.2.1.2 Theoretical Basis for *J-V* Characteristics

In single carrier devices, only charge injection and transport are considered. These devices are generally used to assess the process of current flow in an organic

semiconductor diode with one of the electrodes forming an ohmic contact and the other forming a non-ohmic contact (Brütting et al. 2001). The difference in the work function of the two electrodes is the built-in voltage (V_{bi}) across the organic semiconductor, resulting in the build-up of internal electric fields.

In the case of hole-only devices, the application of a positive bias larger than the built-in voltage on the anode results in a positive electric field directed towards the cathode. This results in a drift current due to injection of only holes from the anode and is limited by the space charge created by the holes. This space-charge-limited current is described analytically by the Mott–Gurney (1940) equation as follows

$$J = \frac{9}{8}\mu\varepsilon_r\varepsilon_0\frac{(V-V_{bi})^2}{d^3} \tag{2.1}$$

where μ and ε_r are mobility and dielectric constant of the material, ε_0 is the permittivity of vacuum, d is the distance between the contacts, V is the applied voltage and V_{bi} is the built-in voltage of the device.

At bias voltages lower than V_{bi}, the electric field is negative and directed towards the anode. This leads to a negative drift current due to injected holes. However, at bias voltages greater than V_{bi}, this current is negligible compared to the positive current due to diffusion of holes towards the cathode.

In the case of single carrier devices, the flow of current through the device can be limited due to three major factors, i.e., injection, space-charges and traps. The current is said to be injection-limited (ILC) if the metal-organic interface barrier is greater than 0.3 eV at zero electric field (Varo et al. 2012), wherein the injection of charges from the metal into the organic is limited by this barrier. This behavior is observed at very low voltages, when the number of injected carriers is low compared to the existing thermally generated carriers and impurities in the device (Varo et al. 2012). Therefore, the metal-organic interface behaves as an ohmic contact, leading to a linear graph in Region I of figure 2.3. However, if the barrier is less than 0.3 eV, current due to the easily injected charges can be limited by their bulk transport through the device.

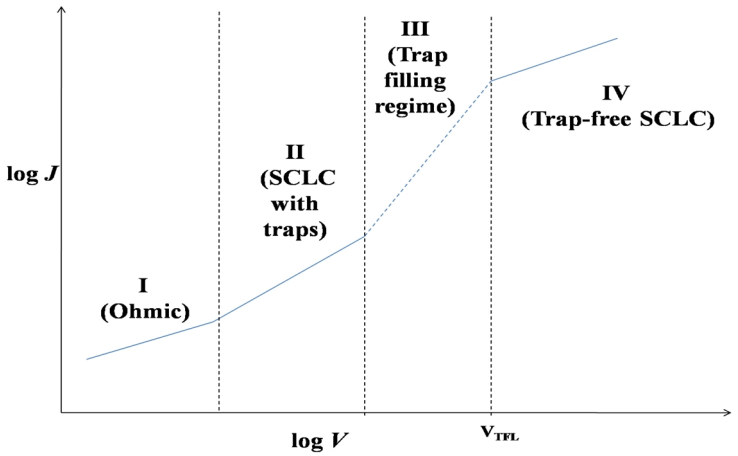

Figure 2.3 Typical *J-V* characteristics showing behavior of current in different regimes

The accumulation of these injected charges at the metal-organic interface leads to the formation of space-charge due the slow charge transport through the organic layer. The injected charges fill a finite number of low-lying trap energy states and this current is called space-charge limited current (SCLC) as shown by Region II. Region III shows the trap filling regime. The current in this regime follows a nonquadratic relation with the applied voltage.

Beyond a critical voltage (also called trap filled limit voltage V_{TFL}) all the traps are filled, and at very high voltages the current follows a quadratic relation with the applied voltage (Region IV). This is called the trap-free space-charge limited current. The different regimes of the current-voltage characteristics depend on the interfaces as well as the impurities and traps present in the organic semiconductor (Stallinga 2009).

2.2.1.3 Experimental Setup for *J-V* Characteristics

The current-voltage measurement setup used for the electrical characterization of organic devices consists of a computer-controlled Keithley 2400 Sourcemeter. The schematic of the measurement setup used is shown in figure 2.4 (a), and figure 2.4 (b) shows the Keithley 2400 Sourcemeter measurement setup used in this study.

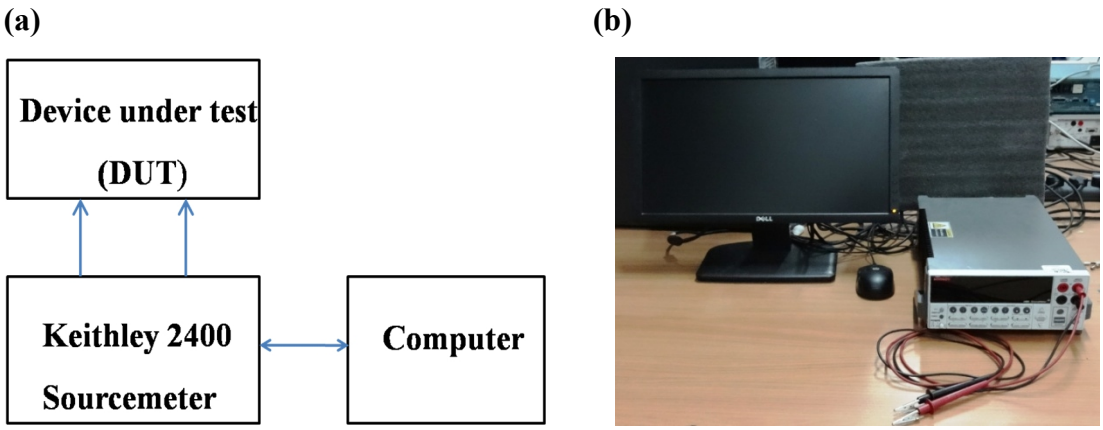

Figure 2.4 (a) Schematic of the current-voltage measurement setup and **(b)** Keithley 2400 Sourcemeter measurement setup

The Keithley 2400 Sourcemeter (SMU) functions as a highly stable dc power source as well as digital multimeter. The device under test (DUT) is connected to the SMU and a range of dc voltages (sweep) is applied while simultaneously measuring the current through it. The SMU is interfaced to the computer through IEEE-488 USB-to-GPIB Interface Adapter and measurements are performed using Keithley Labtracer v2.0 I-V curve tracing application software.

2.2.2 Impedance Spectroscopy (IS)

2.2.2.1 Introduction

The electrical properties and dynamics of organic semiconductor materials at the metal-organic interface or in their bulk form can be easily investigated using a relatively new and powerful electrical characterization method called Impedance Spectroscopy (IS). This is a purely electrical and non-destructive technique which does not require expensive experimental setup.

The general approach in Impedance Spectroscopy of organic semiconductors is to apply an external stimulus (*ac* voltage or current) to the electrodes and observe the response. The nature of the external stimulus can be varied and the standard approach is to apply a single-frequency voltage or current to the interface and measure the phase

shift and amplitude, or real and imaginary parts of the resulting current at that frequency, using either analog circuit or fast Fourier transform (FFT) analysis of the response (Barsoukov and Macdonald 2005).

2.2.2.2 Theoretical Basis for IS

In impedance spectroscopy measurements, a small sinusoidal voltage $v(t) = V_m\sin(\omega t)$ of amplitude V_m and frequency $\omega = 2\pi f$ is applied to the sample along with a constant bias voltage V. The response of the sample is given by the resulting measured current $i(t) = I_m\sin(\omega t+\phi)$ with a phase shift ϕ and amplitude I_m. The small sinusoidal voltage is in the order of millivolts so that the current response is almost linear and does not perturb the sample very much. For purely resistive behavior, $\phi = 0$. When the system involves capacitive and inductive elements, the relation between the properties of the system and its response to the external stimuli becomes very complex in time domain. The frequency dependent complex impedance $Z(\omega)$ is defined according to Ohm's law as the ratio of the complex voltage $V(\omega)$ to complex current $I(\omega)$ and is given by the following expression

$$Z(\omega) = \frac{V(\omega)}{I(\omega)} = \mathrm{Re}[Z(\omega)] + i\,\mathrm{Im}[Z(\omega)] \tag{2.2}$$

where $\mathrm{Re}[Z(\omega)]$ is the real part and $\mathrm{Im}[Z(\omega)]$ is the imaginary part of the complex impedance. The plot of $-\mathrm{Im}[Z(\omega)]$ versus $\mathrm{Re}[Z(\omega)]$ is called as the Cole – Cole plot and is shown in figure 2.5.

The modulus $|Z(\omega)|$ is given by the expression

$$|Z(\omega)| = \sqrt{\{(\mathrm{Re}[Z(\omega)])^2 + (\mathrm{Im}[Z(\omega)])^2\}} \tag{2.3}$$

and the phase angle is given by the following expression

$$\phi = \tan^{-1}\left(\frac{\mathrm{Im}[Z(\omega)]}{\mathrm{Re}[Z(\omega)]}\right) \tag{2.4}$$

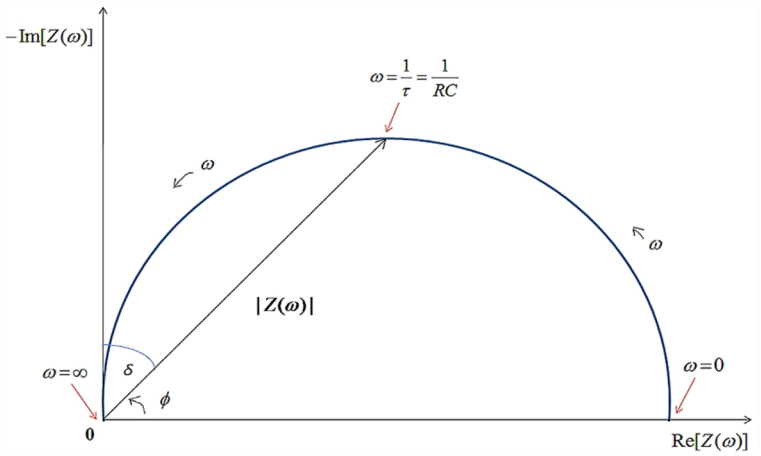

Figure 2.5 Cole – Cole plot

The IS data is represented and modeled using different equivalent circuits consisting of resistors and capacitors, depending on the structure and type of devices studied.

The *RC* circuit as shown in figure 2.6 consisting of a resistor R_S in series with a parallel resistor R_P and parallel capacitor C_P is used to represent a single semicircle of radius $R_P/2$ and height $\tau = 1/R_P C_P$ in the Cole - Cole plot. The negligible value of series resistor R_S can be obtained from the distance between the origin and $\omega = \infty$ on the x-axis of the Cole – Cole plot.

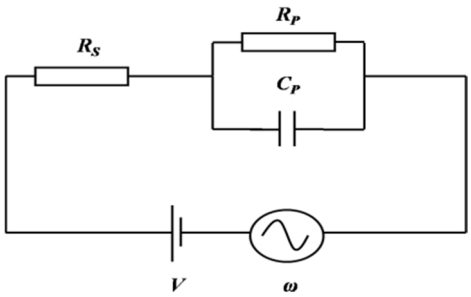

Figure 2.6 Equivalent circuit model

The values of R_P and C_P are given by the following equations:

$$R_P = (\mathrm{Re}[Z(\omega)] - R_S) + \frac{(\mathrm{Im}[Z(\omega)])^2}{(\mathrm{Re}[Z(\omega)] - R_S)} \qquad (2.5)$$

$$C_P = -\left(\frac{1}{\omega R_P}\right) + \frac{(\mathrm{Im}[Z(\omega)])}{(\mathrm{Re}[Z(\omega)] - R_S)} \tag{2.6}$$

The real and imaginary parts of the complex impedance in terms of the time constant can be derived from the *RC* circuit (ignoring inductive reactance X_L).

$$Z(\omega) = \frac{R_P i(-X_C)}{R_P + i(-X_C)} \tag{2.7}$$

$$Z(\omega) = \frac{R_P(-iX_C)}{R_P - iX_C} \cdot \left(\frac{R_P + iX_C}{R_P + iX_C}\right) = \frac{R_P {X_C}^2 - i{R_P}^2 X_C}{{R_P}^2 + {X_C}^2} \tag{2.8}$$

$$Z(\omega) = \frac{R_P {X_C}^2}{{R_P}^2 + {X_C}^2} - \frac{i{R_P}^2 X_C}{{R_P}^2 + {X_C}^2} \tag{2.9}$$

$$X_C = \frac{1}{\omega C_P} \text{ and } \omega_0 = \frac{1}{R_P C_P} \tag{2.10}$$

Considering a series resistor R_S in the circuit, the complex impedance can then be written as

$$Z(\omega) = R_S + \frac{R_P}{1 + \left(\frac{\omega}{\omega_0}\right)^2} - \frac{iR_P\left(\frac{\omega}{\omega_0}\right)}{1 + \left(\frac{\omega}{\omega_0}\right)} \tag{2.11}$$

The real part of equation (2.9) can be written as

$$\mathrm{Re}[Z(\omega)] = \frac{\frac{R_P}{(\omega C_P)^2}}{{R_P}^2 + \frac{1}{(\omega C_P)^2}} = \frac{R_P}{1 + (\omega\tau)^2} \tag{2.12}$$

Similarly, the imaginary part is written as

$$\mathrm{Im}[Z(\omega)] = -\frac{\omega\tau R_P}{1+(\omega\tau)^2} \tag{2.13}$$

The complex impedance $Z(\omega)$ of the device can also be represented in terms of its capacitance C and conductance G as shown in the equations below:

$$C = \frac{1}{2\pi f}\cdot\left[\frac{-\mathrm{Im}[Z(\omega)]}{(\mathrm{Re}[Z(\omega)])^2+(\mathrm{Im}[Z(\omega)])^2}\right] \tag{2.14}$$

$$\frac{G}{\omega} = \frac{1}{2\pi f}\cdot\left[\frac{\mathrm{Re}[Z(\omega)]}{(\mathrm{Re}[Z(\omega)])^2+(\mathrm{Im}[Z(\omega)])^2}\right] \tag{2.15}$$

Dielectric materials have the tendency to absorb some of the energy when an *ac* signal is applied. This value is called Dissipation factor (D) which is related to the loss and is a critical parameter in dielectric measurements. It can also be written as tan δ (loss tangent), where δ is called the loss angle measured in radians (equal to $\pi/2 - \phi$). The loss tangent is given by the following equation: (see Agilent Impedance Measurement Handbook-A guide to measurement technology and techniques, 4th edition, page 1-10)

$$\tan\delta = \frac{1}{\omega C_P R_P} \tag{2.16}$$

The loss tangent is also written as (Schönhals 1998)

$$\tan\delta = \frac{\varepsilon''}{\varepsilon'} \tag{2.17}$$

where ε' and ε'' are the real and imaginary parts of the complex dielectric constant; ε'' is also known as dielectric loss factor. The value of loss tangent (dissipation factor D) that can be measured in Agilent E4980A Precision LCR Meter is ± 0.000001 to 9.999999 (see Appendix I for Agilent E4980A Precision LCR Meter 20 Hz to 2 MHz Data Sheet). The variation of loss tangent with frequency depends on the material properties, and gives information regarding the relaxation process (Lee et al. 2003).

2.2.2.3 Experimental Setup for IS

The impedance spectroscopy measurement setup used for the electrical characterization of organic devices consists of computer-controlled Agilent E4980A Precision LCR meter. The schematic of the measurement setup is shown in figure 2.7 (a), and figure 2.7 (b) shows the Agilent E4980A Precision LCR meter setup used in this study.

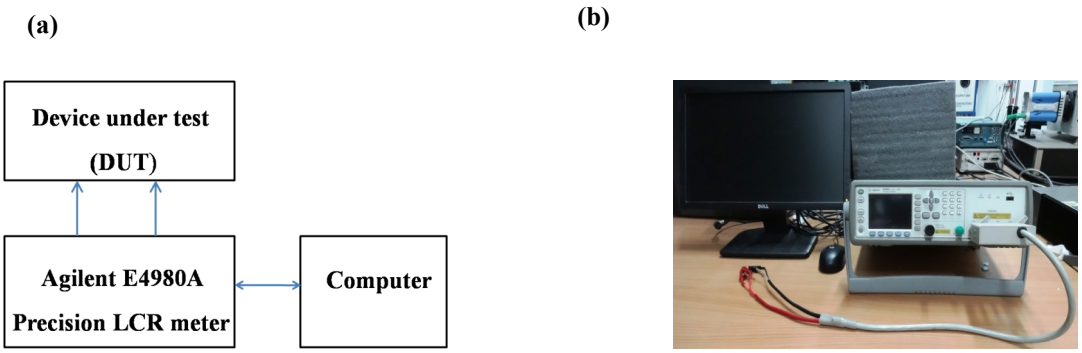

Figure 2.7 (a) Schematic of the IS measurement setup and **(b)** Agilent E4980A Precision LCR meter measurement setup

As mentioned earlier, a small *ac* voltage superimposed on a dc bias is applied to a DUT, and the resulting current across the DUT is measured along with the phase angle between the voltage and current. The ratio of voltage to current gives the magnitude of the impedance. The DUT is modeled using an equivalent circuit consisting of resistors, capacitors and inductors. The measurements are performed with a frequency sweep of 20 Hz to1 M Hz.

2.2.2.4 Impedance Measurements

The frequency dependence of the real and imaginary parts of impedance is shown in figure 2.8 below. The real part of impedance [Re $Z(\omega)$] decreases with increasing frequency, while the imaginary part of impedance [-Im $Z(\omega)$] shows a peak at a particular frequency called the relaxation frequency (ω_{max}), where the relaxation time $\tau = 1/\omega_{max}$ is used to calculate the mobility of charge carriers in the device. The Cole-Cole plot is obtained when Re $Z(\omega)$ is plotted on the x-axis and -Im $Z(\omega)$ is plotted on the y-axis, as explained in section 2.2.2.2.

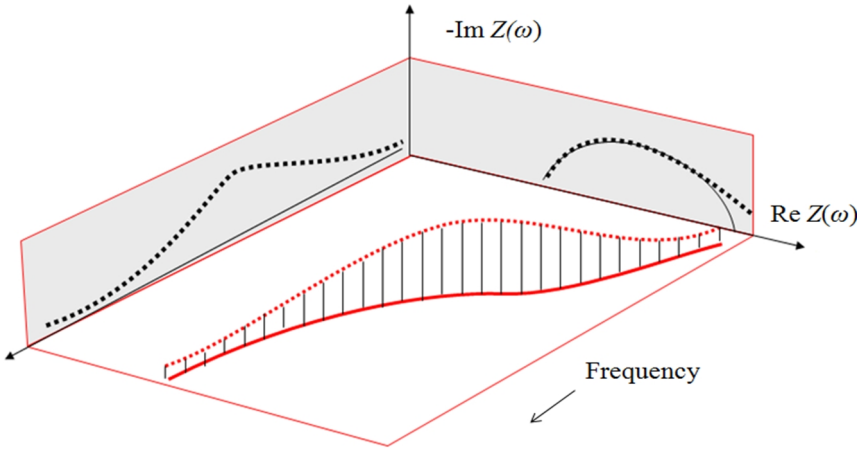

Figure 2.8 Typical characteristics of frequency dependent real and imaginary parts of impedance

2.2.3 Capacitance-Voltage (*C-V*) Characteristics

2.2.3.1 Introduction

Measurement techniques such as Capacitance-Voltage (*C-V*) have gained prominence due to their sensitivity to charge transport behavior in organic semiconductors (Brütting et al. 2001). The experimental setup and measurement of *C-V* characteristics are the same as in section 2.2.2.3.

2.2.3.2 Theoretical Basis for *C-V* Characteristics

Trapped carriers are considered to be the cause for the *C–V* peak (Figure 2.9) at higher bias voltages (Sharma et al. 2013). On applying an external bias, carriers are injected and get trapped in organic semiconductor films close to the interface, creating an interfacing electric field.

The accumulation of these carriers increases the diffusion capacitance and as the voltage increases due to the drift, they move further into the organic semiconductor layer. This causes the capacitance to reduce. So, this capacitance peak demarcates the diffusion dominated transport at lower voltages from the drift dominated transport at higher voltages (Tripathi and Mohapatra 2014).

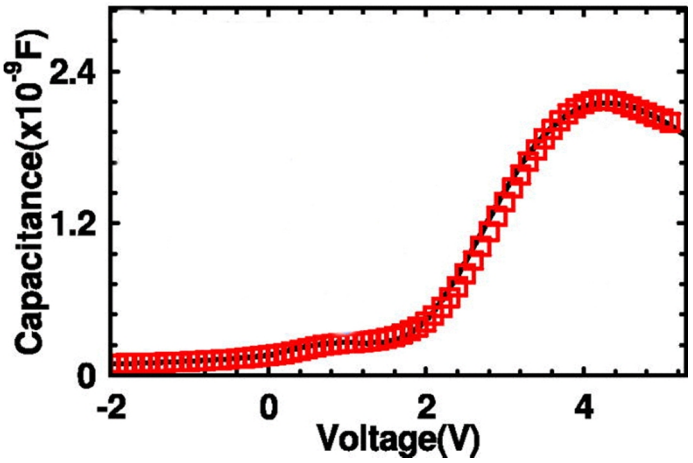

Figure 2.9 *C-V* characteristics of Al/CuPc/Au sandwiched devices at 200 Hz in which organic thin films of thickness 200 nm are grown with a deposition rate of 20 Å/s [reproduced from (Sharma et al. 2013)]

The magnitude of this capacitance is given by the following equation (Tripathi and Mohapatra 2013)

$$C_{diff} = \frac{qAp_0 d}{2}\left(\frac{k_B T}{q}\right)^{1/2}(V - V_{bi})^{-3/2} \tag{2.18}$$

where C_{diff} is the diffusion capacitance for a device of area A and organic layer thickness d at temperature T, p_0 is the carrier density due to accumulation in a narrow region at the injecting contact, q is the electronic charge, V is the applied voltage and V_{bi} is the built-in voltage of the device.

2.2.4 Capacitance-Frequency (*C-f*) and Conductance-Frequency (*G-f*) Characteristics

2.2.4.1 Introduction

The frequency dependence of the capacitance and conductance yields information on the type of charge transport, interfacial behavior and relaxation processes in the device upon application of a small *ac* bias in the order of a few hundred millivolts. The experimental setup and measurement of *C-f* and *G-f* characteristics are the same as shown in section 2.2.2.3.

2.2.4.2 Theoretical Basis for *C-f* and *G-f* Characteristics

The geometric capacitance of the device is given by the following expression (Tripathi and Mohapatra 2014)

$$C_{geo} = \frac{\varepsilon_0 \varepsilon_r A}{d} \tag{2.19}$$

where ε_0 is the permittivity of free space, ε_r is the dielectric constant, approximately 3 for organics and A is the area of the device with layer thickness d.

The frequency dependent capacitance (*C-f*) characteristics [Figure 2.10 (a)] show no change in the capacitance value when there is no external applied voltage, which corresponds to the geometric capacitance.

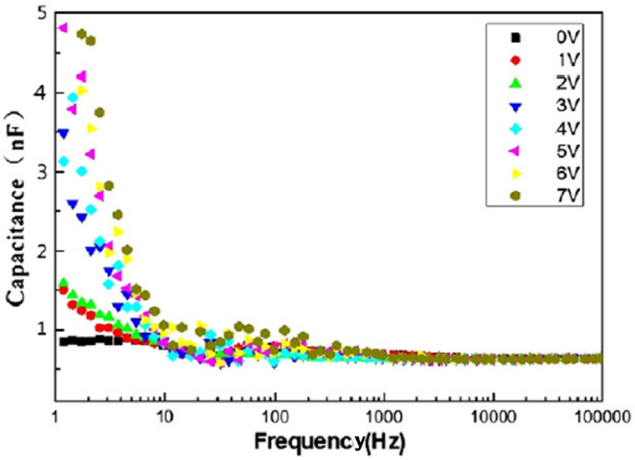

Figure 2.10 (a) Capacitance spectra of ITO/NPB/Ag devices under different bias voltages [reproduced from (Xu et al. 2014)]

When the external voltage is applied to the device, there is a rise in capacitance at lower frequencies which increases in magnitude for higher voltages. This can be attributed to the increase in the charge carrier injection and accumulation at the interface (Nowy et al. 2010). As observed in Figure 2.10 (a), at higher frequencies (> 1 kHz), the capacitance reduces to its geometric value since the dipoles and localized charge carriers will not be able to follow the electric field direction (Nguyen et al. 2007, Sharma et al. 2013). The threshold frequency at which it drops to the geometric

capacitance also increases with bias voltage. The shift in the threshold frequency towards higher value in *C-f* characteristics is due to the increase in the conductance through the device with applied voltage, which is reflected in the conductance-frequency (*G-f*) characteristics [Figure 2.10 (b)] and attributed to the increase in the number of charge carriers.

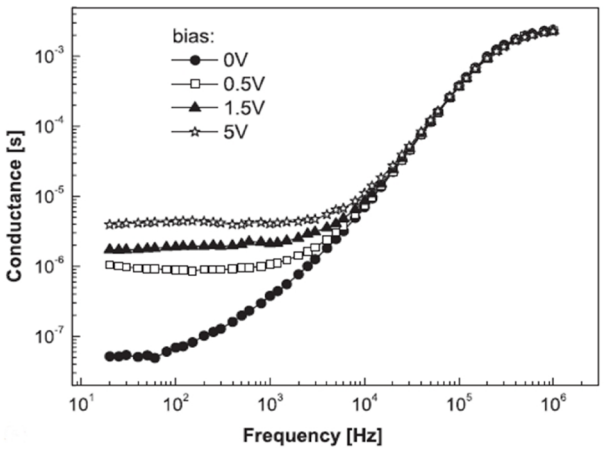

Figure 2.10 (b) Frequency dependence of conductance of ITO/NPB/Al at different bias [reproduced from (Xu et al. 2005)]

At any particular voltage, the conductance remains constant till a certain frequency called threshold frequency, and increases beyond this value [~10^4 Hz for 5 V in Figure 2.10 (b)]. Similar to *C-f*, this threshold frequency shifts to higher frequencies with bias voltage. At higher frequencies, the conductance attains the same maximum value for all bias voltages, since the dipoles and localized charge carriers will not be able to follow the rapidly oscillating electric field.

From the *G-f* characteristics, in order to calculate certain parameters related to the conduction mechanism, the conductance (G) can also be expressed in terms of conductivity (σ). These parameters, namely, the density of localized states [$N(E_f)$] at the Fermi energy E_f, the energy W_m required by a charge carrier to move from one site to another, and the minimum hopping length R, can be calculated from the following expressions, provided the frequency dependent conductivity exhibits a slope s ($0 < s < 1$), (Suman et al. 2009).

$$\sigma(\omega) = \frac{\pi^3}{24} \cdot [N(E_f)]^2 \cdot \varepsilon_0 \varepsilon_r \omega R^6 \tag{2.20}$$

$$R = \frac{e^2}{\pi \varepsilon_0 \varepsilon_r} \left[W_m - k_B T \ln\left(\frac{1}{\omega \tau_0} \right) \right]^{-1} \tag{2.21}$$

$$s = 1 - \frac{6 k_B T}{W_m - k_B T \ln\left(\frac{1}{\omega \tau_0} \right)} \tag{2.22}$$

where τ_0 is the effective relaxation time, e is the electronic charge, k_B is Boltzmann's constant and T is the absolute room temperature. At higher frequencies, the conductivity attains a constant value for all voltages as mentioned earlier.

The charge carrier hopping rate can then be calculated using the following expression (Navamani and Senthilkumar 2014, 2015)

$$\sigma(\omega) = \frac{3}{5} \varepsilon_0 \varepsilon_r \frac{\partial p}{\partial t} \tag{2.23}$$

where ε_0 is the permittivity of free space, ε_r is the dielectric constant of the organic layer and $\partial p/\partial t$ is the charge transfer rate.

Using the frequency dependent charge transfer rate, the coefficient of charge carrier hopping rate and the dynamic state factor are evaluated. These factors enable an analysis of the effect of molecular structural oscillations on charge transfer kinetics in the devices.

2.3 PHOTOPHYSICAL CHARACTERIZATION

The photophysical characterization of organic molecules is performed using UV-Vis and Photoluminescence (PL) spectroscopy. In this thesis, these studies are performed on novel TPA compounds.

2.3.1 UV-Vis Absorption spectroscopy

The existence of intermolecular interactions is confirmed by the UV-Vis absorption spectra of the organic molecules in solution and thin film. The absorption spectrum is recorded using a UV-Vis spectrometer (Ocean Optics Inc SD2000) at room temperature.

2.3.2 Photoluminescence (PL) spectroscopy

The excited state property of the molecules is studied using photoluminescence (PL) spectroscopy by exciting the samples in the form of solution or thin film, using the wavelength of peak absorption. At room temperature, steady state PL spectra and quantum yield measurements in the visible region are recorded using Fluoromax-4 TCSPC spectrophotometer (Horiba Jobin Yvon) shown in Figure 2.11.

Figure 2.11 Fluoromax-4 TCSPC spectrophotometer (Horiba Jobin Yvon)

The PL quantum yield of the organic compounds dissolved in hexane is determined relative to 9,10-diphenyl anthracene (quantum yield = 0.95 in cyclohexane).

CHAPTER 3

ELECTRICAL STUDIES ON HOLE INJECTION AND TRANSPORT IN α- NPD WITH F_4TCNQ AS HOLE INJECTION LAYER

Abstract

This chapter explores the charge transport properties of a thin film of N,N′-Di(1-naphthyl)-N,N′-diphenyl-(1,1′-biphenyl)-4,4′-diamine (α-NPD) in hole-only devices with 2,3,5,6-tetrafluoro-7,7,8,8-tetracyanoquinodimethane (F_4TCNQ) as the hole injection layer. For this purpose, variation of current density with bias voltage, capacitance with voltage, capacitance and conductance with frequency were measured. Further, impedance spectroscopy measurements were also carried out to obtain the Cole-Cole plot for further theoretical analysis. In section 3.1, we discuss hole injection properties, and in section 3.2, the hole transport properties of the device.

3.1 HOLE INJECTION IN α-NPD: F_4TCNQ HOLE-ONLY DEVICE: THICKNESS DEPENDENCE

3.1.1 Introduction

The efficiency of an OLED depends critically on charge injection, charge transport and electron-hole recombination in the multi-layered devices. It is necessary to use organic materials having high values of such parameters. A widely used hole transport material is *N,N*′-Di(1-naphthyl)-*N,N*′-diphenyl-(1,1′-biphenyl)-4,4′-diamine, also termed α-NPD. In Sec. 3.1, an investigation of the hole transport property of a thin film of α-NPD in a hole-only device is presented. This study enables us to get a better understanding of multi-layered OLED device structures (Tripathi and Mohapatra 2014). An ohmic contact is necessary to efficiently inject charge carriers in the device (Fischer et al. 2014). The well-known hole-injection material 2,3,5,6-tetrafluoro-

7,7,8,8-tetracyanoquinodimethane (F_4TCNQ) plays a crucial role in forming a nearly ohmic contact between ITO anode and α-NPD by lowering the energy barrier between them (Rana et al. 2012, Tyagi et al. 2013).

The dependence of the hole transport efficiency with the thickness of the F_4TCNQ layer is also investigated. Since it is a hole-only device, we may neglect electron-hole recombination in the analysis of the device. The injection of electrons by the metal electrode is prevented by the large potential barrier with the lowest unoccupied molecular orbital (LUMO) of α-NPD. The charge transport properties are evaluated by *J-V* and *C-V* measurements and impedance spectroscopy techniques. It is shown that the hole injection into α-NPD increases with 4 nm F_4TCNQ thickness by correlating the current density - voltage, capacitance - voltage, capacitance – frequency, conductance - frequency and impedance measurements.

3.1.2 Fabrication and Characterization of Hole-only Devices

High quality F_4TCNQ (> 99 %) and α-NPD (> 99.5 %) were obtained from M/s. Sigma Aldrich, USA, and were used without any further purification. In this investigation, devices with four different configurations (**D_0**, **D_1**, **D_4** and **D_6**) have been fabricated. Patterned indium tin oxide (ITO) was used as the bottom anode, F_4TCNQ was used as a hole injection material, α-NPD was used as the hole transport material and aluminum (Al, from Alfa Aesar, USA) was used as cathode. Prior to the thin film deposition, ITO coated glass substrates (XinYan Technology Ltd., Hong Kong), with a sheet resistance of 15 Ω/□, were ultrasonicated using acetone, isopropyl alcohol, DI water, in that sequence, for 15 min each and dried in flowing nitrogen to ensure that the substrate surface is free of any contaminant. This was followed by UV-Ozone treatment for 15 min which enhances the work-function of ITO.

Thin films of F_4TCNQ, α-NPD and Al were sequentially deposited at a rate of 0.2 $Å s^{-1}$, 0.5 $Å s^{-1}$and 5 $Å s^{-1}$, respectively, by thermal evaporation on the pre-cleaned ITO coated glass substrate under vacuum (base pressure ~ $8x10^{-6}$ mbar). The active area of the device was 1.6 mm^2. Figure 3.1 (a) shows the schematic representation of the fabricated devices with the configuration ITO/F_4TCNQ (x nm)/α-NPD (80 nm)/Al,

where device **D_0**, **D_1**, **D_4** and **D_6** correspond to device with 0 nm, 1 nm, 4 nm and 6 nm thickness of F_4TCNQ, respectively. The energy level diagram of the fabricated devices is shown in Figure 3.1(b). The molecular structures of F_4TCNQ and α-NPD are given in Figure 3.1 (c).

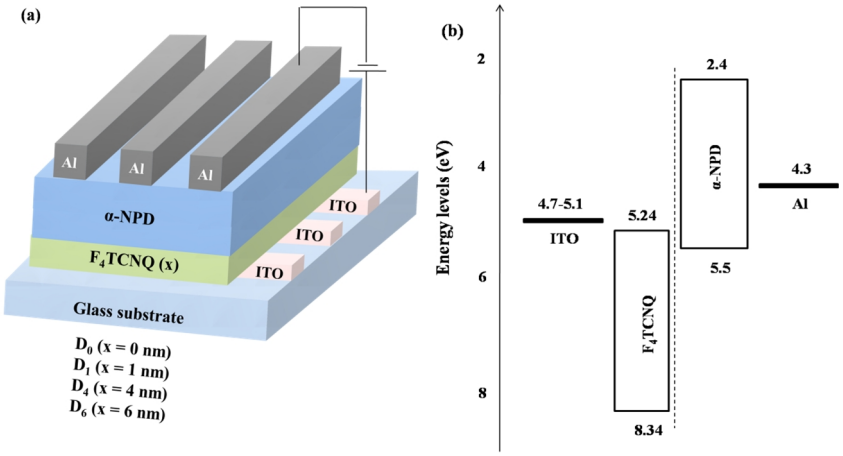

Figure 3.1 (a) Schematic representation of the device structure **D_0**, **D_1**, **D_4** and **D_6** with F_4TCNQ thickness x = 0 nm, 1 nm, 4 nm and 6 nm, respectively and **(b)** energy level diagram

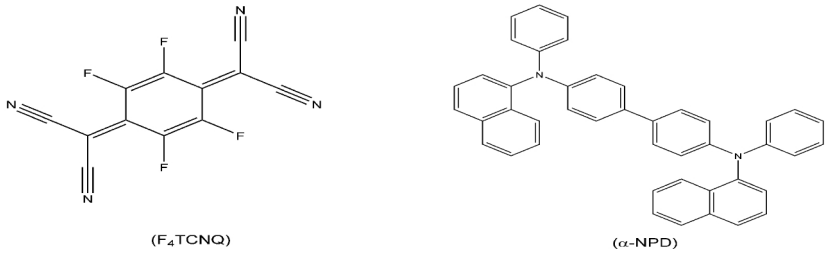

Figure 3.1 (c) Molecular structures of F_4TCNQ and α-NPD

Frequency dependent complex impedance, capacitance and conductance along with voltage dependent capacitance (*C-V*) were measured at room temperature using Agilent E4980A Precision LCR Meter in the frequency range 20 Hz-1 MHz at an *ac* voltage of 100 mV. Current density-voltage (*J-V*) measurements were carried out using computer-controlled Keithley 2400 SMU. All measurements were carried out immediately after device fabrication keeping them in open air.

3.1.3 Results and Discussion

(a) Current Density-Voltage (*J-V*) Characteristics

It is clearly discernible from the current-density versus voltage (*J-V*) characteristics [Figure 3.2 (a)] that insertion of F_4TCNQ and the increase in its layer thickness in the device lead to an enormous increase in current density through the device. Insertion of F_4TCNQ layer between ITO and *α*-NPD leads to two mechanisms. One is reduction in charge injection barrier and the other is moderate doping of α-NPD by F_4TCNQ. These cause the turn-on voltage of the devices to decrease as the F_4TCNQ layer thickness is increased up to 4 nm (**D_4**). However, when the F_4TCNQ layer thickness is increased to 6 nm (**D_6**), there is a slight increase in the turn-on voltage and current density reduces. This suggests that, beyond 4 nm F_4TCNQ layer, higher dopant concentration compromises the structural quality of the layer due to the additional F_4TCNQ molecules remaining un-ionized (Salzmann et al. 2016). This results in increase in the density of traps and scattering centers for free charge carriers, which is clearly detrimental to the conductivity and mobility of the device (Harada et al. 2010, Salzmann et al. 2016). Thus, effectively the injection barrier is increased in device **D_6**.

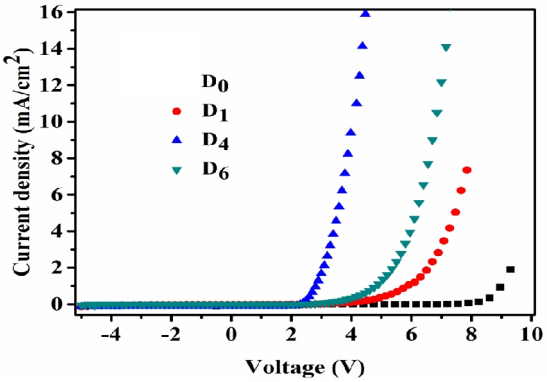

Figure 3.2 (a) *J-V* characteristics of devices **D_0**, **D_1**, **D_4** and **D_6**

Figure 3.2 (b) shows the log *J*- log *V* plot of devices **D_0**, **D_1**, **D_4** and **D_6**. In this figure, it is observed that the current density is space charge limited (SCLC) (region with slope ≈ 2) at high voltages. The turn on voltage of devices **D_0**, **D_1**, **D_4** and **D_6** at which they enter SCLC regime is 7.29 V, 4.91 V, 3.82 V and 4.15 V, respectively. The

reverse leakage current density obtained from the semi-log plot of the devices shown in Figure 3.2 (c) is found to be 6.85 x 10^{-4} mA cm^{-2}, 1.7 x 10^{-2} mA cm^{-2}, 11.8 x 10^{-2} mA cm^{-2} and 1.9 x 10^{-2} mA cm^{-2} at -4 V for device **D_0**, **D_1**, **D_4** and **D_6**, respectively.

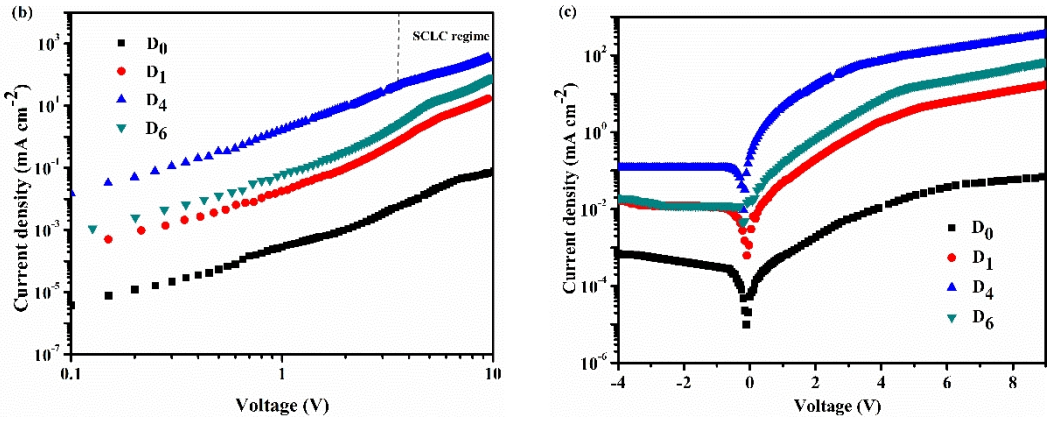

Figure 3.2 (b) log *J*- log *V* plot and **(c)** Semi-log plot of devices **D_0**, **D_1**, **D_4** and **D_6**

Thus, it is clear that the hole injection is efficient in device **D_4**, which may be ascribed to the space charge formed by ionized F_4TCNQ molecules near the interface with α-NPD.

(b) Capacitance-Voltage (*C-V*) Characteristics

The *J-V* characteristics established the need for a layer of F_4TCNQ of optimum thickness in any OLED device. In order to understand the injection properties of F_4TCNQ further, measurement of the capacitance variation of the devices with dc bias voltage on which a small low frequency (500 Hz) *ac* voltage is superimposed [Figure 3.3 (a)] was performed. At reverse bias voltages, the capacitance represents the geometric capacitance of the device, which can be obtained from the following expression (Tripathi and Mohapatra 2014).

$$C_{geo} = \frac{\varepsilon_0 \varepsilon_r A}{d} \tag{3.1}$$

where ε_0 is the permittivity of free space, ε_r is the dielectric constant (~ 3 for organic materials) and A is the area of the device with layer thickness d. At forward bias voltages, *C-V* peaks have been observed at 2.45 V, 4.6 V, 3.45 V and 3.98 V,

respectively, for devices **D0**, **D1**, **D4** and **D6**.

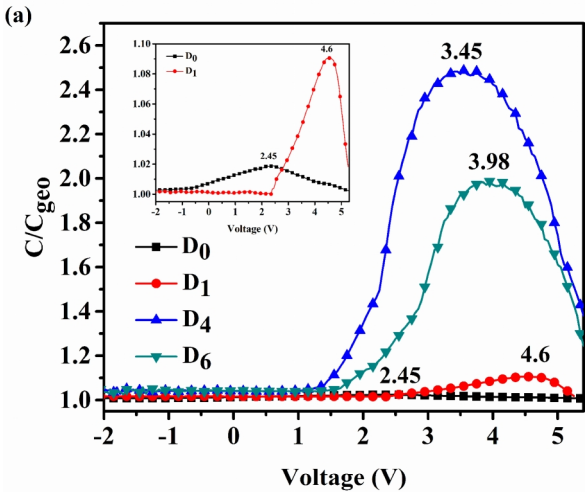

Figure 3.3 (a) *C-V* characteristics of devices **D0**, **D1**, **D4** and **D6** at 500Hz

In general, *C-V* peak occurs close to the built-in voltage (V_{bi}) for intrinsic organic semiconductors (Sharma et al. 2011). Recent investigations by Sharma et al. (2011 and 2013), as well as by Tripathi and Mohapatra (2013), clearly explain the second *C-V* peak, occurring at a voltage slightly above V_{bi}. For the device **D0**, the capacitance peak in the *C-V* plot should ideally occur at the built-in voltage (V_{bi}) i.e., at the difference between the work function of ITO and Al (~ 0.6 V) (Sharma et al. 2011, Tripathi and Mohapatra 2013). In our experiments, the capacitance peak generally occurring near the built-in voltage is absent. Instead, a peak at 2.45 V is seen in device **D0**, which may be due to a large injection barrier (Tripathi and Mohapatra 2014). The characteristic *C-V* peak of device **D1** is observed at a higher voltage when compared to the device **D0**. Introduction of a very thin layer (1 nm) of F_4TCNQ leads to the creation of ionized molecules at the F_4TCNQ/α-NPD interface. This enhances the charge accumulation, resulting in the large peak at 4.6 V in comparison with device **D0**. In addition, the thin layer of F_4TCNQ offers a large interfacial area that may lead to increase in the trap density and, hence, to the peak at 4.6 V. On the other hand, as the thickness of F_4TCNQ increases (4 nm), the effective interfacial area would be less compared to that of the device **D1** and the peak shifts to 3.45 V. However, for device **D6**, the peak is observed at 3.98 V. The shifting of capacitance peak to lower voltages with the decrease in barrier for charge injection at the hetero-interface has been

demonstrated by Tripathi and Mohapatra (2014). This concept can be used to explain the fact that, since the barrier for charge injection increases in **D_6**, the capacitance shifts from 3.45 V in **D_4** to 3.98 V in **D_6**.

For any particular applied bias voltage (say 4 V), the conductance of device **D_4** depends on the thickness of F_4TCNQ layer as is clearly observed from Figure 3.3 (b).

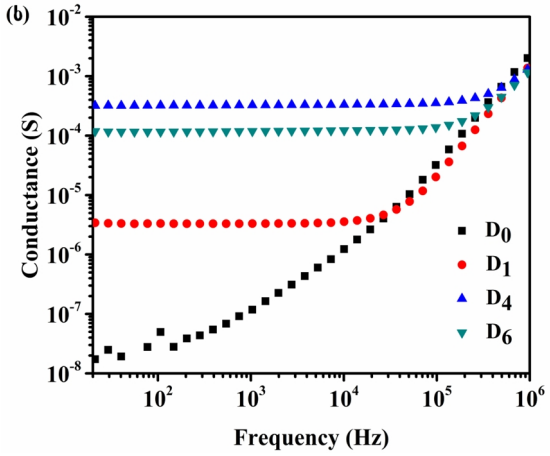

Figure 3.3 (b) Frequency dependent conductance of devices **D_0**, **D_1**, **D_4** and **D_6** at 4 V

A drastic increase by four orders of magnitude is observed in the conductance of device **D_4** (from ~10^{-8} S to ~10^{-4} S) at lower frequencies. Likewise, it can be inferred from the increase in peak capacitance in **D_4** [Figure 3.3 (a)] that, with increase in F_4TCNQ thickness there is an increase in the number of ionized F_4TCNQ molecules, leading to moderate doping of α-NPD. The same interpretation holds good for device **D_1** when compared to **D_0**. However, the capacitance [Figure 3.3 (a)] and conductance of device **D_6** [Figure 3.3 (b)] is observed to reduce compared to device **D_4**. As mentioned earlier, this is because, beyond 4 nm F_4TCNQ layer, higher dopant concentration compromises the structural quality of the layer due to the additional F_4TCNQ molecules remaining un-ionized (Salzmann et al. 2016). This results in increase in the density of traps and scattering centers for free charge carriers, which is clearly detrimental to the conductivity and mobility of the device (Harada et al. 2010, Salzmann et al. 2016). Thus, effectively the injection barrier is increased in device **D_6**.

(c) Capacitance-Frequency (*C-f*) and Conductance-Frequency (*G-f*) Characteristics

Figure 3.4 (a) shows the variation of capacitance with frequency of the *ac* component of applied bias for device **D4**.

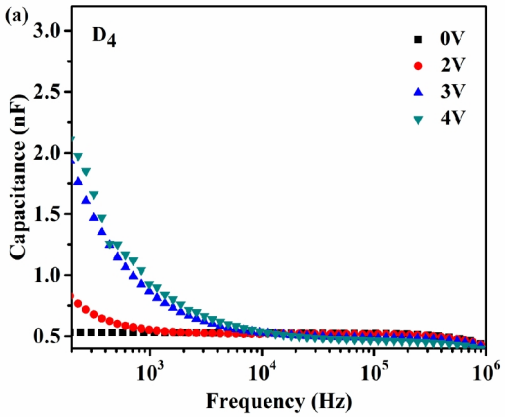

Figure 3.4 (a) Frequency dependent capacitance of device **D4**

At higher frequencies, the capacitance reduces to its geometric value since the dipoles and localized charge carriers will not be able to follow the *ac* electric field variations (Nguyen et al. 2007, Sharma et al. 2013). It is observed that as the applied dc voltage increases, the capacitance in device **D4** increases in magnitude. The threshold frequency at which it drops to the geometric capacitance also increases. The geometric capacitance values are shown in Table 3.1 (b) of the next section. The increase in capacitance is due to increase in the charge injection in device **D4** (Nowy et al. 2010). The threshold frequency shift towards higher region in *C-f* characteristics is due to the increase in the conductance in device **D4** with applied voltage as shown in Figure 3.4 (b). The increase in conductance is also in agreement with the conclusions drawn from the *J-V* characteristics. The nature of *J-V*, *C-V* and *C-f* characteristics, together, clearly indicate an improvement in hole injection in device **D4** in comparison to devices **D0**, **D1** and **D6**.

The loss tangent is given by the following expression (see Agilent Impedance Measurement Handbook-A guide to measurement technology and techniques, 4th edition, page 1-10)

$$\tan\delta = \frac{1}{\omega R_P C_P} \tag{3.2}$$

where δ is called the loss angle measured in radians (equal to $\pi/2 - \phi$), $\omega = 2\pi f$ is the angular frequency of the *ac* signal and $R_P C_P$ is the time constant.

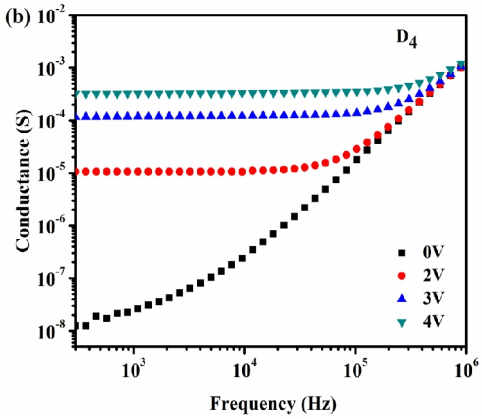

Figure 3.4 (b) Frequency dependent conductance of device **D4**

Figure 3.4 (c) shows the variation of loss tangent with frequency and figure 3.4 (d) shows the comparison of the frequency dependence of loss tangent and imaginary part of dielectric constant (dielectric loss factor ε'') of device **D4**.

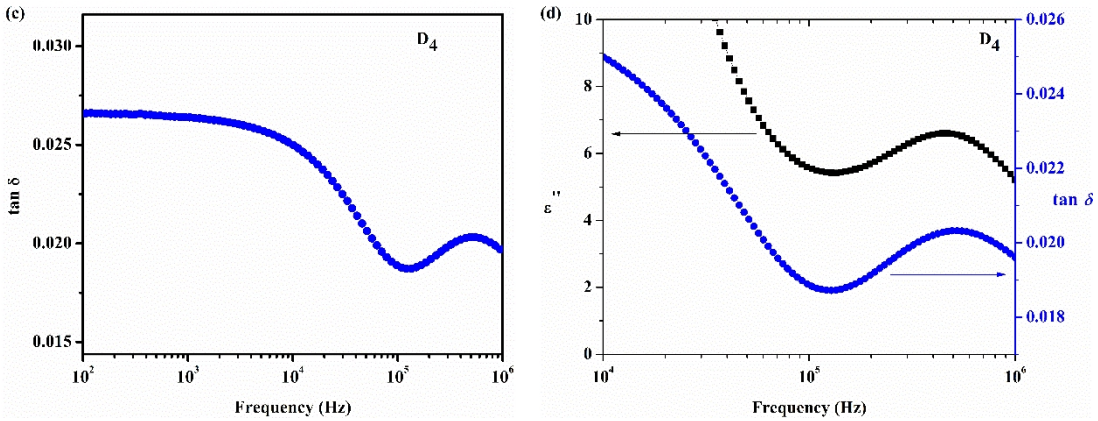

Figure 3.4 (c) Frequency dependent loss tangent of device **D4** at 4 V and **(d)** Comparison of the frequency dependence of loss tangent and imaginary part of dielectric constant of device **D4** at 4 V

From Figure 3.4 (c), it is observed that the loss tangent in device **D4** remains

almost constant (0.026) till 10^4 Hz and then decreases with further increase in frequency. However, at ~ 5 x 10^5 Hz, a small peak is observed in the loss tangent, which corresponds to the peak in the dielectric loss factor ε'' [Figure 3.4 (d)], denoting the relaxation frequency (Lee et al. 2003). Figure 3.4 (e) shows the frequency dependent loss tangent of devices **D0**, **D1**, **D4** and **D6**.

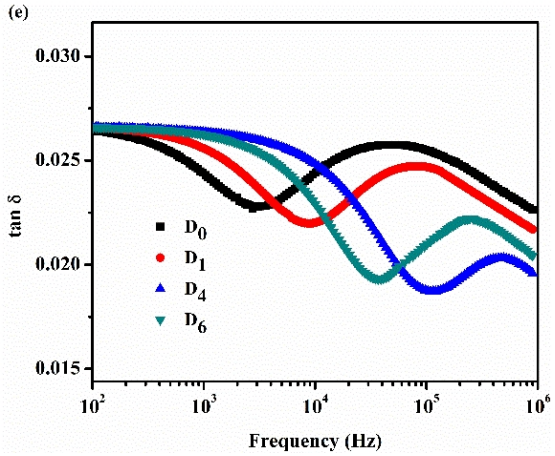

Figure 3.4 (e) Frequency dependent loss tangent of devices **D0**, **D1**, **D4** and **D6** at 4 V

The low values of the loss tangent at high frequency indicate that device **D4** is efficient in terms of charge conduction.

(d) Impedance Measurements

An important technique to investigate electrical characteristics of diode devices is the Complex Impedance measurements. Impedance measurements have been carried out for all the devices fabricated. The complex impedance of the device is given by the equation (Ahn et al. 2005)

$$Z(f) = \mathrm{Re}[Z(f)] + i\,\mathrm{Im}[Z(f)] = R_S + \frac{R_P}{1 + i\omega\tau} \qquad (3.3)$$

Here, R_S is the contact resistance and R_P is the bulk resistance through the organic layer, $\omega = 2\pi f$ is the angular frequency of the *ac* signal and τ, which is equal to $R_P C_P$ (time constant), refers to the relaxation time. The frequency dependent impedance can be represented either as $Z(f)$ or as $Z(\omega)$.

A small *ac* voltage of 100 mV is superimposed on the dc bias voltages for the experiments in the present work. The corresponding impedance studies have been performed at room temperature. As we know, at higher frequencies, the dipoles and localized charge carriers will be unable to follow the *ac* electric field, which implies that there is no dependence on *ac* component of the applied bias voltage. Hence, all the curves in Re[Z(*f*)] and Im[Z(*f*)] versus frequency converge to a single line (i.e., geometric capacitance). As shown in the region II of Figures 3.5 (a) and (b), the characteristic curves for all the voltages converge at higher frequencies for device **D4**.

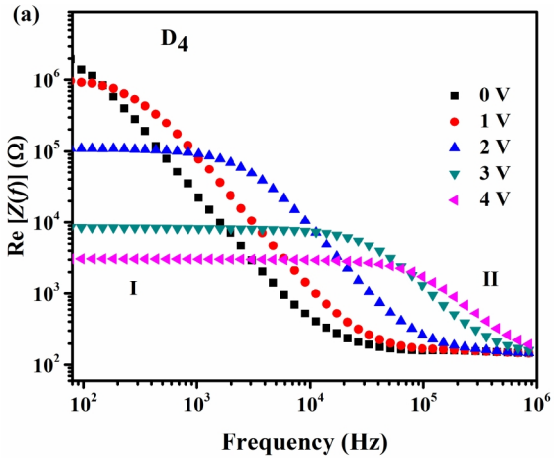

Figure 3.5 (a) Frequency dependent real part of impedance of device **D4**

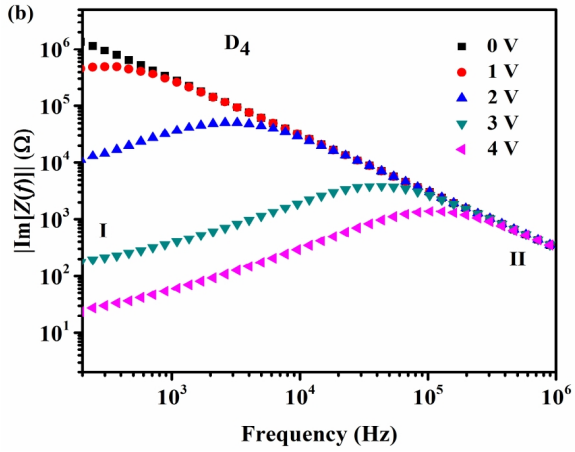

Figure 3.5 (b) Frequency dependent imaginary part of impedance of device **D4**

At low frequencies, the dipoles and localized charge carriers respond to the applied voltage. Good hole injection due to F_4TCNQ layer leads to the increase in conductance through the device. This results in decrease in impedance with applied voltage (0 - 4 V). The peak shift in the Im[$Z(f)$] towards higher frequency region yields the relaxation frequency. This confirms the reduction of relaxation time with increasing dc voltage, which indirectly demonstrates the increase in conductance in the device.

The Cole - Cole plot for Im[$Z(f)$] versus Re[$Z(f)$] of device **D4** for different bias voltages is shown in Figure 3.6 (a). Each curve represents a semicircle of radius $R_P/2$ in a complex plane and the height of the semicircle gives the relaxation frequency. A generalized equivalent circuit model [Figure 3.6 (b)], consisting of a parallel resistor-capacitor RC component (R_P and C_P) with relatively small contact resistance R_S, was used to estimate the parameters from Cole - Cole plots. This is governed by the equation (Ahn et al. 2005)

$$\left(\mathrm{Re}[Z(f)]-\left(R_S+\frac{R_P}{2}\right)\right)^2+\left(|\,\mathrm{Im}[Z(f)]\,|\right)^2=\left(\frac{R_P}{2}\right)^2 \qquad (3.4)$$

Figure 3.6 (c) shows the Cole-Cole plot of devices **D0**, **D1**, **D4** and **D6** at 4 V. As shown in the figure, the fits to the experimental data are obtained using EIS Spectrum Analyzer software, and the values thus obtained for the equivalent circuit components for devices **D0**, **D1**, **D4** and **D6**, at a bias voltage of 4 V are shown in Table 3.1 (a).

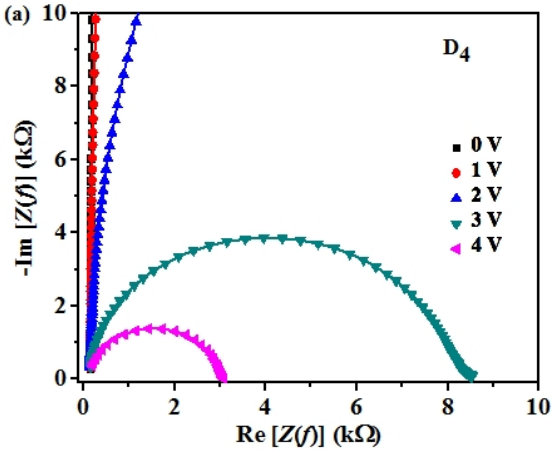

Figure 3.6 (a) Cole-Cole plot at different bias voltages for device **D4**

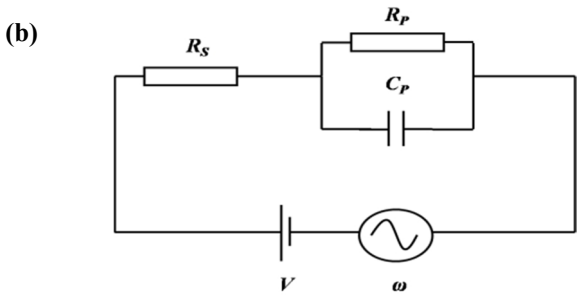

Figure 3.6 (b) Schematic of equivalent circuit model for the analysis of Cole-Cole plot

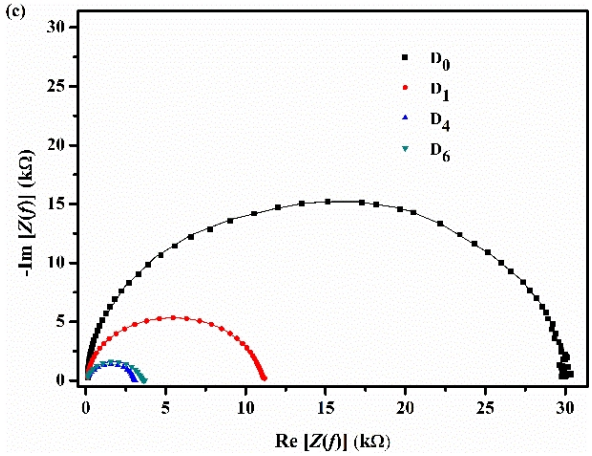

Figure 3.6 (c) Cole-Cole plot of devices **D0**, **D1**, **D4** and **D6** at 4 V

Table 3.1 (a) Equivalent circuit parameters of devices **D0**, **D1**, **D4** and **D6** at 4 V

Device	C_P (nF)	R_P (kΩ)	R_S (Ω)
D0	0.83	31.28	125
D1	0.595	10.80	115
D4	0.520	2.79	150
D6	0.514	3.56	148

It is observed that the parallel capacitance C_P reduces on insertion of F_4TCNQ hole injection layer and is the least in device **D4**. The series or contact resistance (R_S) in all the devices (**D0**, **D1**, **D4** and **D6**) is in the order of few hundreds of ohms when compared to the parallel or bulk resistance (R_P), and is neglected. The reduction of R_P

and C_P in device **D4** when compared to devices **D0**, **D1** and **D6** is attributed to the reduction in the time τ required for the charge carriers to transit through the device. This is due to the increase in conductance through the device **D4**.

The values of geometric capacitance (C_{geo}) estimated from the *C-f* characteristics of all the devices and calculated using equation 3.1 are shown in Table 3.1 (b) and are in the range ~ 0.5 ± 0.1 nF.

Table 3.1 (b) Geometric capacitance of devices **D0**, **D1**, **D4** and **D6**

Device	From *C-f* characteristics (nF)	From equation (nF)
D0	0.61	0.531
D1	0.593	0.524
D4	0.511	0.505
D6	0.498	0.494

The *J-V*, capacitance, conductance and impedance measurements confirm the improved injection of holes in device **D4**.

3.1.4 Conclusion

In summary, the charge transport at the organic interface formed between a hole-injection layer (F_4TCNQ) and a hole transport layer (α-NPD) is explored using capacitance (*C-V* and *C-f*), conductance (*G-f*) and impedance based electrical techniques. The significance of an optimum thickness for the F_4TCNQ layer is clearly established. Such a hole injection layer will greatly improve the efficiency of OLED devices. The thickness of the F_4TCNQ layer plays a crucial role in device properties since the charge carrier storage at the interface depends on the thickness of this layer. In these studies, the device with 4 nm F_4TCNQ proved much more efficient in terms of hole injection compared to the device with no F_4TCNQ and those with 1 nm and 6 nm F_4TCNQ injection layer. An agreement between the results based on capacitance, conductance and impedance measurements has been observed and this work paves the way for the determination of carrier mobility in the devices.

3.2 HOLE TRANSPORT IN α-NPD: THICKNESS DEPENDENT MOBILITY

3.2.1 Introduction

The benefits of novel organic device applications have demanded the study of charge carrier mobility in organic materials (Aloui et al. 2014, Ooi et al. 2014, Fukuda et al. 2014, Philippa et al. 2015). Various studies to determine charge transport properties in organic semiconductors have contributed to the development of more efficient OLED devices. The critical parameters to be optimized include charge injection, transport and recombination (Crone et al. 1998, Blom and Vissenberg 2000, Eva et al. 2010, Pivrikas et al. 2010). Other physical aspects such as defects or traps also affect the performance of these devices (Nguyen et al .2001, Li et al. 2007, Zhan et al. 2007, Kumar et al. 2011). Recently, Sharma et al. (2011) have investigated the dependence of traps in organic semiconductors on the growth conditions and surface morphology. The dopant molecules in the various organic layers in a device function either as traps or scattering centers, thus affecting the charge carrier mobility (Zhan et al. 2007, Chauhan et al. 2010). The generation of free carriers due to the ionization of dopant molecules leads to an increase in the mobility and conductivity (Tong et al. 2007). Lee et al. (2014) demonstrated that direct charge transfer from trap states of host to dopant molecules enhances the conductivity of doped organic semiconductors.

Trapping of charge carriers is considered to be the primary cause for dispersive charge transport in many organic systems (Borsenberger et al. 1992, Berleb and Brütting 2002, Philippa et al. 2014). Here, dispersive charge transport indicates that there is a decrease in the mean hopping rate of the carriers with time due to their trapping in deeper states, and there is broadening of the original carrier packet due to dispersion caused by change in hopping rates (Klauk 2012).

It must be noted that if dispersion is present even at a moderate level, the frequency dependent capacitance and conductance (*C-f* and *G-f*) may not show the characteristic dip needed to determine mobility by negative differential susceptance ($-\Delta B$) and differential conductance ($\omega \Delta G$) methods, respectively (Tripathi et al. 2011). This problem can be overcome by using the frequency dependent impedance method

(|Im[$Z(f)$]|–f) which is not susceptible to dispersion (Tripathi et al. 2011).

In section 3.1 of this thesis, the enhancement in hole injection into α-NPD layer was studied using capacitance and impedance spectroscopy techniques. The measurements were carried out on device **D4** that has a 4 nm thick F_4TCNQ film as hole-injection layer and α-NPD layer of thickness 80 nm. The LUMO of F_4TCNQ (5.24 eV) is very close to the HOMO of α-NPD (5.5 eV). It was shown from the *J-V*, *C-V*, *C-f* and impedance measurements that the device with a 4 nm F_4TCNQ layer has better hole injection properties when compared to the devices without F_4TCNQ and those with 1 nm and 6 nm F_4TCNQ layer (Fernandes et al. 2014). In this context, the present studies focus on the comparative analysis of the charge transport parameter (mobility) of devices without F_4TCNQ (device **D0**) and with 4 nm F_4TCNQ (device **D4**) for varying thickness (100 nm, 500 nm and 1000 nm) of the α-NPD layer.

The charge carrier transport is studied in hole-only devices made using α-NPD with F_4TCNQ film as hole-injection layer. The field dependent mobility of the charge carriers is determined by measuring frequency dependent capacitance, conductance and impedance for varying thickness of α-NPD. The Poole-Frenkel zero-field mobility and the Poole-Frenkel coefficient are evaluated for each device using all the data thus obtained.

3.2.2 Fabrication and Characterization of Hole-only Devices

High quality F_4TCNQ (> 99 %) and α-NPD (> 99.5 %) were obtained from M/s. Lumtec, Taiwan, and were used without any further purification. In this investigation, devices with six different configurations (**D0:100**, **D0:500**, **D0:1000**, **D4:100**, **D4:500** and **D4:1000**) were fabricated in a single batch. Patterned indium tin oxide (ITO, XinYan Technology Ltd., Hong Kong) was used as the bottom anode, F_4TCNQ was used as a hole injection material, α-NPD was used as the hole transport material and aluminum (Al, Alfa Aesar, USA) was used as cathode. Prior to the thin film deposition, ITO coated glass substrates (XinYan Technology Ltd., Hong Kong), with a sheet resistance of 15 Ω/□, were ultrasonicated using acetone, isopropyl alcohol, DI water, in that sequence, for 15 min each and dried in flowing nitrogen to ensure that the substrate

surface is free of any contaminant. This was followed by UV-Ozone treatment for 15 min which enhances the work-function of ITO. Thin films of F_4TCNQ, α-NPD and Al were sequentially deposited at a rate of 0.2 $Å s^{-1}$, 0.5 $Å s^{-1}$ and 5 $Å s^{-1}$, respectively, by thermal evaporation on the pre-cleaned ITO coated glass substrate under vacuum (base pressure ~ $8x10^{-6}$ mbar). The active area of the device was 1.6 mm^2. Figure 3.7 shows the schematic representation of the fabricated devices with the configuration ITO/F_4TCNQ (x nm)/α-NPD (y nm)/Al, i.e., two device sets (F_4TCNQ variation x = 0 and 4 nm) having three device subsets each (α-NPD variation y = 100, 500 and 1000 nm). Devices $\mathbf{D_{0:100}}$, $\mathbf{D_{0:500}}$, $\mathbf{D_{0:1000}}$ correspond to devices with no F_4TCNQ and 100, 500 and 1000 nm α-NPD, respectively, whereas devices $\mathbf{D_{4:100}}$, $\mathbf{D_{4:500}}$ and $\mathbf{D_{4:1000}}$ correspond to devices with 4 nm thickness of F_4TCNQ and 100, 500 and 1000 nm α-NPD, respectively.

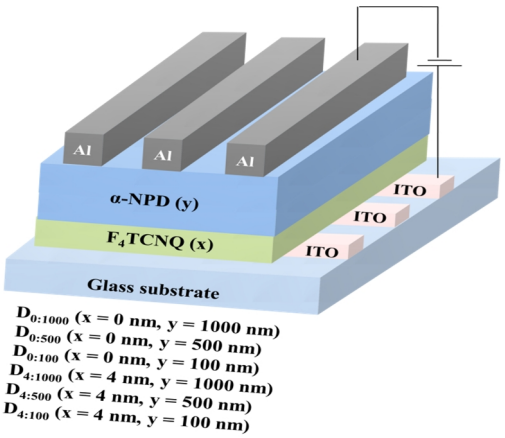

Figure 3.7 Schematic representation of the device structure $\mathbf{D_{0:100}}$, $\mathbf{D_{0:500}}$, $\mathbf{D_{0:1000}}$, $\mathbf{D_{4:100}}$, $\mathbf{D_{4:500}}$ and $\mathbf{D_{4:1000}}$ with F_4TCNQ thickness x = 0 nm and 4 nm and α-NPD thickness y = 100 nm, 500 nm and 1000 nm each, respectively

Frequency dependent complex impedance, capacitance and conductance along with voltage dependent capacitance (*C-V*) were measured at room temperature using Agilent E4980A Precision LCR Meter in the frequency range 20 Hz-1 MHz at an *ac* voltage of 100 mV. Current density-voltage (*J-V*) measurements were carried out using computer-controlled Keithley 2400 SMU. All measurements were carried out immediately after device fabrication keeping them in open air.

3.2.3 Results and Discussion

(a) Current Density-Voltage (*J-V*) Characteristics

Figure 3.8 (a) shows the variation of current density with bias voltage (*J-V* characteristics). It can be observed from the *J-V* characteristics that the set of devices (Set 1) with 4 nm layer of F_4TCNQ have a lower turn-on voltage compared to the set of devices without F_4TCNQ (Set 2). As a control sample, a device with 4 nm F_4TCNQ and 80 nm α-NPD layers was also fabricated. The *J-V*, *C-f*, *G-f* and impedance characteristics of this device agreed well with the results presented above in section 1.

Figure 3.8 (b) shows the log *J*- log *V* plot of devices $\mathbf{D_{0:100}}$, $\mathbf{D_{0:500}}$, $\mathbf{D_{0:1000}}$, $\mathbf{D_{4:100}}$, $\mathbf{D_{4:500}}$ and $\mathbf{D_{4:1000}}$. In this figure, it is observed that the current density is space charge limited (SCLC) (region with slope ≈ 2) at high voltages. The turn on voltage for devices $\mathbf{D_{0:100}}$, $\mathbf{D_{0:500}}$, $\mathbf{D_{0:1000}}$, $\mathbf{D_{4:100}}$, $\mathbf{D_{4:500}}$ and $\mathbf{D_{4:1000}}$ at which they enter SCLC regime is 2.3 V, 2.58 V, 5.13 V, 1.9 V, 2.07 V and 2.21 V, respectively. The reverse leakage current density obtained from the semi-log plot of the devices shown in Figure 3.8 (c) is found to be 3.64 x 10^{-3} mA cm^{-2}, 2.4 x 10^{-4} mA cm^{-2}, 1.58 x10^{-5} mA cm^{-2}, 9.41 x 10^{-2} mA cm^{-2}, 4.8 x 10^{-5} mA cm^{-2} and 1.23 x 10^{-5} mA cm^{-2} at - 4 V for devices $\mathbf{D_{0:100}}$, $\mathbf{D_{0:500}}$, $\mathbf{D_{0:1000}}$, $\mathbf{D_{4:100}}$, $\mathbf{D_{4:500}}$ and $\mathbf{D_{4:1000}}$, respectively. There is a clear indication of improvement in hole injection in the devices having 4 nm thick F_4TCNQ film. The high turn on voltage in case of devices without F_4TCNQ is due to large injection barrier. Moreover, the current density is observed to decrease with increase in α-NPD thickness in devices with and without 4 nm F_4TCNQ. This thickness dependence can be attributed to the dependence of carrier density on voltage in the bulk region, as indicated by equation 3.5 (Tripathi and Mohapatra 2013) given below

$$p(X) = p_0 \exp\left(\frac{-Xq(V_{bi} - V)}{k_B T d}\right) \tag{3.5}$$

where X is the position of organic layer of thickness d from the anode in the device, T is the temperature (in K), p_0 is the carrier density due to accumulation in a narrow region at the injecting contact, q is the electronic charge, k_B is the Boltzmann constant, V is the applied voltage and V_{bi} is the built-in voltage of the device.

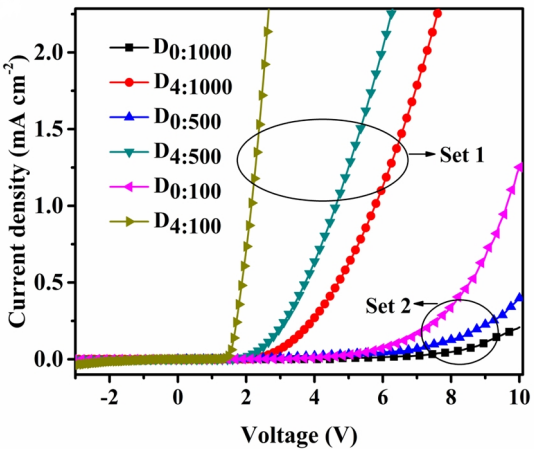

Figure 3.8 (a) *J-V* characteristics of devices **D0:100**, **D0:500**, **D0:1000**, **D4:100**, **D4:500** and **D4:1000** where Set 1 represents devices with 4 nm F_4TCNQ layer and Set 2 represents devices without F_4TCNQ

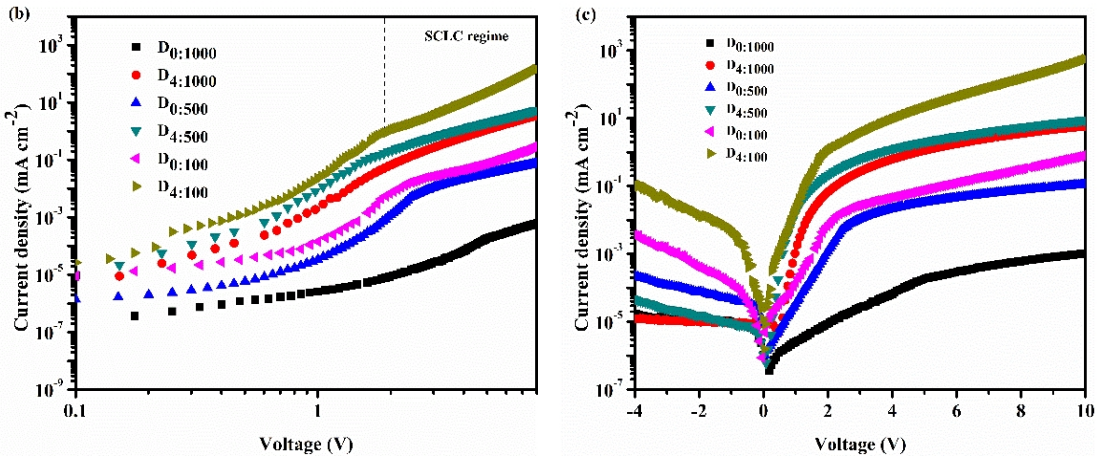

Figure 3.8 (b) log *J*- log *V* plot and **(c)** Semi-log plot of devices **D0:100**, **D0:500**, **D0:1000**, **D4:100**, **D4:500** and **D4:1000**

From equation 3.5, it is established that the accumulation of injected charge carriers is highest at the metal-organic interface ($X = 0$) and decreases as one moves away from the anode. This reduction in the number of charge carriers available for conduction becomes more prominent as the thickness d of α-NPD is increased and is highest when d = 1000 nm. As a result, the current density drops as shown in Figure 3.8 (a).

(b) Negative Differential Susceptance (-Δ*B*)

The frequency dependent variation of capacitance (*C-f*) of devices **D0:100**, **D0:500**, **D0:1000**, **D4:100**, **D4:500** and **D4:1000** was carried out at different voltages (0-10 V) with the superimposed *ac* voltage of 100 mV. The results for only device **D4:1000** are presented here as shown in Figure 3.9 (a). No characteristic dips were observed in the *C-f* plots of the devices having a very thin α-NPD layer (100 nm) and with either no F_4TCNQ layer or with a 4 nm F_4TCNQ layer. This indicates that the interfacial trap states present at the metal-organic interface dominate if the α-NPD layer is relatively thin, whereas devices with thicker α-NPD layer are influenced by bulk properties.

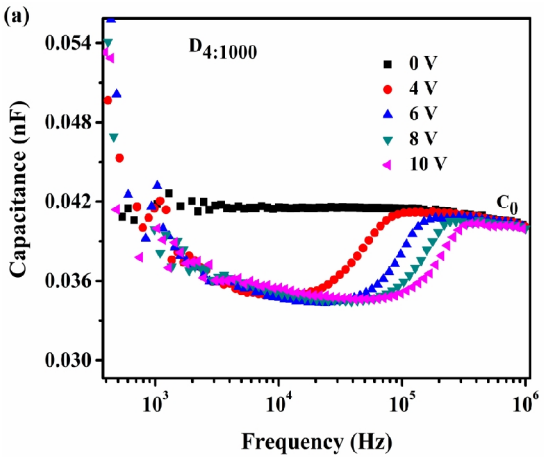

Figure 3.9 (a) Frequency dependent capacitance of device **D4:1000**

As shown in Figure 3.9 (a), the dip in the *C-f* curves is said to be caused by the competition between the transit-time effect and the carrier trapping in the distributed localized state (Ishihara et al. 2014). This minimum value of capacitance is given by $\tau_d = 0.54\tau_r = 0.54/f_{max}$ when using equation 3.6 below (Okachi et al. 2008). For the ideal case of completely trap-free devices, the capacitance at low frequencies reaches ¾ C_0 where C_0 is the geometric capacitance. At higher frequencies, since the dipoles and localized charge carriers do not respond to the applied *ac* bias, the capacitance value goes to C_0. Using the expression for negative differential susceptance $-\Delta B = -\omega(C-C_0)$, the plot of $-\Delta B$ vs f [Figure 3.9 (b)] is generated, from which we get frequency f_{max} (Okachi et al. 2008, Ishihara et al. 2014) at which the peaks occur. Further, the charge

carrier mobility $\mu(F)$ at different voltages can be determined from the following equation (Tsang and So 2006)

$$\mu(F) = \frac{d}{\tau_d F} \tag{3.6}$$

where d is the thickness of the organic layer, $F = V/d$ is the applied electric field at voltage V and $\tau_d = 0.54\tau_r = 0.54/f_{max}$ is the characteristic transit time (Tripathi et al. 2011).

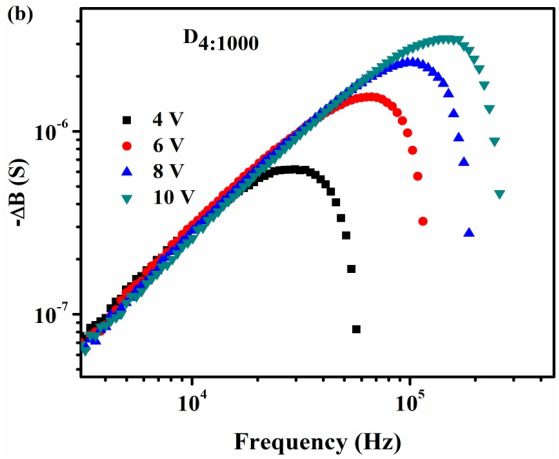

Figure 3.9 (b) Frequency dependent negative differential susceptance $-\Delta B = -\omega(C\text{-}C_0)$ for device **D**$_{4:1000}$ where C_0 is the geometric capacitance

The Poole-Frenkel field dependent carrier mobility (Figure 3.10) is given by (Brütting et al. 2001)

$$\mu(F) = \mu_0 \exp(\beta\sqrt{F}) \tag{3.7}$$

where $F = V/d$ is the applied electric field at voltage V and d is the organic layer thickness. This model describes well the disorder in organic semiconductors. Here, the intercept and slope to the linear fit to the above equation yield the field-independent mobility (μ_0) (also called Zero-field mobility) and the Poole-Frenkel coefficient (β) as shown in Table 3.2 at the end of this section.

From the frequencies (f_{max}) at which the negative differential susceptance ($-\Delta B$)

attains the maximum value in Figure 3.9 (b) and using equation 3.6, the hole-drift mobility values of α-NPD in device **$D_{4:1000}$** are determined at different voltages.

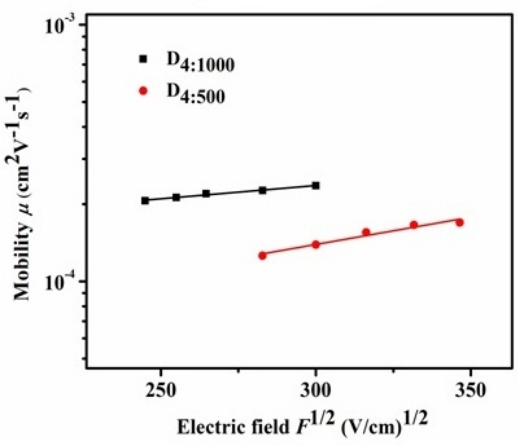

Figure 3.10 Poole-Frenkel dependence of mobility for the devices **$D_{4:1000}$** and **$D_{4:500}$** using *–ΔB* technique (Tsang and So 2006)

In the voltage range 4-10 V, the mobility varies from 1.375 x 10^{-4} $cm^2V^{-1}s^{-1}$ (at 4 V) to 2.787 x 10^{-4} $cm^2V^{-1}s^{-1}$ (at 10 V). The Zero-field mobility in device **$D_{4:1000}$** obtained using Figure 3.10 and equation 3.7 is 1.14 x 10^{-4} $cm^2V^{-1}s^{-1}$.

(c) Differential Conductance ($\omega\Delta G$)

Similar to *–ΔB* technique, the frequency dependent variation of conductance (*G-f*) for devices **$D_{0:100}$**, **$D_{0:500}$**, **$D_{0:1000}$**, **$D_{4:100}$**, **$D_{4:500}$** and **$D_{4:1000}$** was measured at different dc bias voltages (0-10 V) with an *ac* voltage of 100mV superimposed on the dc. The results for device **$D_{4:1000}$** is presented in Figure 3.11 (a). As in the previous case, no characteristic dips were observed in *G-f* plots of the devices irrespective of whether the F_4TCNQ layer was present or not; the devices had a very thin α-NPD layer (100 nm).

The small dips in *G-f* characteristics as seen in Figure 3.11 (a) may be caused by the competition between the transit-time effect and conductance increase due to series resistance (Ishihara et al. 2014). In the ideal case of trap-free devices, the conductance tends to $G(\omega \rightarrow 0) = G_0$ in the low frequency region, whereas it tends to

$G(\omega \rightarrow \infty) = G_\infty = 2/3G_0$ in the higher frequency region (Ishihara et al. 2014). The minimum value of conductance is obtained using equation 3.6 for $\tau_d = 0.36\tau_r = 0.36/f_{max}$ (Ishihara et al. 2014).

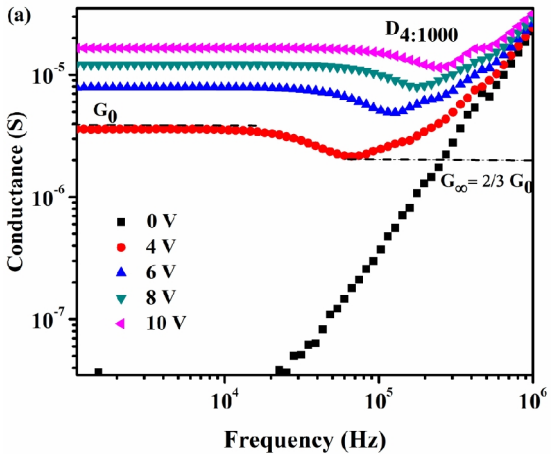

Figure 3.11 (a) Frequency dependent conductance of device **D4:1000**

The value of f_{max} is obtained from the plot of differential conductance $\omega\Delta G = \omega(G - G_\infty)$ versus frequency [Figure 3.11 (b)] from which the mobility at different voltages can be calculated using equation 3.6 (Okachi et al. 2008, Ishihara et al. 2014).

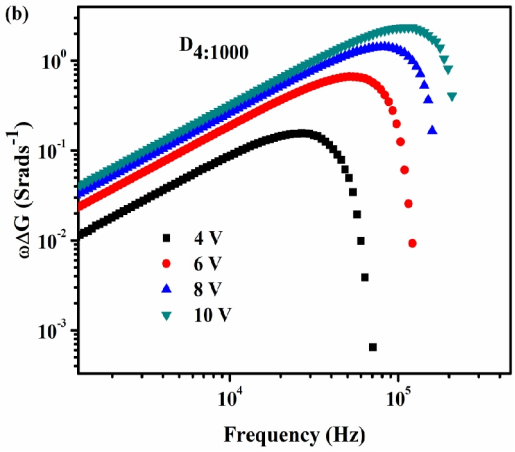

Figure 3.11 (b) Frequency dependent differential conductance $\omega\Delta G = \omega(G - G_\infty)$ of device **D4:1000** where $G(\omega \rightarrow \infty) = G_\infty$ is assumed to be the minimum value of G

From the peak frequencies (f_{max}) of differential conductance ($\omega\Delta G$) in Figure 3.11 (b) and equation 3.6, the hole-drift mobility values of α-NPD in device **D4:1000** are determined at different voltages. In the voltage range 4-10 V, the mobility varies from 1.851 x 10^{-4} $cm^2V^{-1}s^{-1}$ (at 4 V) to 3.022 x 10^{-4} $cm^2V^{-1}s^{-1}$ (at 10 V). The Zero-field mobility in device **D4:1000** obtained using Figure 3.12 and equation 3.7 is 1.38 x 10^{-4} $cm^2V^{-1}s^{-1}$.

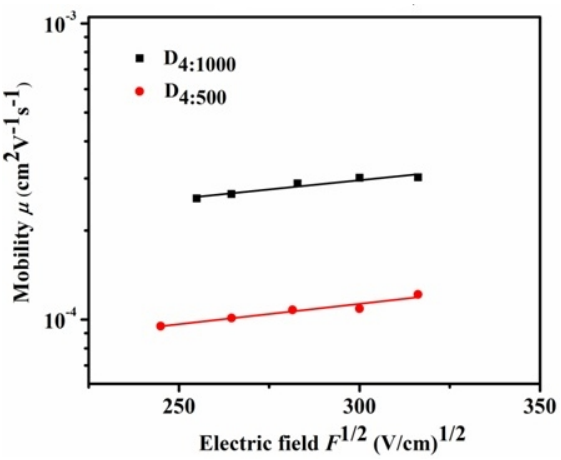

Figure 3.12 Poole-Frenkel dependence of mobility for the devices **D4:1000** and **D4:500** using $\omega\Delta G$ technique

It is observed that the mobility values obtained from $-\Delta B$ and $\omega\Delta G$ methods are in the order of 10^{-4} $cm^2V^{-1}s^{-1}$ in the range 4-10 V.

(d) Frequency Dependent Impedance

The sum of real and imaginary parts of the frequency dependent admittance $Y(\Omega)$ is given by the expression (Martens et al. 2000, Tripathi et al. 2011)

$$Y(\Omega) = G(\Omega) + iB(\Omega) \tag{3.8}$$

where $\Omega = 2\pi f\tau_d = \omega\tau_d$, ω is the angular frequency of the *ac* signal, τ_d is the characteristic transit time, G is the conductance and B is the susceptance.

As mentioned above, the $-\Delta B$ and $\omega\Delta G$ methods are valid for trap-free non-dispersive transport (Okachi et al. 2008, Ishihara et al. 2014). Further, the injection

barrier has to be below the threshold values of 0.2 eV and 0.4 eV, respectively (Okachi et al. 2008, Ishihara et al. 2014). In this context, it should be noted that only the devices **D4:500** and **D4:1000** exhibit the characteristic dip in *C-f* and *G-f* characteristics, from which mobility can be determined. However, the |Im[*Z*(*f*)]| *-f* technique can be employed even in the cases where there is high dispersion and in devices with a small barrier height. So, devices **D0:100**, **D0:500**, **D0:1000**, **D4:100** show frequency dependent change in their impedance characteristics even though no peak is obtained from $-\Delta B$ and $\omega\Delta G$ methods and therefore, mobility can be calculated for these devices too.

The frequency dependent imaginary part of the impedance, as shown in Figure 3.13 (a), gives the relaxation peak ($\tau_r = 1/\omega$) which shows a linear dependence on the characteristic time (τ_d) associated with the carriers. Previous reports have shown that $\tau_d = 0.47\tau_r$ (Tripathi et al. 2011). Hence, the charge carrier mobility can be determined using equation 3.6. The Cole-Cole plot of device **D4:1000** is shown in Figure 3.13 (b). The height of the semicircle represents the relaxation peak ($\tau_r = 1/\omega$) which is the same as that in Figure 3.13 (a).

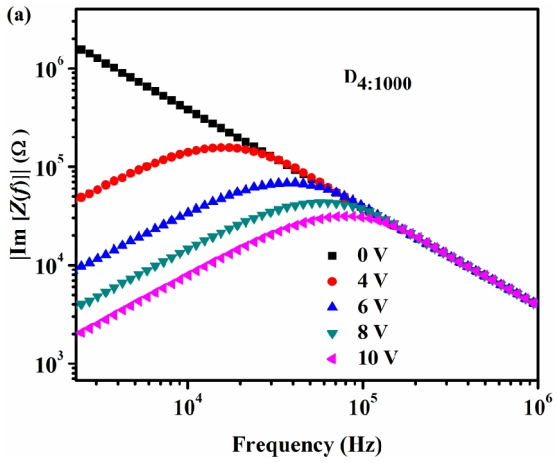

Figure 3.13 (a) Frequency dependent imaginary part of the impedance of device **D4:1000**

From the peak frequencies (f_{max}) of |Im[*Z*(*f*)]| *-f* in Figure 3.13 (a) and equation 3.6, the hole-drift mobility values of α-NPD in device **D4:1000** are determined at different voltages. In the voltage range 4-10 V, the mobility varies from 5.187 x 10^{-4} $cm^2V^{-1}s^{-1}$ (at 4 V) to 1.11 x 10^{-3} $cm^2V^{-1}s^{-1}$ (at 10 V). The Zero-field mobility in device **D4:1000**

obtained using Figure 3.14 and equation 3.7 is 1.82 x $10^{-4}cm^2V^{-1}s^{-1}$.

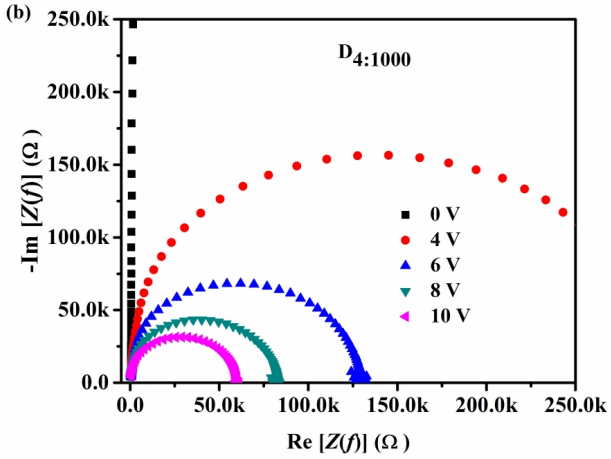

Figure 3.13 (b) Cole-Cole plot at different bias voltages for device **D4:1000**

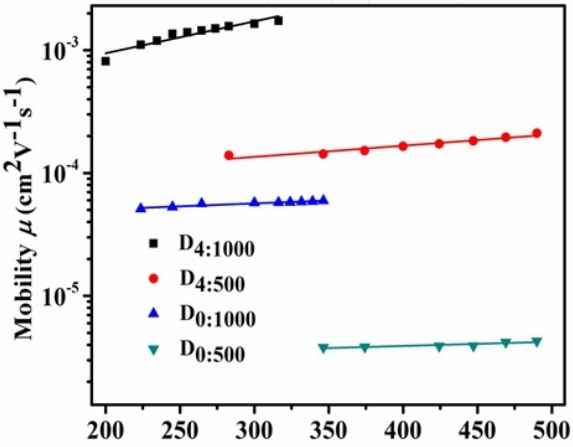

Figure 3.14 Poole-Frenkel dependence of mobility for the devices **D4:1000**, **D4:500**, **D0:1000** and **D0:500** using |Im[*Z*(*f*)]|-*f* technique

Table 3.2 shows the Zero-field mobility of devices **D0:100**, **D0:500**, **D0:1000**, **D4:100**, **D4:500** and **D4:1000** obtained using the techniques: negative differential susceptance (-*ΔB*), differential conductance (*ωΔG*) and frequency dependent imaginary part of impedance (|Im[*Z*(*f*)]|-*f*). It is observed from the table that the values are in the range 10^{-7}–10^{-4} cm^2 V^{-1} s^{-1}. In the voltage range 4-10 V, it is observed that the mobility values obtained from |Im[*Z*(*f*)]| method are higher than those obtained from –*ΔB* and *ω*Δ*G* methods.

Table 3.2 Zero-field mobility of the devices obtained using different techniques

Device	Zero-field Mobility μ_0 ($cm^2V^{-1}s^{-1}$)		
	From $-\Delta B$	From $\omega\Delta G$	From $\lvert Im[Z(f)]\rvert$-f
$D_{0:1000}$	-	-	4.06×10^{-5}
$D_{4:1000}$	1.14×10^{-4}	1.38×10^{-4}	1.82×10^{-4}
$D_{0:500}$	-	-	3.46×10^{-6}
$D_{4:500}$	3.98×10^{-5}	4.30×10^{-5}	4.00×10^{-5}
$D_{4:100}$	-	-	4.89×10^{-7}

This variation is due to the difference in τ_d to τ_r ratio obtained from these methods (Tripathi et al. 2011). However, the Zero-field mobility values obtained from the three methods are in the order of 10^{-4} $cm^2V^{-1}s^{-1}$.

3.2.4 Conclusion

In summary, the mobility in the devices with no F_4TCNQ and 4 nm F_4TCNQ hole-injection layer is investigated by three different measurement schemes and compared in order to corroborate the results of section 3.1. It is established from *J-V* characteristics that all the devices operate in the SCLC regime. The frequency dependent impedance ($|Im[Z(f)]|$-f), capacitance (C-f) and conductance (G-f) characteristics are used to determine the carrier mobility through the devices. The device with 4 nm thick F_4TCNQ layer shows highest mobility for all the measurement methods employed. The Zero-field mobility values obtained from all the methods are in the order of 10^{-4} $cm^2V^{-1}s^{-1}$ in agreement with those reported in literature (Chu and Song 2007, Xu et al. 2014). The Poole-Frenkel coefficient (β) values for all the devices are $\sim 10^{-3} \pm 0.001$ $(cm\ V^{-1})^{1/2}$.

Since the mobility is observed to increase with α-NPD thickness, it can be interesting to know the dependence of mobility beyond the thickness of 1000 nm α-NPD. However, since there is always a trade-off between charge transport and luminescence in OLED devices (Liu et al. 2015), they are usually limited to thicknesses ~ 100 nm (Schols 2011). Therefore, the α-NPD thickness dependent study on the

mobility in this section is restricted to get an overview of the underlying transport mechanism in these devices. This study enables us to better understand the physics of organic materials and devices by investigating their interface and bulk properties.

CHAPTER 4

ELECTRICAL AND OPTICAL PROPERTIES OF NOVEL ALKYL-SUBSTITUTED TRIPHENYLAMINE DERIVATIVES

Abstract

This chapter discusses the electrical and optical properties of three novel compounds bearing triphenylamine (TPA) moiety in hole-only devices through measurement of current density versus voltage (J-V), capacitance versus voltage (C-V), frequency dependent capacitance, ac conductivity, Impedance spectroscopy, UV-Vis and Photoluminescence (PL) spectroscopy. The role of alkyl substitution in these compounds in the improvement of charge transport properties is described in this chapter.

4.1 INTRODUCTION

Molecular engineering, leading to the synthesis of a very wide range of organic materials, together with low temperature technologies for device fabrication have led to rapid progress in this field. Most of the organic materials employed in the electronic devices are π-conjugated materials which have delocalized electrons. It has been observed that organic materials having high Photo Luminescence (PL) efficiency exhibit rather low charge carrier mobility (~ 10^{-6} $cm^2V^{-1}s^{-1}$), whereas materials having large carrier mobility show much lower PL-efficiencies (Liu et al. 2015). Triphenylamine (TPA) and its derivatives, such as α-NPD and TPD, are an important class of π-conjugated organic compounds used in OLED applications. The reported values of hole mobility for such materials fall in the range 10^{-3}-10^{-7} $cm^2V^{-1}s^{-1}$ (So et al. 2007, Fernandes et al. 2015) and the PL quantum efficiencies are seen to be about 30-40% (Liu et al. 2015). A proper choice of the side-group for attachment to such TPA molecules is vital for achieving good device performance. In this chapter, hole-only devices are used to report on the role of methyl and *tert*-butyl groups attached to TPA

molecules on the performance of OLED devices.

The mobility in disordered organic compounds is influenced by several factors such as molecular geometry, impurities and traps. Stability of these compounds in the film form in ambient conditions can significantly affect the charge transport (Kocherzhenko 2011). The stability in ambient conditions depends on the HOMO-LUMO energy levels. Materials with high-lying HOMO levels are prone to oxidation, rendering them less stable (Navamani et al. 2013). However, in TPA molecules, the presence of electron deficient nitrogen and C=N double bond lowers the HOMO energy level, leading to better stability besides enhanced hole-transport (So et al. 2007). Thus, these molecules can be designed to play multifunctional roles in devices depending on their HOMO-LUMO levels which can be suitably altered by molecular engineering.

The presence of side groups in the organic molecules leads to modifications in their electronic and optical properties. One such effect is the increase in the number of π-electrons (Navamani et al. 2013). Secondly, the presence of oxadiazole moiety reduces the steric repulsion and minimizes the torsional disorder between the neighboring units, thereby leading to a more planar structure (Datta and Pati 2004). Nagakubo et al. (2011) observed a reduction in the traps at the organic-substrate interface due to the presence of *tert*-butyl groups, leading to improvement in transistor characteristics (Nagakubo et al. 2011, Higashino et al. 2012). In this chapter, it is shown that the attachment of *tert*-butyl groups to the TPA moiety results in an order of magnitude improvement in the hole mobility ($\sim 10^{-6}$ $cm^2V^{-1}s^{-1}$) and thin films of this material show significant photoluminescence quantum efficiency (~ 30%). This is in contrast to materials having high carrier mobility (Liu et al. 2015) but low PL quantum efficiencies, typically < 1%. Further, the attachment of methyl or *tert*-butyl side group to TPA molecule increases the number of delocalized electrons and also shows higher carrier hopping rate. These investigations suggest that the alkyl-substituted TPA has good potential for OLED applications.

Attachment of *tert*-butyl group to certain organic molecules such as quarterthiophene, TTF and its derivatives, etc., improves their stability and also electronic properties due to the delocalization of π-electrons (Higashino et al. 2012). In

contrast, the attachment of s-alkyl and n-alkyl side groups to these molecules does not bring in these beneficial changes. In addition, the *para*-position of the substituents is responsible for additional electron donation due to a special type of resonance contribution known as hyperconjugation (Pross et al. 1980). It is therefore important to choose appropriate molecules as side groups for achieving the desired optoelectronic characteristics.

This chapter presents the experimental investigation of hole transport in three new compounds containing electron donating TPA moiety. The compounds denoted for further discussion as X_1, X_2 and X_3 are listed below:

X_1:2-(4-(5-(4-(diphenylamino)phenyl)-1,3,4-oxadiazol-2-yl)benzylidene)malononitrile
X_2:2-(4-(5-(4-(di-p-tolylamino)phenyl)-1,3,4-oxadiazol-2-yl)benzylidene)malononitrile
X_3:2-(4-(5-(4-(bis(4-(tert-butyl)phenyl)amino)phenyl)-1,3,4-oxadiazol-2-yl)benzylidene) malononitrile.

In these compounds, X_2 and X_3 are obtained from compound X_1 by attaching methyl and *tert*-butyl substituents, respectively, to the TPA moiety. These compounds were obtained from Indian Institute of Chemical Technology, Hyderabad (India). The photophysical characterization data has been given in the appendices II-IV (page number 112 of this thesis).

The hole mobility is determined by employing Impedance Spectroscopy which is widely used to study organic materials having dispersive transport (Barsoukov and Macdonald 2005). Besides this, current density-voltage (*J-V*), capacitance-voltage (*C-V*) as well as frequency dependent capacitance (*C-f*) and conductivity (σ-*f*) measurements have been carried out on the devices fabricated in order to get an insight into the charge transport process.

Previous theoretical studies (Berlin et al. 2008, Troisi and Cheung 2009, Troisi 2011, Navamani et al. 2013) indicate that the molecular structural dynamics is responsible for interaction between the neighboring localized hopping sites. For hopping transport, electronic coupling and structural relaxation are key parameters

which can be altered by appropriate side-group substitutions. Hence, in this chapter, the role of side-groups on the transport and the frequency dependence of hopping rate has been investigated in detail. The effect of molecular structural oscillations on charge transfer kinetics in these devices has also been analyzed.

4.2 FABRICATION AND CHARACTERIZATION OF HOLE-ONLY DEVICES

The hole-only device structure used in this study is shown in Figure 4.1 (a), which includes 10 nm thick layers of *N,N′*-Di(1-naphthyl)-*N,N′*-diphenyl-(1,1′-biphenyl)-4,4′-diamine (α-NPD) on either side of compounds X_1, X_2 or X_3 to facilitate hole transport from 2,3,5,6-tetrafluoro-7,7,8,8-tetracyanoquinodimethane (F_4TCNQ) layer as well as to block electron injection from the Al cathode. The hole mobility measured in the devices fabricated in this study is in the range 10^{-6} -10^{-7} $cm^2V^{-1}s^{-1}$ and is seen to improve with alkyl substitution. These materials are considered a good choice for maintaining charge carrier balance in organic electronic devices (Leung et al. 2009).

High quality F_4TCNQ (> 99%) and α-NPD (> 99.5%) were obtained from M/s. Lumtec, Taiwan, and were used without any further purification. Three separate devices, viz., **P_1** using compound X_1, **P_2** using X_2 and **P_3** using X_3 were fabricated. Patterned indium tin oxide (ITO) on glass substrate was used as the bottom anode, F_4TCNQ was used as a hole injection material, α-NPD was used as a hole transport and electron blocking material, X_1 or X_2 or X_3 was used as a hole transport material and aluminum [Al, Alfa Aesar (99.999%)] was used as cathode.

The purity of the synthesized compounds was estimated by HPLC and all of them had purity better than 99%. Prior to the thin film deposition, ITO coated glass substrates (XinYan Technology Ltd., Hong Kong), with a sheet resistance of 15 Ω/□, were ultrasonicated using acetone, isopropyl alcohol, DI water, in that sequence, for 15 min each and dried in flowing nitrogen to ensure that the substrate surface is free of any contaminant. This was followed by UV-Ozone treatment for 15 min which enhances the work-function of ITO. All the materials were placed in molybdenum boats, well separated from each other inside the vacuum chamber. Each boat was heated

one at a time. After the deposition of the material from a particular boat, it was covered with a shutter and allowed to cool down. Then the next boat was heated to deposit the succeeding layer and the process was repeated till all the layers were deposited.

Thin films of F_4TCNQ, α-NPD, X_1 or X_2 or X_3 and Al were sequentially deposited at a rate of 0.2 $Å s^{-1}$, 0.5 $Å s^{-1}$, 0.5 $Å s^{-1}$ and 5 $Å s^{-1}$, respectively, by thermal evaporation on the pre-cleaned ITO coated glass substrate under vacuum (base pressure ~ $8x10^{-6}$ mbar). The active area of the device was 1.6 mm^2.

Figure 4.1 (b) shows the HOMO and LUMO energy levels of various layers in the fabricated devices having the following configuration:

ITO/F_4TCNQ (4nm)/α-NPD (10 nm)/X_1 or X_2 or X_3 (125 nm)/α-NPD (10 nm)/Al.

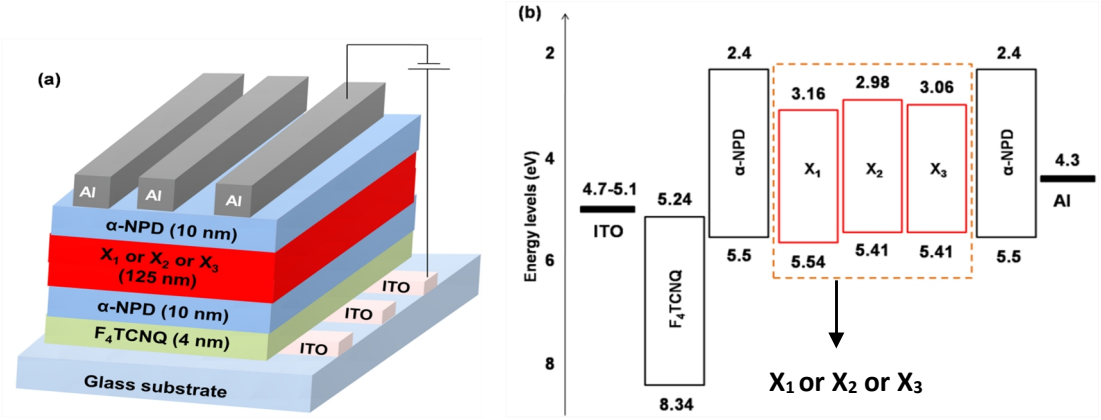

Figure 4.1 (a) Schematic representation of the device structure and **(b)** energy level diagram of various layers, where layers X_1, X_2 and X_3 correspond to devices **P_1**, **P_2** and **P_3**, respectively

As mentioned earlier, in these devices, F_4TCNQ serves as a hole injection layer facilitating injection of holes from ITO into the adjacent hole transporting α-NPD layer. The injection of electrons from Al cathode into the device is blocked by the α-NPD layer adjacent to the cathode.

The molecular structures of F_4TCNQ, α-NPD, X_1, X_2 and X_3 are given in Figure 4.2.

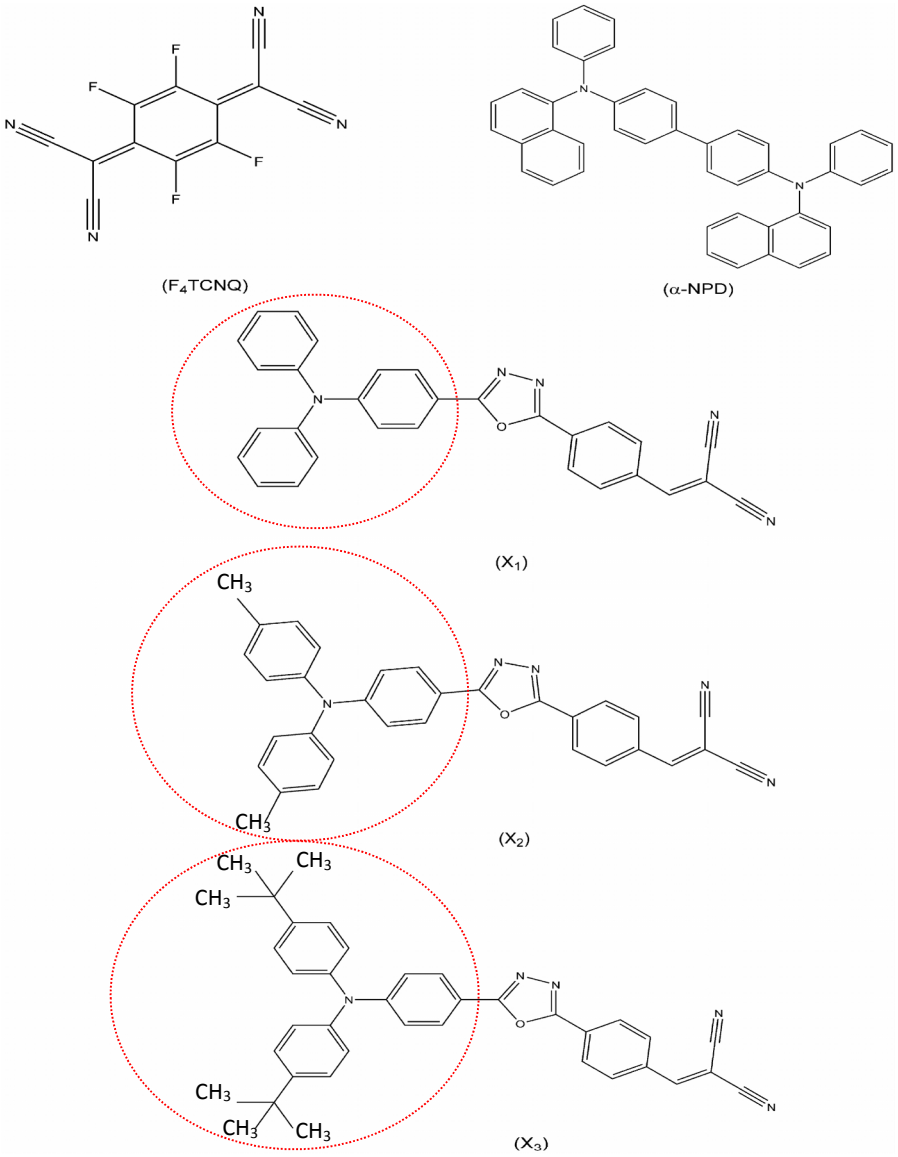

Figure 4.2 Molecular structures of F_4TCNQ, α-NPD, X_1, X_2 and X_3

Methyl and *tert*-butyl functional group substituents in molecules X_2 and X_3 are expected to result in nearly planar molecular structure with highly delocalized π-electron concentration. Since the performance of organic semiconductor devices is strongly sensitive to fabrication conditions, care was taken by fabricating multiple devices, in the 3x3 pixel format, on a given substrate, thereby obtaining 9 identical devices for characterization. The device **P_1** was fabricated using material X_1, device **P_2** using X_2 and **P_3** using X_3 as hole-only device. From the large number of devices of type **P_1**, measurements were carried out for 6 randomly chosen devices. Similar

measurements were done for devices of type **P2** and **P3**. Frequency dependent complex impedance, capacitance and conductivity along with voltage dependent capacitance (*C-V*) were measured at room temperature using Agilent E4980A Precision LCR Meter in the frequency range 20 Hz-1 MHz at an *ac* voltage of 100 mV. Current density-voltage (*J-V*) measurements were carried out using computer-controlled Keithley 2400 SMU. UV-Vis absorption spectra measurements were carried out using Ocean Optics Inc SD2000 spectrometer. All measurements were carried out immediately after device fabrication keeping them in open air.

4.3 RESULTS AND DISCUSSION

4.3.1 Impedance Spectroscopy

Frequency dependent impedance measurements were performed to investigate the conduction mechanism in all the devices. The charge transport in organic materials is dictated by several factors, such as the quality of each of the interfaces, uniformity of the films deposited, quality of the deposited electrode films, the injected free carriers and also the polarizability of the organic molecules. In order to investigate the influence of these factors on the device operation, it is common to plot the imaginary part of the complex impedance against the real part and is termed as Cole–Cole plot. These plots, for our devices **P1**, **P2** and **P3** at different dc bias voltages, are shown in Figure 4.3 (a-c). The shape of the Cole-Cole plots is seen to be non-semi-circular. They may be fitted to a pair of semicircles, which individually represent the behavior of bulk and the interfaces. One may thereby extract relaxation times, corresponding respectively to the bulk and the interfaces, from each of the two semicircles (Liu et al. 2004).

The devices fabricated in this chapter are expected to behave as imperfect capacitors, owing to roughness in the interfaces and metal electrode surfaces, inhomogeneities in the film, varying film thickness and non-uniform current density distribution. For the purpose of electrochemical impedance analysis, such a device is often modeled as the circuit shown in Figure 4.4 (a). In this figure, the resistance R_S corresponds to the contact resistance, R_B and R_I correspond to the bulk and interfacial resistances, respectively.

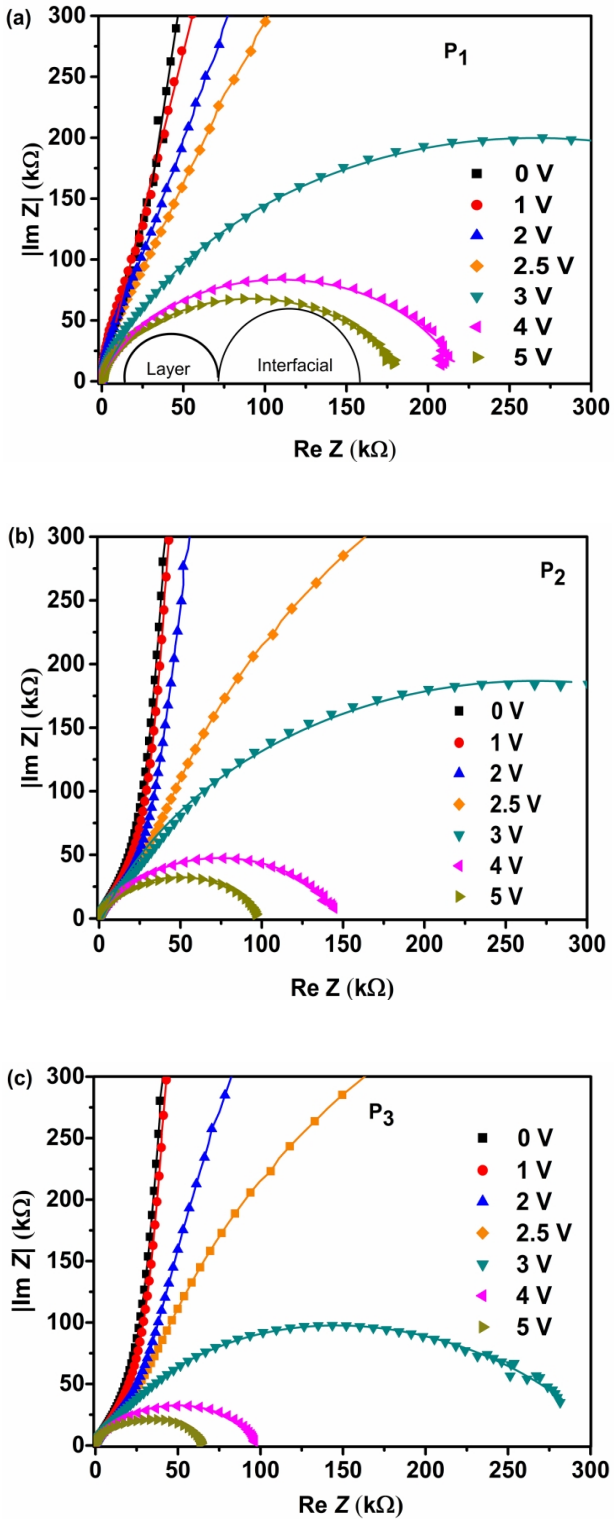

Figure 4.3 Cole-Cole plots at different bias voltages for devices **(a) P_1 (b) P_2** and **(c) P_3**

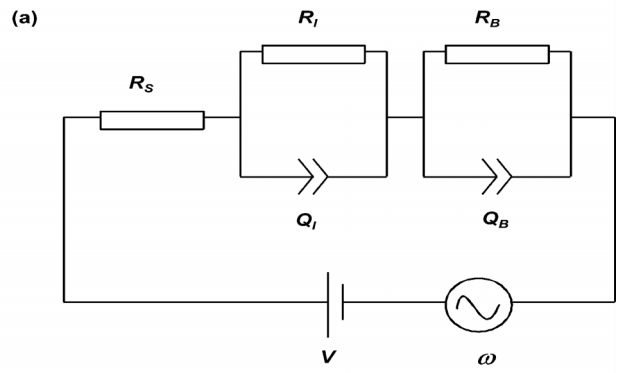

Figure 4.4 (a) Schematic of equivalent circuit model for the analysis of Cole-Cole plot

The elements Q_I and Q_B termed as 'constant phase elements (CPE)' represent the effect of inhomogeneities and surface roughness of various layers in the devices mentioned above.

The frequency dependent complex impedance of this equivalent circuit is given by (Diard et al. 2013)

$$Z(\omega) = R_S + \frac{R_I}{1+(i\omega)^{n_I}\tau_I} + \frac{R_B}{1+(i\omega)^{n_B}\tau_B} \tag{4.1}$$

where $\tau_I = R_I Q_I$ and $\tau_B = R_B Q_B$, with τ_I and τ_B being the average relaxation times at interface and within the organic layers. The curves fitted using equation 4.1 yield values of various circuit parameters for devices **P1**, **P2** and **P3** and are shown in Table 4.1 (a).

Table 4.1 (a) Equivalent Circuit parameters for devices **P1**, **P2** and **P3** at 5 V

Device	R_I **(Ω)**	R_B **(Ω)**	Q_I **(F.cm^{-2}.s$^{(n-1)}$)**	Q_B **(F.cm^{-2}.s$^{(n-1)}$)**	n_I	n_B
P1	1.86×10^{5}	24.3×10^{3}	1.44×10^{-8}	8.98×10^{-9}	0.95	0.76
P2	0.94×10^{5}	16.5×10^{3}	2.72×10^{-8}	9.30×10^{-9}	0.91	0.82
P3	0.59×10^{5}	16.1×10^{3}	4.13×10^{-8}	9.83×10^{-9}	0.98	0.81

From the table, it can be seen that the device **P3** possesses lower interfacial and bulk resistance values (R_I and R_B) compared to the corresponding values for devices **P1** and **P2**. Therefore, the current density in **P3** for a given bias voltage is higher than in **P1** and **P2**. This is also validated by the *J-V* measurements discussed later. With this in mind, a detailed investigation of device **P3** only is carried out, which is presented in Table 4.1 (b). From Table 4.1 (b), it can be seen that the values of n_I and n_B obtained for the device **P3** lie in the range of 0.72–0.98 for different voltages. Further, the value of the series resistance (R_S) is found to be ~ 240 Ω which is much smaller than the values of parallel resistances (R_B and R_I). Values of Q_I and Q_B are seen to remain almost constant with applied voltage, indicating space charge limited conduction mechanism (Kim et al. 2005). The reduction in R_B and R_I with applied voltage corresponds to the reduction in the radius of the semicircles in the Cole-Cole plots as applied bias increases from 3 V to 5 V [see Figure 4.3 (c)] which suggests increase in the injection of charge carriers. The computed values of interfacial and bulk relaxation times ($\tau_I = R_I Q_I$ and $\tau_B = R_B Q_B$) decrease with voltage as shown in Figure 4.4 (b).

Table 4.1 (b) Equivalent circuit parameters for device **P3** at various voltages

Bias (V)	R_I **(Ω)**	R_B **(Ω)**	Q_I **(F.cm^{-2}.s$^{(n-1)}$)**	Q_B **(F.cm^{-2}.s$^{(n-1)}$)**	n_I	n_B
3	2.63×10^{5}	88.4×10^{3}	3.46×10^{-8}	9.79×10^{-9}	0.75	0.72
3.25	1.8×10^{5}	50.1×10^{3}	3.47×10^{-8}	9.61×10^{-9}	0.79	0.75
3.5	1.42×10^{5}	31×10^{3}	3.48×10^{-8}	9.46×10^{-9}	0.82	0.81
3.75	1.25×10^{5}	25.2×10^{3}	3.63×10^{-8}	9.73×10^{-9}	0.87	0.83
4	0.98×10^{5}	23.5×10^{3}	3.96×10^{-8}	9.14×10^{-9}	0.92	0.83
4.25	0.83×10^{5}	22.5×10^{3}	3.97×10^{-8}	9.34×10^{-9}	0.91	0.79
4.5	0.75×10^{5}	21.3×10^{3}	3.98×10^{-8}	9.12×10^{-9}	0.95	0.80
4.75	0.68×10^{5}	18.1×10^{3}	4.01×10^{-8}	9.51×10^{-9}	0.97	0.81
5	0.59×10^{5}	16.1×10^{3}	4.13×10^{-8}	9.83×10^{-9}	0.98	0.81

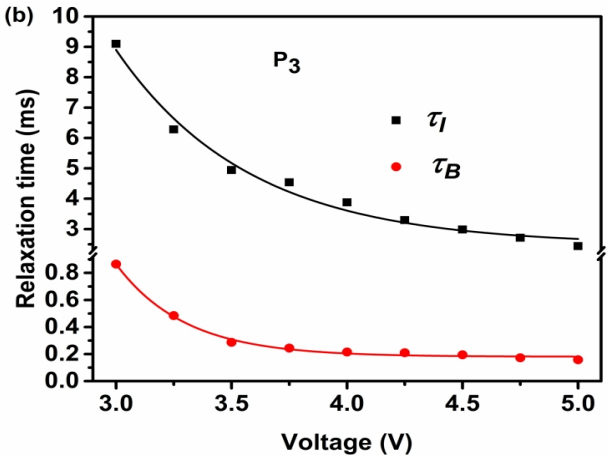

Figure 4.4 (b) Relaxation times at the interface (τ_I) and bulk (τ_B) for device **P3**

It is observed that the relaxation time τ_B in bulk regime is nearly ten times less than τ_I in the interfacial regime in all the devices **P1**, **P2** and **P3**, indicating the dominance of bulk transport in the devices.

4.3.2 Charge carrier mobility from Impedance Spectroscopy

The charge carrier mobility at room temperature was studied by analyzing the frequency dependence of imaginary part of the complex impedance obtained from impedance spectroscopy. Figure 4.5 (a-c) shows the plot of |Im(Z)| as a function of frequency for the devices **P1**, **P2** and **P3** for a range of bias voltages. It can be seen that in each of these plots, |Im(Z)| attains a peak at a particular frequency. The inverse of this frequency gives the bulk relaxation time ($\tau_B = 1/\omega$). The average carrier transit time (τ_{dc}) is related to τ_B through the relation $\tau_{dc} \approx 0.4\tau_B$ (Tripathi et al. 2011).

This transit time at different voltages is used to calculate the mobility as follows (Tsang and So 2006)

$$\mu(F) = \frac{d}{\tau_{dc} F} \tag{4.2}$$

where d is the thickness of the organic layer X_1 or X_2 or X_3 and F is the applied electric field.

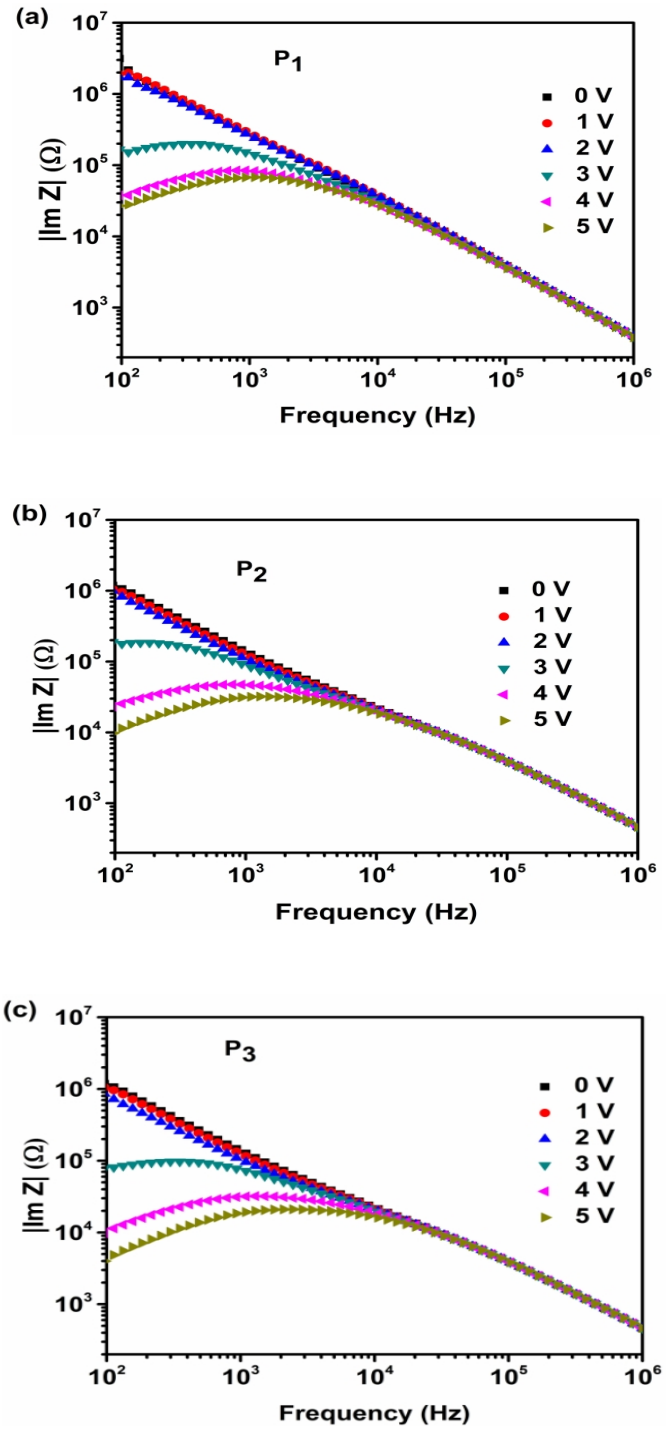

Figure 4.5 Frequency dependent imaginary part of impedance of devices **(a) P_1 (b) P_2** and **(c) P_3**

Theoretically, the mobility is modeled by the well-known Poole-Frenkel theory and is given by (Tsang and So 2006)

$$\mu(F) = \mu_0 \exp(\beta\sqrt{F}) \tag{4.3}$$

where $F = V/d$ is the applied electric field at voltage V and d is the thickness of the layer X_1 or X_2 or X_3. The plot of ln ($\mu(F)$) against $\sqrt{F}$ yields a straight line as shown in Figure 4.5 (d).

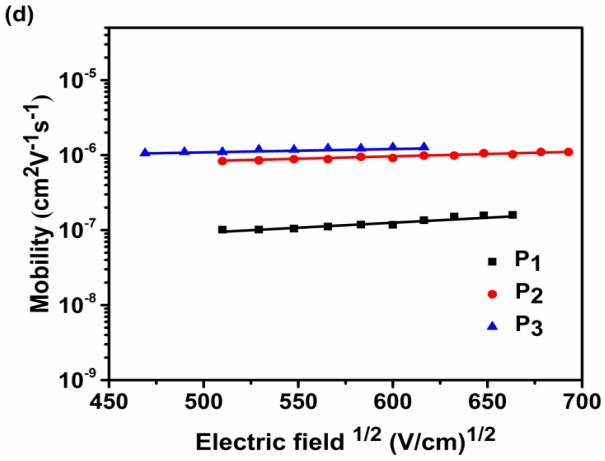

Figure 4.5 (d) Poole-Frenkel dependence of mobility in the devices **P1**, **P2** and **P3**

The slope of this line gives the Poole-Frenkel coefficient (β), and the intercept of the extrapolated graph at $F = 0$ yields the zero-field mobility (μ_0). For devices in this study, the value of β is seen to be in the order of ~ 10^{-3} (cm V^{-1})$^{1/2}$. The values of μ_0 for the devices are shown in Table 4.2.

Table 4.2 Zero-field mobility in devices **P1**, **P2** and **P3**

Device	Zero field mobility ($cm^{-2}V^{-1}s^{-1}$)
P1	1.01 x 10^{-7}
P2	1.06 x 10^{-6}
P3	1.12 x 10^{-6}

An order of magnitude larger hole mobility is observed in devices **P2** and **P3** compared to that in **P1** which may be ascribed to hyperconjugation resulting from the

alkyl substitution on the TPA moiety. Hyperconjugation results in enhanced molecular stability due to the interaction of electrons in the σ-bond with adjacent empty or partially filled p- or π-orbital, leading to extended molecular orbitals. Methyl or *tert*-butyl groups show hyperconjugation and hence, compounds X_2 and X_3 show greater stability and also higher π-electron density compared to X_1. Unlike fluorine, methyl or *tert*-butyl groups do not possess negative inductive effects associated with electron withdrawing nature (Woon et al. 2016). Thus, fluorine substituted compounds are typically less stable and have lower density of delocalized electrons in contrast to molecules with methyl or *tert*-butyl moieties. Further, the extended molecular orbitals ensure greater intermolecular interaction, resulting in higher charge mobility. The experiments in this chapter clearly indicate that attachment of methyl or *tert*-butyl side groups to the TPA molecules leads to an order of magnitude increase in the hole mobility as compared to a pure TPA molecule. This aspect is also corroborated by the enhanced UV-Vis absorption exhibited by devices made using X_2 or X_3 compound [Figure 4.5 (e)].

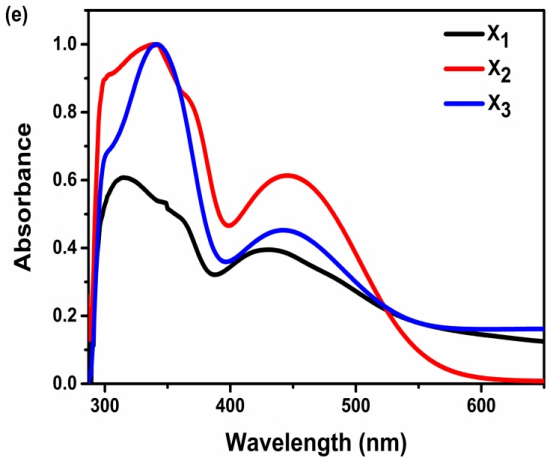

Figure 4.5 (e) UV-Vis spectra of compounds X_1, X_2 and X_3 in thin film

4.3.3 *J-V* Characteristics

The *J-V* characteristics of our devices are shown in Figure 4.6 (a-b). From Figure 4.6 (a), we observe higher current density and lower turn-on voltage for device **P3** compared to devices **P2** and **P1**, indicating improved hole injection and transport, in

agreement with the impedance measurements. This is also consistent with the conclusions from mobility measurements described in section 4.3.2 above. With either of the two substitutions (methyl or *tert*-butyl), there is an increase in the number of delocalized π-electrons. The *para*-position of the substituent leads to highest charge distribution in the aromatic ring at that site (Pross et al. 1980).

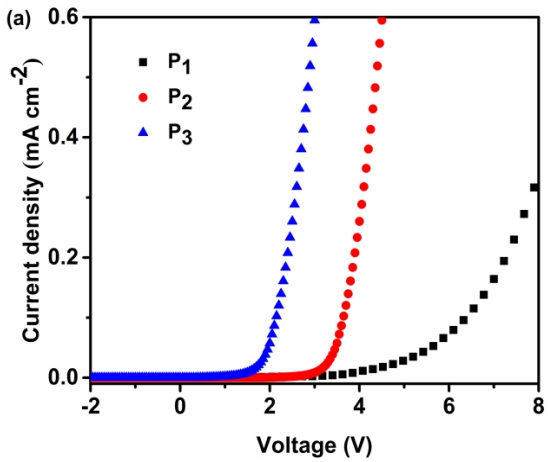

Figure 4.6 (a) *J-V* characteristics of devices **P1**, **P2** and **P3**

Figure 4.6 (b) shows the log *J*- log *V* plot. In this figure, the region with slope ≈ 2 corresponds to space-charge-limited current regime.

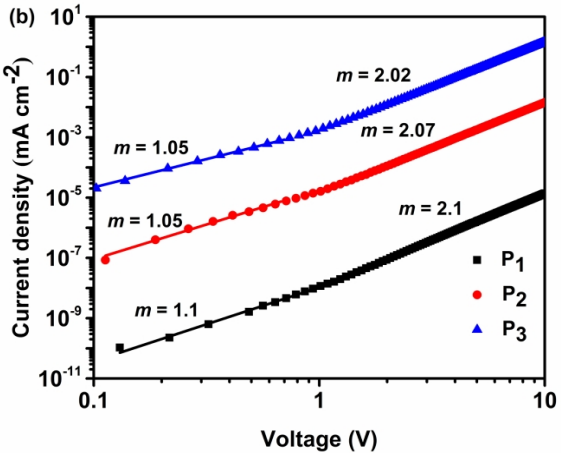

Figure 4.6 (b) log *J*- log *V* plot of devices **P1**, **P2** and **P3**

4.3.4 Charge carrier mobility from *J-V* Characteristics

The current density in the space-charge-limited regime follows the Mott-Gurney law (Lampert and Mark 1970) given below

$$J = \frac{9}{8}\varepsilon_0\varepsilon_r\mu_0\frac{V^2}{d^3} \tag{4.4}$$

where J is the current density, ε_0 is the permittivity of free space, ε_r is the dielectric constant of the organic layer (X_1 or X_2 or X_3) of thickness d, V is the applied voltage and μ_0 is the zero-field charge carrier mobility. Charge carrier mobility values are extracted from the *J-V* characteristics shown in Figure 4.6 (b) for devices **P1**, **P2** and **P3** and are tabulated in Table 4.3.

Table 4.3 Comparison of measured mobility values in devices **P1**, **P2** and **P3**

Device	**Zero field mobility ($cm^{-2}V^{-1}s^{-1}$)**	
	From Impedance Spectroscopy	**From *J-V* Characteristics**
P1	1.01×10^{-7}	0.98×10^{-7}
P2	1.06×10^{-6}	1.02×10^{-6}
P3	1.12×10^{-6}	1.07×10^{-6}

The mobility values obtained from Impedance Spectroscopy and *J-V* characteristics are in good agreement with each other.

4.3.5 *C-V* Characteristics

Figure 4.7 (a) shows capacitance normalized to geometric capacitance (C_g) plotted as a function of dc bias voltage for devices **P1**, **P2** and **P3**. For measurements in this study, the dc bias voltage ranges from –5 V to +5 V and on this bias a 100 mV, 500 Hz *ac* signal is also imposed. This ensures that all the dipoles and localized charge carriers respond to the electric field and contribute to the capacitance.

It is clearly seen that the capacitance equals the geometric capacitance for bias

voltages < - 2V (Sharma et al. 2011). The peak observed at higher voltages in the *C-V* plot can be attributed to the deep traps prevalent at the metal-organic and organic-organic interfaces (Sharma et al. 2011). This peak demarcates the diffusion dominated transport at lower voltages from the drift dominated transport at higher voltages. In general, there is a competition between the two transport mechanisms in the forward bias. At high forward bias, the transport across the entire device is space-charge limited (Tripathi and Mohapatra 2014).

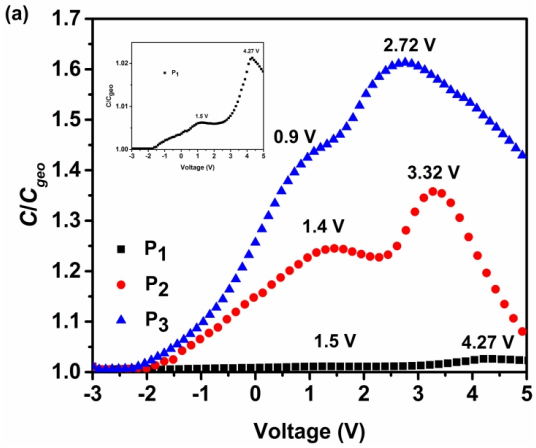

Figure 4.7 (a) *C-V* characteristics of devices **P1**, **P2** and **P3**

Addition of *tert*-butyl group is known to reduce the trap density at the interfaces (Nagakubo et al. 2011), which is in consonance with the shift in the peak towards lower voltage for device **P3** as compared to **P1** and **P2**. Further, a smaller peak is observed at lower voltages, which is proportional to the built-in potential (Sharma et al. 2013). This peak is also seen to reduce progressively from 1.5 to 0.9 V for devices **P1**, **P2** and **P3**, respectively.

4.3.6 *C-f* Characteristics

Since device **P3** exhibits highest current density, again the *C-f* measurements for only **P3** are presented. From the *C-f* characteristics in Figure 4.7 (b), it is seen that the capacitance increases with dc bias voltage at low frequencies due to enhanced charge injection (Nowy et al. 2009, Fernandes et al. 2014).

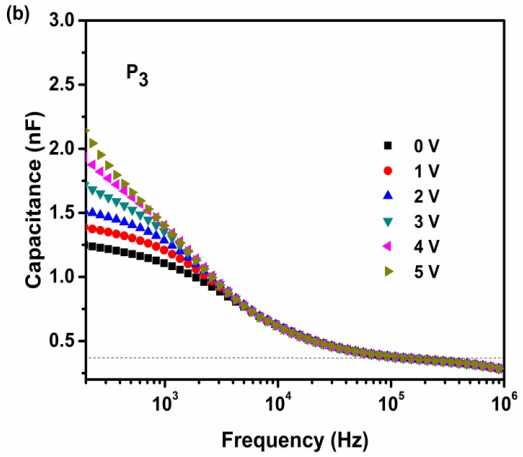

Figure 4.7 (b) Frequency dependent capacitance of device **P3**

At higher frequencies, the dipoles and localized charge carriers cannot follow the rapidly oscillating electric field, leading to reduction in capacitance to its geometric value (C_g) given by the following equation (Nowy et al. 2010)

$$C_g = \frac{\varepsilon_0 \varepsilon_r A}{d} \tag{4.5}$$

where ε_0 is the permittivity of free space, ε_r is the dielectric constant of the organic layer (X_1 or X_2 or X_3) of thickness d and A is the area of the device. The value of this capacitance is seen to be about 0.39 nF from Figure 4.7 (b). The devices **P2** and **P1** also have similar C_g values.

The slight reduction in capacitance below C_g at very high frequencies is ascribed to the parasitic effects due to contact resistances and capacitances (Brütting et al. 2001, Xu et al. 2005).

4.3.7 Conductivity measurements

The nature of field dependent charge transport mechanism in the devices can be ascertained from the frequency dependent conductivity (σ-f) measurements. The *ac* electrical conductivity is given by (Suman et al. 2009)

$$\sigma_{ac} = \frac{d}{A\,\mathrm{Re}[Z(f)]} \tag{4.6}$$

where d is the thickness of the organic layer (X_1 or X_2 or X_3) and A is the area of the device. As shown in Figure 4.8, the *ac* conductivity for device **P3** increases from about 10^{-9} Sm^{-1} to about 10^{-6} Sm^{-1} with voltage at low frequencies and converges to a value in the order of 10^{-5} Sm^{-1} for all voltages at higher frequencies. This clearly shows that at higher frequencies (> 10 kHz) the dipole contribution to σ_{ac} becomes negligible.

The hopping transport in disordered materials is generally described by the Jonscher power law of *ac* conductivity as shown below (Jonscher 1977)

$$\sigma_{ac} = \sigma_{dc} + B\omega^{s};\ 0 < s < 1 \tag{4.7}$$

where σ_{dc} is the dc conductivity, ω is the frequency of the applied *ac* signal, and B is a complex constant depending on the material and doping level. Further, s is determined from the slope of the curves in Figure 4.8. The values of s obtained at 0-5 V for devices **P1**, **P2** and **P3** are seen to range from 0.951 to 0.430 and are displayed in Table 4.4 (a). Various other parameters related to hopping conduction, such as the density of localized states [$N(E_f)$] at the Fermi energy E_f, the energy W_m required by a charge carrier to move from one site to another, and the minimum hopping length R are obtained using the following expressions (Suman et al. 2009)

$$\sigma(\omega) = \frac{\pi^3}{24}\cdot[N(E_f)]^2\cdot\varepsilon_0\varepsilon_r\omega R^6 \tag{4.8}$$

$$R = \frac{e^2}{\pi\varepsilon_0\varepsilon_r}\left[W_m - k_B T\ln\left(\frac{1}{\omega\tau_0}\right)\right]^{-1} \tag{4.9}$$

$$s = 1 - \frac{6k_B T}{W_m - k_B T\ln\left(\frac{1}{\omega\tau_0}\right)} \tag{4.10}$$

where τ_0 is the effective relaxation time, e is the electronic charge, k_B is

Boltzmann's constant and T is the absolute room temperature. The values of these parameters are listed in Table 4.4 (a).

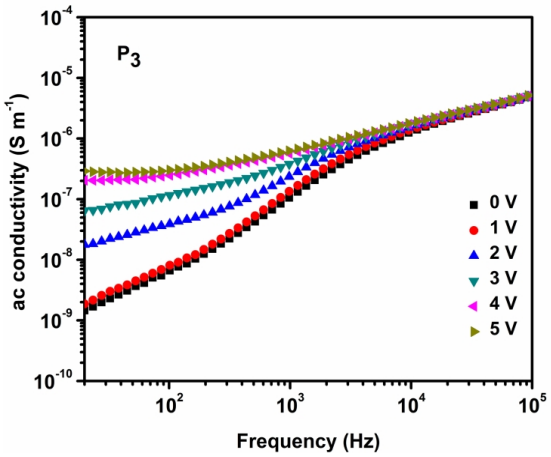

Figure 4.8 Frequency dependent conductivity of device **P3**

It has been shown that for hopping conduction mechanism, the value of s lies between 0 and 1 (Elliott 1977, Hill and Jonscher 1979, Suman et al. 2009, Mansour et al. 2015). Therefore, it can be concluded that, in the devices in this study, the charge transport is dominated by hopping mechanism.

The hopping conductivity, according to density flux model can be written as (Navamani and Senthilkumar 2014, 2015)

$$\sigma(\omega) = \frac{3}{5}\varepsilon_0\varepsilon_r \frac{\partial p}{\partial t} \tag{4.11}$$

where ε_0 is the permittivity of free space, ε_r is the dielectric constant of the organic layer (X_1 or X_2 or X_3) and $\partial p/\partial t$ is the charge transfer rate. In this study, the average charge transfer rate between the two electrodes (ITO and Al) is calculated using equation 4.11.

An important objective of this investigation is to understand the role of alkyl substitution in the organic molecules such as TPA.

Table 4.4 (a) Variation of carrier binding energy, minimum hopping length and density of localized states for device **P_1**, **P_2** and **P_3**

Device	Voltage (V)	s	W_m (eV)	R (nm)	$N(E_f)$ ($eV^{-1}m^{-3}$) at 500 Hz
	0	0.951	3.183	0.57	4.55×10^{28}
	1	0.893	1.457	1.245	4.37×10^{27}
P_1	2	0.775	0.693	2.618	4.70×10^{26}
	3	0.761	0.652	2.782	3.91×10^{26}
	4	0.698	0.516	3.516	1.94×10^{26}
	5	0.613	0.403	4.502	9.25×10^{25}
	0	0.943	2.736	0.644	3.24×10^{28}
	1	0.793	0.753	2.342	6.75×10^{26}
P_2	2	0.722	0.561	3.144	2.79×10^{26}
	3	0.671	0.474	3.722	1.68×10^{26}
	4	0.563	0.356	4.955	7.14×10^{25}
	5	0.551	0.347	5.084	6.61×10^{25}
	0	0.903	1.608	1.039	1.12×10^{28}
	1	0.733	0.584	2.862	5.36×10^{26}
P_3	2	0.652	0.448	3.731	2.42×10^{26}
	3	0.601	0.390	4.286	1.59×10^{26}
	4	0.458	0.287	5.825	6.36×10^{25}
	5	0.430	0.273	6.124	5.48×10^{25}

The alkyl substitution leads to the molecular orbital overlapping between the adjacent molecular units. The size of the substituted alkyl group controls the self-assembling character as well as structural reorganization energy (Prasad 2012, Navamani et al. 2013). To get a clear insight on structure-property relationship, the effect of molecular structural oscillations on the electrical conductivity of the devices has been studied in this chapter. Previous theoretical studies (Berlin et al. 2008, Troisi and Cheung 2009, Troisi 2011, Navamani et al. 2013) confirm that the molecular structural dynamics determines the interaction between electronic and nuclear degrees

of freedom, which is in turn responsible for interaction between the neighboring localized hopping sites. For hopping transport, electronic coupling and structural relaxation are key parameters which can be altered by the molecular structural disorder and appropriate side-group substitutions.

Investigations over the last decade, based on Marcus theory of charge transfer rate have mostly focused on studying the effect of dynamic disorder (due to strong molecular vibrations) on charge transport in organic materials (Berlin et al. 2008, Troisi 2011, Kocherzhenko 2011, Navamani and Senthilkumar 2014, Fornari and Troisi 2014). Thus, in the present study the effect of molecular structural oscillations on charge transfer kinetics for devices **P1**, **P2** and **P3** is analyzed through frequency dependent conductivity (Figure 4.8). The density flux model (Navamani and Senthilkumar 2014, 2015) indicates that the average hopping rate may be directly obtained from the frequency dependent conductivity for hole transport. In our experiments, the *ac* component of the applied bias significantly perturbs the nuclear motion, leading to dynamic disorder (rather than static) in agreement with the previous theoretical studies (Troisi and Cheung 2009, Navamani and Senthilkumar 2015).

To analyze the dynamic disorder effect, the hole hopping rate as a function of frequency [Figure 4.9 (a-c)] is plotted and the curve is fit to the following power law (Berlin et al. 2008, Navamani et al. 2013, Navamani and Senthilkumar 2014)

$$\frac{\partial p}{\partial t} = k(\omega) = \gamma^{1-b} \left(\omega\right)^{b} \tag{4.12}$$

where b is the fitting parameter termed 'dynamic state factor' related to the dynamic disorder. The calculated rate coefficient (γ), hopping conductivity (σ) and dynamic state factor (b) at different applied potentials for the devices **P1**, **P2** and **P3** are displayed in Table 4.4 (b). It is seen that the device **P3** has good hole transporting ability and a hopping rate of 10.73 x10^5 s^{-1} as calculated from the dynamic state factor (~ 0.57 at zero dc bias). This indicates significant influence of molecular oscillations on the charge transport. Of the three devices, **P3** is seen to have the largest hopping conductivity of 19.6 μSm^{-1}, and also maximum dynamic state factor over an applied bias of 0 – 5 V.

For this sample, the dynamic state factor is seen to decrease from 0.574 to 0.531 when the applied voltage is raised from 0 to 5 V [Table 4.4 (b)]. From Figure 4.8, it is noted that the conductivity at a dc bias of 5 V increases by a factor of 10 over a frequency range of 10 Hz – 100 kHz. In contrast, at zero bias voltage, the conductivity increases by about a factor of 1000 over the same frequency range. Therefore, slope of σ-f graph is controlled by the applied potential.

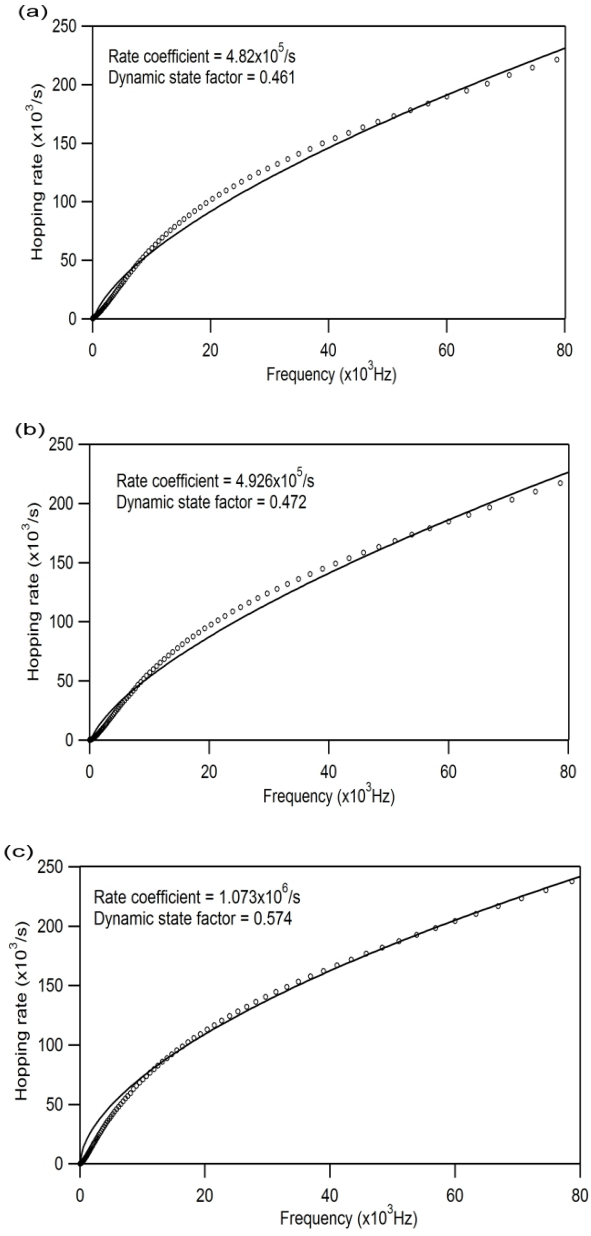

Figure 4.9 The frequency dependent hopping rates for hole transport in **(a) P_1 (b) P_2** and **(c) P_3**

From Table 4.4 (b), it is noted that the dynamic state factor decreases slowly with increase in applied voltage for all the three devices, and hence it can be concluded that the applied potential ensures a uniform rate coefficient. It is also clear from Table 4.4 (b) that the dynamic state factor *b* for any device generally reduces with increase in bias voltage. At smaller *b*, the effect of *ac* component of the bias is expected to be negligible and hence the conductivity is of the dc type. On the other hand, at zero dc bias, *b* is largest, indicating that the conductivity is of the *ac* type.

Table 4.4 (b) Dynamic state factor (*b*) at different applied voltages, rate coefficient (γ) and hopping conductivity (σ) for hole transport in **P1**, **P2** and **P3**

Device	**Dynamic state factor (*b*)**						**Rate coefficient (γ) in $10^5 s^{-1}$**	**Hopping conductivity (σ) in 10^{-6} Sm^{-1}**
	Applied potential (V) in volts							
	V=0	**V=1**	**V=2**	**V=3**	**V=4**	**V=5**		
P1	0.461	0.456	0.429	0.39	0.364	0.33	4.82	8.12
P2	0.472	0.462	0.434	0.4	0.39	0.368	4.93	8.54
P3	0.574	0.566	0.556	0.547	0.542	0.531	10.73	19.61

It is observed from Table 4.4 (a) that devices **P2** and **P3** have lower charge carrier binding energy and density of localized states, and higher minimum hopping length at each applied voltage (0-5 V) when compared to device **P1**. This means that the charge carriers in devices **P2** and **P3** require lesser energy to hop between sites and they are free to move since there are fewer trap states [$N(E_f)$] where the charge carriers are localized [Table 4.4 (a)]. The increase in the minimum hopping length indicates that the injected carriers can hop a greater distance at a given applied bias. However, **P3** has much higher *ac* conductivity, indicating improved carrier transport in accordance with the *J-V*, capacitance and impedance measurements.

4.4 CONCLUSION

In summary, the hole transport properties of three new compounds containing electron donating TPA moiety have been explored using impedance spectroscopy,

current density-voltage (*J-V*) measurements, capacitance-voltage (*C-V*) measurements, frequency dependent capacitance (*C-f*) and frequency dependent *ac* conductivity. The alkyl substitution on the TPA moiety is shown to play an important role in the improvement of hole transport in the devices, mainly due to the increase in π electrons available for conduction on account of hyperconjugation. Various measurements show that, in particular, the presence of *tert*-butyl group in the *para*-position of the TPA moiety leads to superior device properties. The relaxation time associated with the bulk of the organic layer is found to be nearly ten times less than that at the interfaces, indicating dominance of bulk charge transport in all the devices. The value of bulk hole mobility determined in the device is observed to increase by an order of magnitude with alkyl substitution on the TPA moiety in these compounds. Different parameters such as hopping length, carrier binding energy, extended molecular orbitals and the effective localized density of states are determined to understand the charge transport mechanism and relate it to the device performance. The experimental results show that the structural oscillations due to a small applied *ac* electric field improve the charge transport and are in agreement with the previous theoretical studies. The frequency dependence on hopping rate is analyzed by the dynamic state factor which determines the crossover mechanism between *ac* and dc conductivity. The electrical and optical properties of these compounds indicate that they can be potential candidates for applications such as OLEDs.

CHAPTER 5

SUMMARY AND CONCLUSIONS

5.1 SUMMARY AND CONCLUSIONS

In this thesis, hole transport properties of triarylamine-based compounds i.e., α-NPD and novel compounds bearing electron donating TPA moiety have been investigated to understand their electrical characteristics in single carrier device structures fabricated using thermal vapor deposition method. These compounds have some distinct advantages. They have good hole-transporting capability in devices due to the easy oxidizability of the amine nitrogen atom, leading to the ability to transport positive charges efficiently. In addition, they are known to exhibit good chemical, thermal, structural and morphological stability. These properties make them an ideal choice to study the physics involved with these materials in device applications.

5.1.1 Studies on α-NPD with F_4TCNQ as Hole Injection Layer

Hole injection and transport properties of p-type material α-NPD with F_4TCNQ as hole injection layer were investigated using impedance spectroscopy, current density-voltage (*J-V*) measurements, capacitance-voltage (*C-V*) measurements, frequency dependent capacitance and conductance measurements. The thickness of F_4TCNQ and α-NPD layers was varied systematically to study its dependence on these electrical properties in the fabricated hole-only devices. The thickness variation of F_4TCNQ layer was studied in the first section, whereas the second section deals with the thickness variation of α-NPD layer.

In hole-only devices based on α-NPD, it is shown that the thickness of the F_4TCNQ layer plays a crucial role in device properties. The optimum thickness of F_4TCNQ layer is found to be 4 nm and this device shows improvement in hole injection to α-NPD compared to devices with 0, 1 and 6 nm of F_4TCNQ layer. The improvement

in electrical properties is attributed to the charge accumulation leading to injection at the organic interface between F_4TCNQ and α-NPD. The bulk resistance extracted from the equivalent circuit of this device is also shown to be minimum (2.79 kΩ) when compared to the other devices.

The frequency dependent capacitance, conductance and impedance methods yield parameters such as negative differential susceptance ($-\Delta B$), differential conductance ($\omega\Delta G$) and imaginary part of impedance ($|\mathrm{Im}[Z(f)]|$). The field and thickness dependent hole mobility in α-NPD was determined using the frequency dependence of these parameters. In these devices, the thickness of α-NPD was varied and comparative analysis was done with no F_4TCNQ and 4 nm F_4TCNQ layer. The α-NPD thickness dependent hole mobility values determined using $-\Delta B$, $\omega\Delta G$ and $|\mathrm{Im}[Z(f)]|$ methods are in the order of 10^{-4} $cm^2V^{-1}s^{-1}$ for devices with 1000 nm α-NPD and in the order of 10^{-5} $cm^2V^{-1}s^{-1}$ for devices with 500 nm α-NPD. For devices with 100 nm α-NPD, the hole mobility values determined using $|\mathrm{Im}[Z(f)]|$ method are in the order of 10^{-7} $cm^2V^{-1}s^{-1}$. These values obtained from the three methods are in agreement with each other and also with those reported in literature (~ 10^{-6} - 10^{-4} $cm^2V^{-1}s^{-1}$) (Chu and Song 2007, Xu et al. 2014).

5.1.2 Studies on Compounds Bearing Alkyl-Substituted Triphenylamine Moiety

Hole transport characteristics in three new organic compounds based on triphenylamine (TPA) moiety were studied. The effect on electrical and optical properties of TPA, attached with methyl or *tert*-butyl side groups, was investigated through measurement of current density versus voltage (*J-V*), capacitance versus voltage (*C-V*), frequency dependent capacitance, *ac* conductivity, Impedance spectroscopy, UV-Vis spectroscopy and Photoluminescence (PL) spectroscopy. These measurements reveal that, the attachment of methyl or *tert*-butyl group in the *para*-position of the TPA moiety leads to improved electrical and optical properties and greater molecular stability.

The enhanced UV-Vis absorption observed for the alkyl-substituted TPA compounds in thin films indicates greater intermolecular interactions in these

compounds. Moreover, the PL studies indicate significant Quantum Efficiency (~30 %) for alkyl-attached TPA. The nature of transport through the device based on *ac* conductivity measurements is shown to be dominated by hopping process observed in disordered systems. It is also observed that the molecular structural oscillations due to a small applied *ac* electric field improve the charge transfer in these devices. The dynamic state factor *b* has higher value for lower bias voltage, corresponding to dc conductivity; whereas, at higher bias, the value of *b* is smaller, indicating the dominance of *ac* conductivity. Hopping conductivity is seen to be highest for the device with *tert*-butyl substitution in TPA moiety. The experiments indicate an order of magnitude enhancement in charge carrier mobility for alkyl-substituted TPA from ~10^{-7} $cm^2V^{-1}s^{-1}$ to ~10^{-6} $cm^2V^{-1}s^{-1}$. The relaxation time is computed from the equivalent circuit parameters, and its value associated with the bulk of the organic layer is found to be nearly ten times less than that at the interfaces, indicating dominance of bulk charge transport in all the devices.

Clearly, the electrical and optical properties of these triarylamine-based compounds indicate that they can be potential candidates for applications such as OLEDs, and their electrical characteristics in devices help us understand the underlying physics behind their charge transport mechanism. This understanding is essential to develop efficient optoelectronic devices by tuning the device architecture and the molecular structure design with the electrical and optical properties.

5.2 SCOPE FOR FURTHER RESEARCH

The investigations of the present research work can be extended further in the following directions:

- Present measurements were performed at room temperature in ambient conditions. This can be extended to temperature dependent measurements in controlled conditions.
- The electrical measurements carried out in this work can be correlated to the surface morphology of the thin films in the device.

- The charge injection and transport studies presented here were limited to hole-only devices based on triarylamine compounds. This can be extended to studies on electron-only devices using electron transport materials and appropriate electrodes, as well as OLED fabrication and characterization.
- Studies on the compounds used in this work were limited to certain thickness values. The suitability of their electrical characteristics can be examined for devices in a wide range of thicknesses.
- Optimization of material design (using quantum chemical modelling) and synthesis as well as device architecture should be carried out to arrive at best device performances.

APPENDIX I: Agilent E4980A Precision LCR Meter 20 Hz to 2 MHz Data Sheet

Agilent

E4980A Precision LCR Meter
20 Hz to 2 MHz

Data Sheet

Agilent Technologies

Definitions

All specifications apply to the conditions of a 0 to 55 °C temperature range, unless otherwise stated, and 30 minutes after the instrument has been turned on.

Specifications (spec.): Warranted performance. Specifications include guardbands to account for the expected statistical performance distribution, measurement uncertainties, and changes in performance due to environmental conditions.

Supplemental information is provided as information that is useful in operating the instrument, but is not covered by the product warranty. This information is classified as either typical or nominal.

Typical (typ.): Expected performance of an average unit without taking guardbands into account.

Nominal (nom.): A general descriptive term that does not imply a level of performance.

How to Use Tables

When measurement conditions fall under multiple categories in a table, apply the best value.

For example, basic accuracy Ab is 0.10% under the following conditions;

Measurement time mode	SHORT
Test frequency	125 Hz
Test signal voltage	0.3 Vrms

Basic Specifications

Measurement functions

Measurement parameters

- Cp-D, Cp-Q, Cp-G, Cp-Rp
- Cs-D, Cs-Q, Cs-Rs
- Lp-D, Lp-Q, Lp-G, Lp-Rp, Lp-Rdc[1]
- Ls-D, Ls-Q, Ls-Rs, Ls-Rdc[1]
- R-X
- Z-θd, Z-θr
- G-B
- Y-θd, Y-θr
- Vdc-Idc[1]

Definitions

Cp Capacitance value measured with parallel-equivalent circuit model
Cs Capacitance value measured with series-equivalent circuit model
Lp Inductance value measured with parallel-equivalent circuit model
Ls Inductance value measured with series-equivalent circuit model
D Dissipation factor
Q Quality factor (inverse of D)
G Equivalent parallel conductance measured with parallel-equivalent circuit model
Rp Equivalent parallel resistance measured with parallel-equivalent circuit model
Rs Equivalent series resistance measured with series-equivalent circuit model
Rdc Direct-current resistance
R Resistance
X Reactance
Z Impedance
Y Admittance
θd Phase angle of impedance/admittance (degree)
θr Phase angle of impedance/admittance (radian)
B Susceptance
Vdc Direct-current voltage
Idc Direct-current electricity

Deviation measurement function: Deviation from reference value and percentage of deviation from reference value can be output as the result.

Equivalent circuits for measurement: Parallel, Series

Impedance range selection: Auto (auto range mode), manual (hold range mode)

Trigger mode: Internal trigger (INT), manual trigger (MAN), external trigger (EXT), GPIB trigger (BUS)

1. Option E4980A-001 is required.

Table 1. Trigger delay time

Range	0 s - 999 s
Resolution	100 µs (0 s - 100 s) 1 ms (100 s - 999 s)

Table 2. Step delay time

Range	0 s - 999 s
Resolution	100 µs (0 s - 100 s) 1 ms (100 s - 999 s)

Measurement terminal: Four-terminal pair

Test cable length: 0 m, 1 m, 2 m, 4 m

Measurement time modes: Short mode, medium mode, long mode.

Table 3. Averaging

Range	1 - 256 measurements
Resolution	1

Test signal

Table 4. Test frequencies

Test frequencies	20 Hz - 2 MHz
Resolution	0.01 Hz (20 Hz - 99.99 Hz) 0.1 Hz (100 Hz - 999.9 Hz) 1 Hz (1 kHz - 9.999 kHz) 10 Hz (10 kHz - 99.99 kHz) 100 Hz (100 kHz - 999.9 kHz) 1 kHz (1 MHz - 2 MHz)
Measurement accuracy	± 0.01%

Table 5. Test signal modes

Normal	Program selected voltage or current at the measurement terminals when they are opened or short-circuited, respectively.
Constant	Maintains selected voltage or current at the device under test (DUT) independently of changes in impedance of DUT.

Signal level

Table 6. Test signal voltage

Range		0 Vrms - 2.0 Vrms
Resolution		100 µVrms (0 Vrms - 0.2 Vrms) 200 µVrms (0.2 Vrms - 0.5 Vrms) 500 µVrms (0.5 Vrms - 1 Vrms) 1 mVrms (1 Vrms - 2 Vrms)
Accuracy	Normal	±(10% + 1 mVrms) Test frequency ≤ 1 MHz: spec. Test frequency > 1 MHz: typ.
	Constant[1]	±(6% + 1 mVrms) Test frequency ≤ 1 MHz: spec. Test frequency > 1 MHz: typ.

Table 7. Test signal current

Range		0 Arms - 20 mArms
Resolution		1 µArms (0 Arms - 2 mArms) 2 µArms (2 mArms - 5 mArms) 5 µArms (5 mArms - 10 mArms) 10 µArms (10 mArms - 20 mArms)
Accuracy	Normal	±(10% + 10 µArms) Test frequency ≤ 1 MHz: spec. Test frequency > 1 MHz: typ.
	Constant[1]	±(6% + 10 µArms) Test frequency < = 1 MHz: spec. Test frequency > 1 MHz: typ.

Output impedance: 100 Ω (nominal)

Test signal level monitor function

- Test signal voltage and test signal current can be monitored.
- Level monitor accuracy:

Table 8. Test signal voltage monitor accuracy (Vac)

Test signal voltage[2]	Test frequency	Specification
5 mVrms - 2 Vrms	≤ 1 MHz	± (3% of reading value + 0.5 mVrms)
	> 1 MHz	± (6% of reading value + 1 mVrms)

Table 9. Test signal current monitor accuracy (Iac)

Test signal current[2]	Test frequency	Specification
50 µArms - 20 mArms	≤ 1 MHz	± (3% of reading value + 5 µArms)
	> 1 MHz	± (6% of reading value + 10 µArms)

1. When auto level control function is on.
2. This is not an output value but rather a displayed test signal level.

Measurement display ranges

Table 10 shows the range of measured value that can be displayed on the screen.

Table 10. Allowable display ranges for measured values

Parameter	Measurement display range
Cs, Cp	±1.000000 aF to 999.9999 EF
Ls, Lp	± 1.000000 aH to 999.9999 EH
D	± 0.000001 to 9.999999
Q	± 0.01 to 99999.99
R, Rs, Rp, X, Z, Rdc	±1.000000 aΩ to 999.9999 EΩ
G, B, Y	± 1.000000 aS to 999.9999 ES
Vdc	±1.000000 aV to 999.9999 EV
Idc	±1.000000 aA to 999.9999 EA
θr	± 1.000000 arad to 3.141593 rad
θd	± 0.0001 deg to 180.0000 deg
D%	±0.0001 % to 999.9999 %

a: 1×10^{-18}, E: 1×10^{18}

APPENDIX II: UV-Vis Spectra of novel molecules in Solution

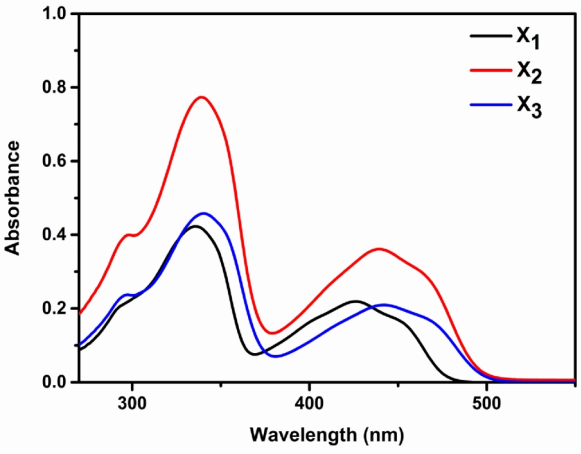

Figure I UV-Vis spectra of compounds X_1, X_2 and X_3 in solution (1×10^{-5} M, hexane)

APPENDIX III: Fluorescence Spectra of novel molecules in Solution

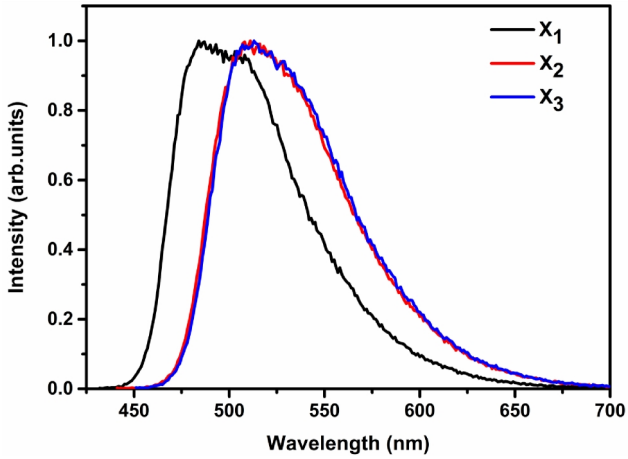

Figure II Fluorescence spectra of compounds X_1, X_2 and X_3 in solution (1×10^{-5} M, hexane)

APPENDIX IV: Fluorescence Spectra of novel molecules in Thin Film

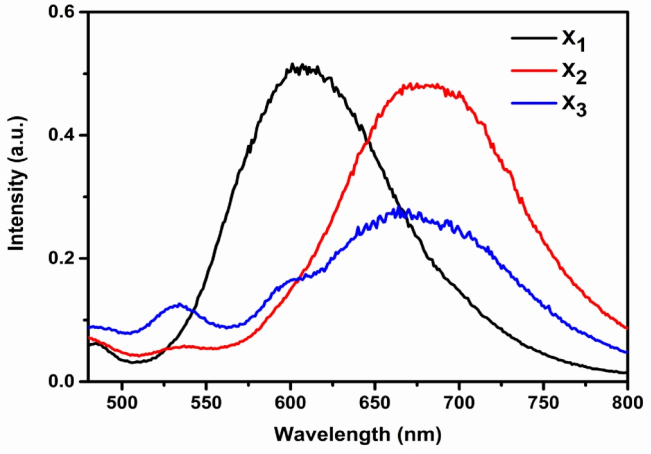

Figure III Fluorescence spectra of compounds X_1, X_2 and X_3 in thin film

Table III Fluorescence quantum yield of compounds X_1, X_2 and X_3

Compound	**Fluorescence quantum yield (measured in hexane)** [a]
X_1	0.20
X_2	0.30
X_3	0.28

[a] relative to 9,10-diphenyl anthracene (quantum yield = 0.95 in cyclohexane).

REFERENCES

Adachi, C., Tokito, S., Tsutsui, T. and Saito, S. (1988). "Organic Electroluminescent Device with a Three-Layer Structure." *Jpn. J. Appl. Phys*., 27 (4A), L713-L715.

Agarwal, R. Agarwal, A. K. and Mazhari, B. (2016). "Estimation of carrier mobility at organic semiconductor/insulator interface using an asymmetric capacitive test structure." *AIP Adv*., 6 (4), 045017-1-045017-5.

Agilent Technologies (2009). *Agilent Impedance Measurement Handbook-A guide to measurement technology and techniques*, © Agilent Technologies, Inc. 2000-2009, USA.

Ahn, J. -H., Chung, D. -H., Lee, J. -U., Lee, G. -S., Song, M. -J., Lee, W. -J., Han, W. -K. and Kim, T. W. (2005). "Equivalent-Circuit Analysis of Organic Light-Emitting Diodes by Using the Frequency-Dependent Response of an ITO/Alq3/Al Device." *J. Korean Phys. Soc*., 46 (2), 546-550.

Aloui, W., Ltaief, A., Bouazizi, A. (2014). "Electrical impedance studies of optimized standard P3HT:PC_{70}BM organic bulk heterojunctions solar cells." *Superlattice. Microst.,* 75, 416–423.

Arkhipov, V. I., Emelianova, E. V., Tak, Y. H. and Bässler, H. (1998). "Charge injection into light-emitting diodes: Theory and experiment." *J. Appl. Phys*., 84 (2), 848-856.

Barsoukov, E. and Macdonald, J. R. (2005). *Impedance Spectroscopy Theory, Experiment, and Applications*, Wiley, USA.

Bässler, H. (1993). "Charge Transport in Disordered Organic Photoconductors." *Phys. Status Solidi B*., 175 (1), 15-56.

Beljonne, D., Cornil, J., Muccioli, L., Zannoni, C., Brédas, J. –L. and Castet, F. (2011). "Electronic Processes at Organic−Organic Interfaces: Insight from Modeling and Implications for Opto-electronic Devices." *Chem. Mater.*, 23 (3), 591–609.

Bellmann, E., Shaheen, S. E., Thayumanavan, S., Barlow, S., Grubbs, R. H., Marder, S. R., Kippelen, B. and Peyghambarian, N. (1998). "New Triarylamine-Containing Polymers as Hole Transport Materials in Organic Light-Emitting Diodes: Effect of Polymer Structure and Cross-Linking on Device Characteristics." *Chem. Mater*., 10 (6), 1668-1676.

Berleb, S., Brütting, W. (2002). "Dispersive Electron Transport in tris (8-Hydroxyquinoline) Aluminum (Alq 3) Probed by Impedance Spectroscopy." *Phys. Rev. Lett.,* 89 (28), 286601-1-286601-4.

Berleb, S., Brütting, W. and Paasch, G. (2001). "Interfacial charges in organic hetero-layer light emitting diodes probed by capacitance - voltage measurements." *Synth. Met*., 122 (1), 37-39.

Berlin, Y. A., Grozema, F. C., Siebbeles, L. D. A. and Ratner,M. A. (2008). "Charge Transfer in Donor-Bridge-Acceptor Systems: Static Disorder, Dynamic Fluctuations, and Complex Kinetics."*J. Phys. Chem. C*., 112 (29), 10988-11000.

Bernanose, A. (1955). "Electroluminescence of organic compounds." *Br. J. Appl. Phys*., 6 (S4), S54-S56.

Bisquert, J., Garcia-Belmonte, G., Pitarch, A. and Bolink, H. J. (2006). "Negative capacitance caused by electron injection through interfacial states in organic light-emitting diodes." *Chem. Phys. Lett.,* 422 (1-3), 184-191.

Bittle, E. G., Basham, J. I., Jackson, T. N., Jurchescu, O. D. and Gundlach, D. J. (2016). "Mobility overestimation due to gated contacts in organic field-effect transistors." *Nat. Commun*., 7 (10908), 1-7.

Blakesley, J. C., Castro, F. A., Kylberg, W., Dibb, G. F. A., Arantes, C., Valaski, R., Cremona, M., Kim, J.S. and Kim, J-S. (2014). "Towards reliable charge-mobility benchmark measurements for organic semiconductors." *Org. Electron*., 15 (6), 1263-1272.

Blom, P. W. M., Vissenberg, M. C. J. M. (2000). "Charge transport in poly(p-phenylenevinylene) light-emitting diodes." *Mat. Sci. Eng.,* 27 (3-4), 53-94.

Boix, P. B., Garcia-Belmonte, G., Munecas, U., Neophytou, M., Waldauf, C. and Pacios, R. (2009). "Determination of gap defect states in organic bulk heterojunction solar cells from capacitance measurements." *Appl. Phys. Lett*., 95 (23), 233302-1-233302-3.

Borsenberger, P. M., Pautmeier, L. T., Bässler, H. (1992). "Nondispersive-to-dispersive charge-transport transition in disordered molecular solids." *Phys. Rev. B.,* 46 (19), 12145-12153.

Brütting, W. (2005). *Physics of Organic Semiconductors*, WILEY-VCH Verlag GmbH & Co. KGaA, Weinheim.

Brütting, W., Berleb, S. and Muckl, A. G. (2001). "Device physics of organic light-emitting diodes based on molecular materials." *Org. Electron.,* 2 (1), 1-36.

Brütting, W., Riel, H., Beierlein, T. and Riess, W. (2001). "Influence of trapped and interfacial charges in organic multilayer light-emitting devices."*J. Appl. Phys*., 89 (3), 1704-1712.

Burin, A. L. and Ratner, M. A. (2000). "Exciton Migration and Cathode Quenching in *Organic Light Emitting Diodes." J. Phys. Chem. A*., 104 (20), 4704-4710.

Campbell, A. J., Bradley, D. D. C. and Antoniadis, H. (2001). "Trap-free, space-charge-limited currents in a polyfluorene copolymer using pretreated indium tin oxide as a hole injecting contact." *Synth. Met*., 122, 161-163.

Carr, J. A. and Chaudhary, S. (2012). "On accurate capacitance characterization of organic photovoltaic cells." *Appl. Phys. Lett*., 100 (21), 213902-1-213902-4.

Carr, J. A. and Chaudhary, S. (2013). "On the identification of deeper defect levels in organic photovoltaic devices." *J. Appl. Phys*., 114 (6), 064509-1-064509-7.

Chauhan, G., Srivastava, R., Tyagi, P., Kumar, A., Srivastava, P. C., Kamalasanan, M. N. (2010). "Frequency dependent electrical transport properties of 4,4′,4″-tris(N-3-methylphenyl-N-phenylamine)triphenylamine by impedance spectroscopy." *Synth. Met*., 160 (13-14), 1422-1426.

Cheung, C. H., Kwok, K. C., Tse, S. C. and So, S. K. (2008). "Determination of carrier mobility in phenylamine by time-of-flight, dark-injection, and thin film transistor techniques." *J. Appl. Phy*., 103 (9), 09375-1-09375-5.

Chu, T. -Y., Song, O. -K. (2007). "Hole mobility of N, N'-bis(napthalen-1-yl)-N,N'-bis(phenyl) benzidine investigated by using space-charge-limited currents." *Appl. Phys. Lett.,* 90 (20), 203512-1-203512-3.

Cicoira, F., Santato, C., Dinelli, F., Murgia, M., Loi, M. A., Biscarini, F., Zamboni, R., Heremans, P. and Muccini, M. (2005). "Correlation Between Morphology and Field-Effect Transistor Mobility in Tetracene Thin Films." *Adv. Funct. Mater*., 15 (3), 375-380.

Coropceanu, V., Cornil, J., Filho, D. A. S., Olivier, Y., Silbey R. and Bre´das, J. –L. (2007). "Charge Transport in Organic Semiconductors." *Chem. Rev*., 107 (4), 926-952.

Craciun, N. I. (2011). "Electrical characterization of polymeric charge transport layers." Ph.D. thesis, University of Groningen, The Netherlands.

Crone, B.K., Campbell, I. H., Davids, P.S. and Smith, D. L. (1998). "Charge injection and transport in single-layer organic light-emitting diodes." *Appl. Phys. Lett*., 73 (21), 3162-3164.

Datta, A. and Pati, S. K. (2004). "Charge-Transfer Induced Large Nonlinear Optical Properties of Small Al Clusters: Al4M4 (M = Li, Na, and K)." *J. Phys. Chem. A*., 108 (44), 9527–9530.

Diard, J. –P., Le Gorrec, B. and Montella, C. (2013). *Handbook of Electrochemical Impedance Spectroscopy-Electrical Circuits Containing CPEs*, Bio-Logic Science

Instruments.

Dieckmann, A., Bässler, H. and Borsenberger. P. M. (1993). "An assessment of the role of dipoles on the density-of-states function of disordered molecular solids." *J. Chem. Phys*., 99 (10), 8136-8141.

Dimitrakopoulos C. D. and Malenfant P. R. L. (2002). "Organic Thin Film Transistors for Large Area Electronics." *Adv. Mater*., 14 (2), 99-117.

Elliott, S. R. (1977). "A theory of a.c. conduction in chalcogenide glasses." *Phil. Mag*., 36 (6), 1291-1304.

Eva , B. M., Ortiz, J., Paya, F. J., Fernandez-Lazaro, F., Fabregat-Santiago, F., Sastre-Santos, A., Bisquert, J. (2010). "Energetic factors governing injection, regeneration and recombination in dye solar cells with phthalocyanine sensitizers." *Energy Environ. Sci*., 3 (12), 1985–1994.

Fan, Z., Zhao, H., Li, N., Quan, Y., Chen, Q., Ye, S., Li, S., Wang, Y., Fan, Q. and Huang, W. (2015). "Tuning Charge Balance in Solution-Processable Bipolar Triphenylamine-diazafluorene Host Materials for Phosphorescent Devices." *ACS Appl. Mater. Interfaces*, 7 (18), 9445–9452.

Fernandes, J. M., Kiran, M. R., Ulla, H., Satyanarayan, M. N. and Umesh, G. (2015). "Investigation of hole transport in α-NPD using impedance spectroscopy techniques with F_4TCNQ as hole-injection layer." *Superlattice. Microst.,* 83, 766-775.

Fernandes, J. M., Kiran, M. R., Ulla, H., Satyanarayan, M. N. and Umesh, G. (2014). "Investigation of hole-injection in a-NPD using capacitance and impedance spectroscopy techniques with F_4TCNQ as hole-injection layer: Initial studies." *Superlattice. Microst.,* 76, 385–393.

Fischer, J., Tress, W., Kleemann, H., Widmer, J., Leo, K. and Riede, M. (2014). "Exploiting diffusion currents at Ohmic contacts for trap characterization in organic semiconductors." *Org. Electron*., 15 (10), 2428–2432.

Fornari, R. P. and Troisi, A. (2014). "Theory of charge hopping along a disordered polymer chain." *Phys. Chem. Chem. Phys*., 16 (21), 9997-10007.

Forrest, S.R. (1997). "Ultrathin Organic Films Grown by Organic Molecular Beam Deposition and Related Techniques." *Chem. Rev*., 97 (6), 1793-1896.

Fukuda, K., Takeda,Y., Mizukami, M., Kumaki, D., Tokito, S. (2014). "Fully Solution-Processed Flexible Organic Thin Film Transistor Arrays with High Mobility and Exceptional Uniformity." *Sci. Rep.,* 4 (3947), 1-8.

Giro, G., Cocchi, M., Kalinowski, J., Fattori, V., Marco, P. D., Dembech, P. and Seconi, G. (1999). "A New Diamine as the Hole-transporting Material for Organic Light-emitting Diodes." *Adv. Mater. Opt. Electron*., 9 (5), 189-194.

Gozzi, G., Queiroz, E. L., Zucolotto, V., Faria R. M. and Chinaglia D. L. (2015). "Hopping–tunneling model to describe electric charge injection at metal/organic semiconductor heterojunctions."*Phys. Status Solidi B.*, 252 (2), 404–410.

Hao, J., Deng, Z. and Yang, S. (2006). "Relationship between exciton recombination zone and applied voltage in organic light-emitting diodes." *Displays*, 27 (3), 108-111.

Harada, K., Sumino, M., Adachi, C., Tanaka, S. and Miyazaki, K. (2010). "Improved thermoelectric performance of organic thin-film elements utilizing a bilayer structure of pentacene and 2,3,5,6-tetrafluoro-7,7,8,8-tetracyanoquinodimethane (F_4-TCNQ)." *Appl. Phys. Lett*., 96 (25), 253304-1-253304-4.

Harrison, M. G., Griiner, J. and Spencer, G. C. W. (1996). "Investigations of organic electroluminescent diodes by impedance spectroscopy, photo-impedance spectroscopy and modulated photovoltage spectroscopy." *Synth. Met*., 76 (1-3), 71-75.

Helander, M. G., Wang, Z. B. and Lu, Z. H. (2008). "Contact formation at the C_{60}/alkali-metal fluoride/Al interface."*Appl. Phys. Lett*., 93 (8), 083311-1-083311-3.

Higashino, T., Akiyama, Y., Kojima, H., Kawamoto, T. and Mori, T. (2012). "Organic semiconductors and conductors with tert-butyl substituents." *Crystals*, 2, 1222-1238.

Hill, R. M. and Jonscher, K. (1979). "DC and AC conductivity in Hopping Electronic Systems." *J. Non-Cryst. Solids*., 32 (1-3), 53-69.

Hsieh, M. –T., Chang, C. –C., Chen, J. –F. and Chen, C. H. (2006). "Study of hole concentration of 1,4-bis[N-(1-naphthyl)-N[sup ′]-phenylamino]-4,4[sup ′] diamine doped with tungsten oxide by admittance spectroscopy." *Appl. Phys. Lett*., 89 (10), 103510-1-103510-3.

Ishihara, S., Hase, H., Okachi, T. and Naito, H. (2011). "Determination of charge carrier mobility in tris(8-hydroxy-quinolinato) aluminum by means of impedance spectroscopy measurements." *Org. Electron*., 12 (8), 1364-1369.

Ishihara, S., Hase, H., Okachi, T. and Naito, H. (2012). "Simulation of impedance spectra of double-layer organic light-emitting diodes for the determination of hole drift mobility of NPB/Alq3 diodes by means of impedance spectroscopy." *Phys. Status. Solidi C*., 9 (12), 2561-2564.

Ishihara, S., Hase, H., Okachi, T. and Naito, H. (2014). "Demonstration of determination of electron and hole drift-mobilities in organic thin films by means of impedance spectroscopy measurements." *Thin Solid Films*, 554, 213-217.

Jonda, C. and Mayer, A. B. R. (1999). "Investigation of the Electronic Properties of Organic Light-Emitting Devices by Impedance Spectroscopy." *Chem. Mater.*, 11 (9), 2429–2435.

Jonscher, A. K. (1977). "The 'Universal' Dielectric Response."*Nature*, 267, 673-79.

Juska, G., Genevicius, K., Arlauskas, K., Osterbacka, R. and Stubb, H. (2002). "Charge transport at low electric fields in π-conjugated polymers." *Phys. Rev. B*., 65 (23), 233208-1-233208-4.

Kanai, K., Honda, M., Ishii, H., Ouchi, Y. and Seki, K. (2012). "Interface electronic structure between organic semiconductor film and electrode metal probed by photoelectron yield spectroscopy." *Org. Electron*., 13 (2), 309–319.

Kern, W. (1993). *Handbook of Semiconductor Wafer Cleaning Technology-Science Technology and Applications*, Noyes Publications, U.S.A.

Kim, J.S., Cacialli, F., Granström, M., Friend, R.H., Johansson, N., Salaneck, W.R., Daik, R. and Feast, W.J. (1999). "Characterisation of the properties of surface-treated indium-tin-oxide thin films." *Synth. Met.*, 101 (1-3), 111-112.

Kim, S. H., Lim, S. C., Lee, J. H. and Zhyung, T. (2005). "Conduction mechanism of organic semiconductor AlQ3: Impedance spectroscopy analysis." *Curr. Appl. Phys*., 5 (1), 35–37.

Kim, S. K., Choi, K. –H.,Lee, H. –M., Hwang, D. –H., Do, L. –M., Chu, H. –Y. and Zyung, T. (2000). "Impedance spectroscopy of single- and double-layer polymer light-emitting diode." *J. Appl. Phys*., 87 (2), 882-888.

Klauk, H. (2012). *Organic Electronics II: More Materials and Applications*, Wiley-VCH Verlag GmbH & Co. KGaA.

Koch, N. (2007). "Organic electronic devices and their functional interfaces." *ChemPhysChem*., 8 (10), 1438-1455.

Koch, N., Salzmann, I., Johnson, R. L., Pflaum, J., Friedlein, R. and Rabe, J. P. (2006). "Molecular orientation dependent energy levels at interfaces with pentacene and pentacenequinone." *Org. Electron*., 7 (6), 537–545.

Kocherzhenko, A. A. (2011). "Charge Transport in Disordered Molecular Sytems." Ph.D. Dissertation, Delft University Press: The Netherlands.

Kokil, A., Yang, K. and Kumar, J. (2012). "Techniques for Characterization of Charge Carrier Mobility in Organic Semiconductors." *J. Polym. Sci. Pol. Phys*., 50 (15), 1130-1144.

Kramer, B. (2002). *Advances in Solid State Physics*, *Volume 42*, Springer-Verlag, Berlin Heidelberg.

Kumar, P. (2017). *Organic Solar Cells-Device Physics, Processing, Degradation and Prevention*, CRC Press, Taylor & Francis Group, Boca Raton.

Kumar, P., Sharma, A., Ray Chaudhuri, S., Ghosh, S. (2011). "Effect of deep traps on small molecule based thin film transistors." *Appl. Phys. Lett.,* 99 (17), 173304-1-173304-3.

Lampert, M. A. and Mark, P. (1970). *Current injection in solids*, New York, Academic Press.

Landi, G., Tunc, A.V, Sio, A. D., Parisi, J. and Neitzert, H. –C. (2016). "Hole-mobility limits for the $Zn(OC)_2$ organic semiconductor obtained by SCLC and field-effect measurements." *Phys. Stat. Sol A.*, 213 (7), 1909–1914.

Lee, J. –H., Lee, J., Kim, Y. H., Yun, C., Lüssem, B. and Leo, K. (2014). "Effect of trap states on the electrical doping of organic semiconductors." *Org. Electron*., 15 (1), 16-21.

Lee, Y. S., Park, J. -H. and Choi, J. S. (2003). "Frequency-Dependent Electrical Properties of Organic Light-Emitting Diodes." *J. Korean Phys. Soc*., 42 (2), 294-297.

Leung, L. M., Law, Y. –C., Wong, M. Y., Lee, T. –H., Lai, K. M. and Tang, L. -Y. (2009). "Charge balance materials for homojunction and heterojunction OLED applications." *Front. Optoelectron. China*., 2 (4), 435-441.

Li, C. N., Djurisic, A.B., Kwong, C. Y., Lai, P. T., Chan, W. K. and Liu, S. Y. (2005). "Indium tin oxide surface treatments for improvement of organic light-emitting diode performance." *Appl. Phys. A*., 80, 301-307.

Li, L., Meller, G. and Kosina, H. (2007). "Influence of traps on charge transport in organic semiconductors", *Solid State. Electron*., 51 (3), 445-448.

Li, Z. and Meng, H. (2006). *Organic Light-Emitting Materials & Devices*, Taylor & Francis Group, New York.

Liu, F., Ruden, P. P., Campbell, I. H. and Smith, D. L. (2012). "Device model for electronic processes at organic/organic interfaces." *J. Appl. Phys*., 111 (9), 094507-1 - 094507-12.

Liu, J., Duan, C. –G., Yin, W. –G., Mei, W. –N., Smith, R. W. and Hardy, J. R. (2004). "Large dielectric constant and Maxwell-Wagner relaxation in Bi2/3Cu3Ti4O12." *Phys. Rev. B*., 70 (14), 144106.

Liu, J., Zhang, H., Dong, H., Meng, L., Jiang, L., Jiang, L., Wang, Y., Yu, J., Sun, Y., Hu, W. and Heeger, A. J. (2015). "High mobility emissive organic semiconductor." *Nat. Commun*., 6 (10032), 1-8.

Lu, L., Kelly, M. A., You, W. and Yu, L. (2015). "Status and prospects for ternary organic photovoltaics." *Nat. Photon*., 9, 491–500.

MacDonald, J. R. (1992). "Impedance spectroscopy." *Ann. Biomed. Eng.*, 20 (3), 289-305.

Malliaras, G. G. and Scott, J. C. (1999). "Numerical simulations of the electrical characteristics and the efficiencies of single-layer organic light emitting diodes." *J. Appl. Phys*., 85 (10), 7426-7432.

Mansour, S. O., Louati, B. and Guidara, K. (2015). "AC conductivity and dielectric behavior of high-temperature form of copper silver phosphate." *Ionics*, 21 (7), 1973–1982.

Marcus, R. A. (1956). "Electrostatic Free Energy and Other Properties of States Having Nonequilibrium Polarization. I". *J. Chem. Phys.*, 24 (5), 979.

Marcus, R. A. (1956). "On the Theory of Oxidation-Reduction Reactions Involving Electron Transfer. I." *J. Chem. Phys*., 24 (5), 966.

Martens, H. C. F., Brom, H. B., Blom, P. W. M. (1999). "Frequency-dependent electrical response of holes in poly(p-phenylenevinylene)." *Phys. Rev. B.,* 60 (12), 8489-8492.

Martens, H. C. F., Huiberts, J. N., Blom, P. W. M. (2000). "Simultaneous measurement of electron and hole mobilities in polymer light-emitting diodes." *Appl. Phys. Lett*., 77 (12), 1852-1854.

Mazzeo, M. (2010). *Organic Light Emitting Diode*, Sciyo, Croatia.

Mesta, M., Cottaar, J., Coehoorn, R. and Bobbert, P. A. (2014). "Study of charge-carrier relaxation in a disordered organic semiconductor by simulating impedance spectroscopy." *Appl. Phys. Lett.,* 104 (21), 213301-1-213301-4.

Miller A. and Abrahams, E. (1960). "Impurity Conduction at Low Concentrations." *Phys. Rev.*, 120 (3), 745-755.

Montero, J. M. and Bisquert, J. (2011). "Trap origin of field-dependent mobility of the carrier transport in organic layers." *Solid State Electron*., 55 (1), 1-4.

Montes, V.A., Li, G., Pohl, R., Shinar, J. and Anzenbacher, P. Jr. (2004). "Effective Color Tuning in Organic Light-Emitting Diodes Based on AluminiumTris(5-aryl-8-hydroxyquinoline) Complexes." *Adv. Mater*., 16 (22), 2001-2003.

Mott, N. F. and Gurney, R. W. (1940). *Electronic Processes in Ionic Crystals*, Oxford University Press, London.

Mückl, A. G., Berleb, S., Brütting, W. and Schwoerer, M. (2000). "Transient electroluminescence measurements on organic heterolayer light emitting diodes." *Synth. Met*., 111-112, 91-94.

Nagakubo, J., Ashizawa, M., Kawamoto, T., Tanioka, A. and Mori, T. (2011). "Stabilization of organic field-effect transistors by tert-butyl groups in dibenzotetrathiafulvalene derivatives." *Phys. Chem. Chem. Phys*., 13 (32), 14370–14377.

Navamani, K. and Senthilkumar, K. (2014). "Effect of Structural Fluctuations on Charge Carrier Dynamics in Triazene Based Octupolar Molecules."*J. Phys. Chem. C*., 118 (48), 27754−27762.

Navamani, K. and Senthilkumar, K. (2015). "Effect of dynamic disorder on charge carrier dynamics in Ph4DP and Ph4DTP molecules."*RSC Adv*., 5 (48), 38722-38732.

Navamani, K. and Senthilkumar, K. (2015). "Forth–back oscillated charge carrier motion in dynamically disordered hexathienocoronene molecules: a theoretical study." *Phys. Chem. Chem. Phys*., 17 (27), 17729-17738.

Navamani, K., Saranya, G., Kolandaivel, P. and Senthilkumar, K. (2013). "Effect of Structural Fluctuations on Charge Carrier Mobility in Thiophene, Thiazole and Thiazolothiazole based Oligomers." *Phys. Chem. Chem. Phys*., 15 (41), 17947-17961.

Ng, T. N., Silveira, W. R. and Marohn, J. A. (2007). "Dependence of Charge Injection on Temperature, Electric Field, and Energetic Disorder in an Organic Semiconductor." *Phys. Rev. Lett*., 98 (6), 066101-1-066101-4.

Nguyen, N. D., Schmeits, M. and Loebl, H. P. (2007). "Determination of charge-carrier transport in organic devices by admittance spectroscopy: Application to hole mobility in α-NPD." *Phys. Rev. B*., 75 (7), 075307-1-075307-13.

Nguyen, P. H., Scheinert, S., Berleb, S., Brütting, W., Paasch, G. (2001). "The influence of deep traps on transient current - voltage characteristics of organic light-emitting diodes." *Org. Electron.,* 2 (3-4), 105-120.

Nowy, S., Ren, W., Elschner, A., Lövenich, W. and Brütting, W. (2010). "Impedance spectroscopy as a probe for the degradation of organic light-emitting diodes." *J. Appl. Phys*., 107 (5), 054501-1-054501-9.

Nowy, S., Ren, W., Wagner, J., Weber, J. A. and Brütting, W. (2009). "Impedance spectroscopy of organic hetero-layer OLEDs as a probe for charge carrier injection and device degradation." *Proc. SPIE*., 7415, 74150G-74150G-12.

Okachi, T., Nagase, T., Kobayashi, T., Naito, H. (2008). "Determination of Charge-Carrier Mobility in Organic Light-Emitting Diodes by Impedance Spectroscopy in Presence of Localized States." *Jpn. J. Appl. Phys*., 47 (12R), 8965-8972.

Ono, R., Kiy, M., Biaggio, I. and Gu, P. (2001). "Impurity-gas-dependent charge injection properties at the electrode – organic interface in organic light-emitting diodes." *Mat. Sci. Eng. B*., 85 (2-3), 144-148.

Ooi, Z. -E., Danielson,E., Liang, K., Lombardo, C.,Dodabalapur, A. (2014). "Evaluating Charge Carrier Mobility Balance in Organic Bulk Heterojunctions using Lateral Device Structures." *J. Phys. Chem. C*., 118 (32), 18299–18306.

Opitz, A., Wilke, A., Amsalem, P., Oehzelt, M., Blum, R.-P., Rabe, J. P., Mizokuro, T., Hörmann, U., Hansson, R., Moons, E. and Koch, N. (2016). "Organic heterojunctions: Contact induced molecular reorientation, interface states, and charge redistribution."*Sci. Rep*., 6 (21291), 1-9.

Oshiro, T., Tamura, T., Kageyama, H., Shirota, Y., Kajii, H. and Ohmori, Y. (2012). "Performance of blue fluorescence and red phosphorescent organic light-emitting diodes using a molecular material with high hole drift mobility." *Phys. Stat. Sol. C*., 9 (12), 25-49-2552.

Paek, S., Cho, N., Cho, S., Lee, J. K. and Ko, J. (2012). "Planar star-shaped organic semiconductor with fused triphenylamine core for solution-processed small-molecule organic solar cells and field-effect transistors." *Org. Lett*., 14 (24), 6326-9.

Pahner, P., Kleemann, H., Burtone, L., Tietze, M. L., Fischer, J., Leo, K. and Lüssem, B. (2013). "Pentacene Schottky diodes studied by impedance spectroscopy: Doping properties and trap response." *Phys. Rev. B*., 88 (19), 195205 –1-195205 –8.

Park, H., Kim, H., Dhungel, S. K., Yi, J., Sohn, S. Y. and Jung, D. G. (2007). "Impedance Spectroscopy Analysis of Organic Light-Emitting Diodes Fabricated on Plasma-Treated Indium-Tin-Oxide surfaces." *J. Kor. Phys. Soc*., 51 (3), 1011-1015.

Petty, M.C., Pearson, C., Monkman, A.P., Casalini, R., Capaccioli, S. and Nagel, J. (2000). "Application of impedance spectroscopy to the study of organic multilayer devices." *Colloids Surface A*., 171 (1-3), 159-166.

Philippa, B., Stolterfoht, M., Burn, P. L., Juška, G., Meredith, P., White , R. D., Pivrikas, A. (2014). "The impact of hot charge carrier mobility on photocurrent losses in polymer-based solar cells." *Sci. Rep.,* 4 (5695), 1-7.

Philippa, B., Vijila, C., White, R. D., Sonar, P., Burn, P. L., Meredith, P., Pivrikas, A. (2015). "Time-independent charge carrier mobility in a model polymer:fullerene organic solar cell." *Org. Electron.*, 16, 205–211.

Pingree, L. S. C., Russell, M. T., Marks, T. J. and Hersam, M. C. (2007). "Monitoring interface traps in operating organic light-emitting diodes using impedance spectroscopy." *Thin Solid Films*, 515 (11), 4783-4787.

Pivrikas, A., Neugebauer, H. and Sariciftci, N. S. (2010). "Charge Carrier Lifetime and Recombination in Bulk Heterojunction Solar Cells." *IEEE. J. Sel. Top. Quant*., 16 (6), 1746-1758.

Pope, M., Kallmann, H.P. and Magnante, P. (1963). "Electroluminescence in Organic Crystals." *J. Chem. Phys*., 38 (8), 2042-2043.

Prasad, P. N. (2012). *Frontiers of Polymers and Advanced Materials*, Springer, Plenum Press, New York.

Pross, A., Radom, L. and Riggs, N. V. (1980). "A Theoretical Approach to Substituent Effects. Structural Consequences of Methyl Hyperconjugation.Methyl Tilt Angles and C-H Bond Lengths." *J. Am. Chem. Soc*., 102 (7), 2253- 2259.

Ramar, M., Tyagi, P., Suman, C. K. and Srivastava, R. (2014). "Enhanced carrier transport in tris(8-hydroxy-quinolinato) aluminum by titanylphthalocyanine doping." *RSC Adv.,* 4 (93), 51256-51261.

Rana, O., Srivastava, R., Chauhan, G., Zulfequar, M., Husain, M., Srivastava, P. C. and Kamalasanan, M. N. (2012). "Modification of metal–organic interface using F_4-TCNQ for enhanced hole injection properties in optoelectronic devices."*Phys. Status Solidi A.,* 209 (12), 2539–2545.

Ray, B., Baradwaj, A. G., Boudouris, B. W. and Alam, M. A. (2014). "Defect Characterization in Organic Semiconductors by Forward Bias Capacitance-Voltage (FB-CV) Analysis." *J. Phys. Chem. C*., 118 (31), 17461-17466.

Ryno, S. M., Fu, Y. T., Risko, C. and Brédas J. L. (2016). "Polarization Energies at Organic-Organic Interfaces: Impact on the Charge Separation Barrier at Donor-Acceptor Interfaces in Organic Solar Cells." *ACS Appl. Mater. Interfaces*., 8 (24), 15524-34.

Salaneck, W. R., Strafstrom, S. and Bredas, J. L. (1996). *Conjugated Polymer Surfaces and Interfaces: Electronic and Chemical Structure of Interfaces for Polymer Light Emitting Devices*, Cambridge University Press, Cambridge.

Salzmann, I., Heimel, G., Oehzelt, M., Winkler, S. and Koch, N. (2016). "Molecular Electrical Doping of Organic Semiconductors: Fundamental Mechanisms and Emerging Dopant Design Rules." *Acc. Chem. Res*., 49 (3), 370-378.

Scher, H., Montroll, E. W. (1975). "Anomalous transit-time dispersion in amorphous solids." *Phys. Rev. B*., 12 (6), 2455-2477.

Scholls, S. (2011). *Device Architecture and Materials for Organic Light-Emitting Devices*, Springer, Dordrecht.

Schönhals, A. (1998). *Dielectric Spectroscopy on the Dynamics of Amorphous Polymeric Systems*, Application Note Novocontrol GmbH, Germany.

Sergiyenko, O. (2011). *Optoelectronic Devices and Properties*, InTech, Croatia.

Shan, B. and Miao, Q. (2017). "Molecular Design of N-Type Organic Semiconductors for High-Performance Thin Film Transistors." *Tetrahedron Lett*., 58 (20), 1903-1911.

Sharma, A., Kumar, P., Singh, B., Chaudhuri, S.R. and Ghosh, S. (2011). "Capacitance-voltage characteristics of organic Schottky diode with and without deep traps." *Appl. Phys. Lett.,* 99 (2), 023301-1-023301-3.

Sharma, A., Yadav, S., Kumar, P., Chaudhuri, S.R. and Ghosh, S. (2013). "Defect states and their energetic position and distribution in organic molecular semiconductors." *Appl. Phys. Lett.,* 102 (14), 143301-1-143301-5.

Shinar, J. (2004). *Organic light emitting devices- A survey*, Springer, 1st edition, New York.

Shirota, Y. and Kageyama, H. (2007). "Charge Carrier Transporting Molecular Materials and Their Applications in Devices." *Chem. Rev*.,107 (4), 953-1010.

So, S. K., Tse, S. C. and Tong , K. L. (2007). "Charge Transport and Injection to Phenylamine-Based Hole Transporters for OLEDs Applications." *J. Disp. Technol*., 3 (2), 225-232.

Stallinga, P. (2009). *Electrical Characterization of Organic Electronic Materials and Devices*, Wiley, U.K.

Suman, C. K., Yun, J., Kim, S., Lee, S. –D. and Lee, C. (2009). "AC impedance spectroscopic studies of transport properties in metal oxide doped α-NPD." *Curr. Appl. Phys*., 9 (5), 978–984.

Sze, S. M. and Ng, K. K. (2007). *Physics of Semiconductor Devices*, Wiley, U.S.A.

Takagi, K., Nagase, T., Kobayashi, T. and Naito, H. (2016). "Determination of deep trapping lifetime in organic semiconductors using impedance spectroscopy." *Appl. Phys. Lett*.,108 (5), 053305.

Tang, C. W. and VanSlyke, S. A. (1987). "Organic electroluminescent diodes." *Appl. Phys. Lett*., 51 (12), 913-915.

Tang, C., Yu, H., Wang, X., Liu, W., Liu, R., Rong, Z., Fan, Q. and Huang, W. (2013). "Study of carrier mobility of N,N'-diphenyl-N,N'bis(1,1'-biphenyl)-4,4'-diamine (NPB) by transmission line model of impedance spectroscopy." *Thin Solid Films*, 542, 281-284.

Tang, Y., Peng, Y., Sun, L., Wei, Y. and Xu, S. (2015). "Determining charge carrier mobility in Schottky contacted single-carrier organic devices by impedance spectroscopy." *EPL* (*Europhys. Lett*.), 112 (1), 17007-1-17007-5.

Tao, Y., Wang, Q., Shang, Y., Yang, C., Ao, L., Qin, J., Ma, D. and Shuai, Z. (2009). "Multifunctional bipolar triphenylamine/oxadiazole derivatives: highly efficient blue fluorescence, red phosphorescence host and two-color based white OLEDs."*Chem. Commun*., 1, 77-79.

Tessler, N., Preezant, Y., Rappaport, N. and Roichman, Y. (2009). "Charge Transport in Disordered Organic Materials and Its Relevance to Thin-Film Devices: A Tutorial Review." *Adv. Mater*., 21 (27), 2741-2761.

Thesen, M. W., Hofer, B., Debeaux, M., Janietz, S., Wedel, A., Kohler, A., Johannes, H.-H. and Krueger, H. (2010). "Hole-Transporting Host-Polymer Series Consisting of Triphenylamine Basic Structures for Phosphorescent Polymer Light-Emitting Diodes." *J. Polym. Sci.: Part A: Polym. Chem*., 48 (15), 3417–3430.

Tian, G., Huang, W., Cai, S., Zhou, H., Li, B., Wang, Q. and Su, J. (2014). "Small molecules based on diphenylamine and carbazole with large two-photon absorption cross sections and extraordinary AIEE properties." *RSC Adv.***,** 4 (73), 38939-38942.

Tiwari, S. and Greenham, N. C. (2009). "Charge mobility measurement techniques in organic semiconductors." *Opt. Quant. Electron*., 41 (2), 69-89.

Tong, K. L., Tsang, S. W., Tsung, K. K., Tse, S. C., So, S. K. (2007). "Hole transport in molecularly doped naphthyl diamine." *J. Appl. Phys.,* 102 (9), 093705-1-093705-5.

Tour, J. M. (1996). "Conjugated Macromolecules of Precise Length and Constitution. Organic Synthesis for the Construction of Nanoarchitectures." *Chem. Rev.,* 96 (1), 537-554.

Tress, W. (2014). *Organic Solar Cells-Theory, Experiment, and Device Simulation*, Springer, Switzerland.

Tripathi, A. K., Ashish and Mohapatra, Y. N. (2010). "Mobility with negative coefficient in Poole-Frenkel field dependence in conjugated polymers: Role of injected hot electrons." *Org. Electron*., 11 (11), 1753-1758.

Tripathi, D. C. and Mohapatra, Y. N. (2014). "Charge transport across organic heterostructure: Role of interfacial density of states." *J. Appl. Phys*., 116 (6), 064509-1-064509-10.

Tripathi, D. C., Mohapatra, Y. N. (2013). "Diffusive capacitance in space charge limited organic diodes: Analysis of peak in capacitance-voltage characteristics." *Appl. Phys. Lett.,* 102 (25), 253303-1-253303-5.

Tripathi, D. C., Tripathi A. K. and Mohapatra, Y. N. (2011). "Mobility determination using frequency dependence (Im Z) for organic and polymeric thin films." *Appl. Phys. Lett*., 98 (3), 033304-1-033304-3.

Troadec, D., Veriot, G., Antony, R. and Moliton, A. (2001). "Organic light-emitting diodes based on multilayer structures." *Synth. Met.*, 124 (1), 49-51.

Troisi, A. (2011). "Charge transport in high mobility molecular semiconductors: classical models and new theories."*Chem. Soc. Rev*. 40 (5), 2347-2358.

Troisi, A. and Cheung, D. L. (2009). "Transition from dynamic to static disorder in one-dimensional organic semiconductors." *J. Chem. Phys*., 131 (1), 014703.

Tsang, S. W., So, S. K. (2006). "Application of admittance spectroscopy to evaluate carrier mobility in organic charge transport materials." *J. Appl. Phys.,* 99 (1), 013706-1-013706-7.

Tsung, K. K. and So, S. K. (2009). "Advantages of admittance spectroscopy over time-of-flight technique for studying dispersive charge transport in an organic semiconductor." *J. Appl. Phys*., 106 (8), 083710-1-083710-5.

Tyagi, P., Dalai, M. K., Suman, C. K., Tuli, S. and Srivastava, R. (2013). "Study of 2,3,5,6-tetrafluoro-7,7′,8,8′- tetracyanoquinodimethane diffusion in organic light

emitting diodes using secondary ion mass spectroscopy." *RSC Adv*., 3 (46), 24553-24559.

Uemura , T., Rolin, C., Ke, T.-H., Fesenko, P., Genoe, J., Heremans, P. and Takeya, J. (2016). "On the Extraction of Charge Carrier Mobility in High-Mobility Organic Transistors." *Adv. Mater.*, 28 (1), 151–155.

van Mensfoort, S. L. M. and Coehoorn, R. (2008). "Effect of Gaussian disorder on the voltage dependence of the current density in sandwich-type devices based on organic semiconductors." *Phys. Rev. B*., 78 (8), 085207-1-085207-16.

Varo, P. L., Tejada, J. A. J., Villanueva, J. A. L., Carceller, J. E. and Deen, M. J. (2012). "Modeling the transition from ohmic to space charge limited current in organic semiconductors." *Org. Electron*., 13 (9), 1700-1709.

Vincett, P. S., Barlow, W. A., Hann, R. A. and Roberts, G. G. (1982). "Electrical conduction and low voltage blue electroluminescence in vacuum-deposited organic films." *Thin Solid Films*, 94 (2), 171-183.

Wang, Y., Zhang, X., Han, B., Peng, J., Hou, S., Huang, Y., Sun, H., Xie, M. and Lu, Z. (2010). "The synthesis and photoluminescence characteristics of novel blue light-emitting naphthalimide derivatives." *Dyes Pigments*., 86 (2), 190-196.

Wee, K. –R., Ahn, H. –C., Son, H. –J., Han, W. –S., Kim, J. –E., Cho, D. W. and Kang, S. O. (2009). "Emission Color Tuning and Deep Blue Dopant Materials Based on 1,6-Bis(*N*-phenyl-*p*-(*R*)-phenylamino)pyrene." *J. Org. Chem.*, 74 (21), 8472–8475.

Weis, M., Otsuka, T., Taguchi, D., Manaka, T. and Iwamoto, M. (2015). "Charge injection and accumulation in organic light-emitting diode with PEDOT:PSS anode." *J. Appl. Phys*., 117 (15), 155503-1-113706-7.

Wolf, U., Arkhipov, V. I. and Bässler, H. (1999). "Current injection from a metal to a disordered hopping system. I. Monte Carlo simulation." *Phys. Rev. B*., 59 (11), 7507-7513.

Woon, K. L., Nadiah, Z. N., Hasan, Z. A., Ariffin, A. and Chen, S. A. (2016). "Tuning the singlet-triplet energy splitting by fluorination at 3,6 positions of the 1,4-biscarbazoylbenzene." *Dyes Pigments*, 132, 1-6.

Wu, I. –W., Wang, P. –S., Tseng, W. –H., Chang, J. –H. and Wu, C. –I. (2012). "Correlation of impedance-voltage characteristics and carrier mobility in organic light emitting diodes." *Org. Electron*., 13 (1), 13-17.

Wu, S., Li. S., Sun, Q., Huang, C. and Fung, M.-K. (2016). "Highly Efficient White Organic Light-Emitting Diodes with Ultrathin Emissive Layers and a Spacer-Free Structure." *Sci. Rep.,*6 (25821), 1-8.

Xu, H., Tang, C., Wang, X. -L., Liu, W., Liu, R. -L., Rong, Z., Fan, Q. -L., Huang, W. (2014). "Application of capacitance spectrum and the imaginary part of impedance spectrum to study carrier dynamics of N,N′-diphenyl-N,N′bis(1,1′-biphenyl)-4,4′-diamine." *Thin Solid Films*, 556, 447-451.

Xu, Y. F., Tao, Y.S., Zhang, H. J., Chen, X. Z., Cao, G. H., Xu, Z. A., Li, H.Y., Bao, S. N. and He, P. (2005). "Impedance spectroscopy study on transport properties of N,N'-diphenyl-N,N'bis(1-naphthyl)- 1,1'-biphenyl-4,4'-diamine." *Physica B: Phys. Cond. Mat*., 362 (1-4), 35-40.

Yonezawa , K., Hinderhofer , A., Hosokai , T., Kato , K., Makino , R., Schreiber , F., Ueno , N. and Kera, S. (2014). "Structural Defects Control the Energy Level Alignment at Organic/Organic Interfaces." *Adv. Mater. Interfaces*, 1 (5), 1400004-1-1400004-5.

Zhan, Y. Q., Zhou, J., Zhou, Y. C., Wu, Y., Yang, H., Li, F. Y., Ding, X. M. and Hou, X. Y. (2007). "The effect of dopant-induced electron traps on spectrum evolution of doped organic light-emitting devices", *Thin Solid Films*, 515 (13), 5449-5453.

Zhang, L., Nakanotani, H. and Adachi, C. (2013). "Capacitance-voltage characteristics of a 4,4′-bis[(N-carbazole)styryl]biphenyl based organic light-emitting diode: Implications for characteristic times and their distribution." *Appl. Phys. Lett*., 103 (9), 093301-1-093301-40.

Zheng, Y.-Q., Potscavage Jr., W. J., Komino, T. and Adachi, C. (2013). "Highly efficient bulk heterojunction photovoltaic cell based on tris[4-(5-phenylthiophen-2-yl)phenyl]amine and C_{70} combined with optimized electron transport layer." *Appl. Phys. Lett*., 102 (15), 153302.

LIST OF PUBLICATIONS

PUBLICATIONS IN PEER-REVIEWED INTERNATIONAL JOURNALS

1. **Jean Maria Fernandes**, Chidirala Swetha, Ejjirothu Appalnaidu, K. Navamani, V. Jayathirtha Rao, M. N. Satyanarayan, G. Umesh, "Optoelectronic properties of novel alkyl-substituted Triphenylamine derivatives." *Organic Electronics* (2017) 47, 24-34.
2. **Jean Maria Fernandes**, M. Raveendra Kiran, H. Ulla, M. N. Satyanarayan, G. Umesh, "Investigation of hole transport in α-NPD using impedance spectroscopy with F_4TCNQ as hole-injection layer." *Superlattices and Microstructures* (2015) 83, 766-775.
3. **Jean Maria Fernandes**, M. Raveendra Kiran, H. Ulla, M. N. Satyanarayan, G. Umesh, "Investigation of hole-injection in α-NPD using capacitance and impedance spectroscopy techniques with F_4TCNQ as hole-injection layer: Initial studies." *Superlattices and Microstructures* (2014) 76, 385-393.

PRESENTATIONS IN INTERNATIONAL CONFERENCES

1. **Jean Maria Fernandes**, M. Raveendra Kiran, Hidayath Ulla, M. N. Satyanarayan, G. Umesh, "*Studies on hole injection properties of F_4-TCNQ in organic light emitting diodes*", First International Conference on Emerging Materials: Characterization and Application (EMCA-2014), NIT, Durgapur and CSIR-Central Glass & Ceramic Research Institute, Kolkata, Dec 4-6, 2014.
2. **Jean Maria Fernandes**, B. Garudachari, Hidayath Ulla, M. N. Satyanarayan, G. Umesh and A.M. Isloor, "*Novel Naphthalimide Derivatives as Blue Emitting Components in Potential Organic Light Emitting Diode Applications*", ICRAMST-13, Department of Chemistry, NITK Surathkal, Mangalore, Jan 17-19, 2013.

JEAN MARIA FERNANDES

5-151/24
Ashoknagar P.O.
Mangalore – 575006
Karnataka

Email: jean.nitk@gmail.com
Phone: +91- 9535616508

QUALIFICATION

- **PhD in Physics** [Successful completion of Thesis Defense: February 2018]
  Title : "Charge Transport Investigations in Novel Triarylamine Derivatives Based Organic Devices"
  Institute : National Institute of Technology Karnataka, Surathkal

- **M.Sc. (Physics)** [2010]
  National Institute of Technology Karnataka, Surathkal

- **B.Sc. (Physics, Mathematics and Electronics)** [2008]
  St. Aloysius College, Mangalore University

PUBLICATIONS IN PEER-REVIEWED INTERNATIONAL JOURNALS

1. **Jean Maria Fernandes**, Chidirala Swetha, Ejjirothu Appalnaidu, K. Navamani, V. Jayathirtha Rao, M. N. Satyanarayan, G. Umesh (2017) "Optoelectronic properties of novel alkyl-substituted Triphenylamine derivatives." *Organic Electronics*, 47, 24-34.

2. **Jean Maria Fernandes**, M. Raveendra Kiran, H. Ulla, M. N. Satyanarayan, G. Umesh, (2015) "Investigation of hole transport in α-NPD using impedance spectroscopy with F_4TCNQ as hole-injection layer." *Superlattices and Microstructures*, 83, 766-775.

3. **Jean Maria Fernandes**, M. Raveendra Kiran, H. Ulla, M. N. Satyanarayan, G. Umesh, (2014) "Investigation of hole-injection in α-NPD using capacitance and impedance spectroscopy techniques with F_4TCNQ as hole-injection layer: Initial studies." *Superlattices and Microstructures*, 76, 385-393.

PRESENTATIONS IN CONFERENCES

1. M. Raveendra Kiran, Hidayath Ulla, **Jean M. Fernandes**, M. N. Satyanarayan, G. Umesh, (2015) "Electrical Characterization of hybrid hetero interface using n-ZnO and p-CuPc", Materials Today: Proceedings, 2, 1230-1233.

2. M. Raveendra Kiran, Hidayath Ulla, **Jean Maria Fernandes**, M. N. Satyanarayan, G. Umesh, "Investigation of Impedance Spectroscopy of Inorganic/Orgnic Hybrid p-n Junction Based on ZnO and CuPc", National Conference on Condensed Matter Physics and Applications (CMPA 2015), Manipal Institute of Technology, Manipal University, Mar 27-28, 2015.
3. **Jean Maria Fernandes**, M. Raveendra Kiran, Hidayath Ulla, M. N. Satyanarayan, G. Umesh, "Studies on hole injection properties of F_4-TCNQ in organic light emitting diodes", First International Conference on Emerging Materials: Characterization and Application (EMCA-2014), NIT, Durgapur and CSIR-Central Glass & Ceramic Research Institute, Kolkata, Dec 4-6, 2014.
4. **Jean Maria Fernandes**, B. Garudachari, Hidayath Ulla, M. N. Satyanarayan, G. Umesh and A.M. Isloor, "Novel Naphthalimide Derivatives as Blue Emitting Components in Potential Organic Light Emitting Diode Applications", ICRAMST-13, Department of Chemistry, NITK Surathkal, Mangalore, Jan 17-19, 2013.
5. Hidayath Ulla, Garudachari, B., **Jean Maria Feranandes**, Satyanarayan, M.N., Umesh, G., Isloor, A.M., "Potential blue emitting materials for Organic Light Emitting Diodes", National Seminar on Current Trends in Materials Science (NSCTMS-2012), Kottayam, Kerala, Mar 7-8, 2012.
6. Hidayath Ulla, B. Garudachari, **Jean Maria Fernandes**, M.N. Satyanarayan, G. Umesh and Arun M. Isloor, "Synthesis and characterization of novel naphthalimide derivatives for blue light organic light emitting diodes", International Conference on Recent Trends in Advanced Materials (ICRAM 2012) VIT, Vellore, Feb 20-22, 2012.

TEACHING EXPERIENCE

- **Teaching Assistant -** National Institute of Technology Karnataka, Surathkal

  Courses:

  1. Engineering Physics Laboratory course for B.Tech. students [August 2010 - April 2014]
  2. Physics Laboratory course for M.Sc. students [August 2011 - April 2014]
  3. Physics Tutorials for M.Sc. students [August 2012 - November 2012]

RESEARCH EXPERIENCE

- **Participation in** - Research Project [12(3)/2010-PDD - Ministry of Electronics and Information Technology, Government of India]: 'Fabrication and Characterization of Blue Organic Light Emitting Diodes (OLEDs)' - National Institute of Technology Karnataka, Surathkal, [August 2010 - July 2013]

- **M.Sc. Research Project** - 'Growth and Characterization of Cadmium Telluride Thin Films for TFT Transistor Applications', National Institute of Technology Karnataka, Surathkal, [July 2009 - May 2010]

AWARDS/ SCHOLARSHIPS/ FELLOWSHIPS OBTAINED

- **Sir C. V. Raman Scholarship** [2005-2008] **-** Department of Collegiate Education, Karnataka
- **Government of India National Hindi Scholarship** [2005-2007] - Department of Collegiate Education, Karnataka
- **Endowed Scholarship** [2007-2008] - The Old Boys of St. Aloysius College Based in UAE Scholarship
- **Academic Excellence Award** [2008] - Yenepoya Foundation, a unit of YMK Memorial Educational and Charitable Trust (Regd.) and Yenepoya University, Mangalore
- **PhD Junior and Senior Research Fellowship** [2010-2015] - National Institute of Technology Karnataka, Surathkal

PRACTICAL EXPERIENCE/SKILLS

- Conversant with handling thermal vacuum evaporation system with turbo-molecular pump and diffusion pump along with spin-coating unit and experienced in device fabrication process.
- Experienced in characterization of organic devices using Keithley 2400 Sourcemeter and Agilent E4980a LCR meter and also their computer-controlled interface.
- Familiar with using Ocean Optics UV-Vis Spectrometer, glove box, oscilloscopes and basic electronic circuitry.
- Sound knowledge in using basic software such as MS Office; basic knowledge of C programming, Linux, hardware and networking, and scientific software such as Origin, Materials Studio, COMSOL Multiphysics and MATLAB.

WORKSHOPS AND SEMINARS/CONFERENCES ATTENDED

- Participated in the Global Initiative of Academic Networks course on "Organic Semiconductors for Microelectronics & Display Applications", May 30-June 03, 2016, at National Institute of Technology Karnataka, Surathkal.
- Participated in the "International Winter School on Organic Electronic Materials & Devices (OEMD-2013)", December 19-21, 2013, at National Institute of Technology Karnataka, Surathkal.

- Attended the "Workshop on Quantum Mechanics and Applications", March 22-24, 2013, at Department of Physics, National Institute of Technology Karnataka, Surathkal.
- Attended the Short Course on "Organic Solar Cells", 4th to 9th July, 2011, at Samtel Centre for Display Technologies, IIT Kanpur.
- Participated in the "MEMS design software training program" organized under National Program on Micro and Smart Structures (NPMASS), 30 May-4 June, 2011, at MEMS Design Centre, National Institute of Technology Karnataka, Surathkal.
- Attended a one day symposium on "Recent Advances in Photonics", March 29, 2011, at Centre for Atomic and Molecular Physics, Manipal University, Manipal.
- Participated in the "Winter School on Polymers: Synthesis, Characterization and Applications", December 20-24, 2010, at Department of Materials Engineering, IISc, Bangalore.
- Attended the 10th International Conference on Fiber Optics and Photonics "PHOTONICS-2010", 11-15 December 2010, at IIT Guwahati, Guwahati, India.

MEMBERSHIP OF PROFESSIONAL BODIES

- **IEEE Photonics Society** and **Women in Engineering** Graduate Student free membership [2010-2011]

EXTRACURRICULAR ACTIVITIES

- All India Inter NIT Aquatics Women Championship prizes [2009-2013] and Special Prize for Swimming by St. Aloysius College, Mangalore [2007-08]
- All India Budokan Karate Federation Black belt [2007] and second prize in Asia World United Karate Organization Continental Open Karate Tournament, Visakhapatnam [2006]
- Served the Students' Council of St. Aloysius College, Mangalore as class representative [2007-2008] and volunteered for the National Level Science Fest 'Imprints 2007'
- Secured 'A' grade in National Cadet Corps Certificate C examination [2006] and volunteered in its various community development activities
- Received the Rashtrapati Puraskar (President Award) from The Bharat Scouts & Guides National Headquarters, New Delhi [2003]